



DEVELOPMENT OF A LOW-COST WEARABLE PREVENTION SYSTEM FOR MSDS
USING IMU SYSTEMS AND ELECTRICALLY CONDUCTIVE MATERIALS VIA ADDITIVE
MANUFACTURING



DEVELOPMENT OF A LOW-COST WEARABLE PREVENTION SYSTEM FOR MSDS USING IMU SYSTEMS AND ELECTRICALLY CONDUCTIVE MATERIALS VIA ADDITIVE MANUFACTURING

MEMORY

submitted for the Degree of Doctor of
Philosophy of the University of Navarra
by

Chuan Cao

under the supervision of
María Isabel Rodríguez and
Aitor Cazón Martín

Donostia-San Sebastián, May 2020



tecnun
Universidad
de Navarra

Pº Manuel Lardizabal, 13.

20018 Donostia-San Sebastián, Spain

Tel. 943 219 877

Fax 943 311 442

www.tecnun.es

Chuan Cao



tecnun
Universidad
de Navarra

VNIVERSITAS STVDIORVM
NAVARRENSIS VNIVERSITA
S STVDIORVM NAVARRENS

UNIVERSITY OF NAVARRA
SCHOOL OF ENGINEERING
DONOSTIA-SAN SEBASTIÁN



**DEVELOPMENT OF A LOW-COST
WEARABLE PREVENTION SYSTEM FOR
MSDS USING IMU SYSTEMS AND
ELECTRICALLY CONDUCTIVE MATERIALS
VIA ADDITIVE MANUFACTURING**

DISSERTATION

submitted for the Degree of Doctor of Philosophy
of the University of Navarra by

CHUAN CAO

under the supervision of

MARÍA ISABEL RODRÍGUEZ and

AITOR CAZÓN MARTÍN

Donostia-San Sebastián, May 2020

Acknowledgement

There is an ancient poem in China: "Hai nei cun zhi ji, tian ya ruo bi lin.", which means "A bosom friend afar brings distance near." During the three years of studying here, I have met many kind and lovely people and received countless help. Your meticulous care has made me feel like a hometown in this strange land, and also helped me to learn and experience a lot in this brand-new cultural environment. Here I want to express my gratitude with a little space.

First of all, I appreciate that the University of Navarra - Tecnun gave me this opportunity to do my PhD here in such a beautiful city. Thanks to all the people who work here, your hard work has made each of us extraordinary.

Secondly, I would like to thank my mentors, Aitor and Mabel. You are the most patient and selfless professors I have ever encountered. When I was in a low state and evaded reality, it was your effort, tolerance, and kindness that gave me enough courage to face the difficulties again. You have not only taught me the knowledge and way of thinking but also brought me the shining point of humanity. Thank you for everything you have done for me.

Also I would like to thank my colleagues: Sergio, Leire, Amaia, Mikel, Iñigo, Juan, and guys who have left school, Angél and Wilmer. You also gave me a lot of help and suggestions after work, I will not forget those happy hours with you. And people at Tecnun and Ceit:

Desmond, Izaro, Elena, and another Sergio, I am glad to meet you. In addition, Josecho's coffee is the best I have ever tasted, because it carries the memories of my talk with you during the coffee break here.

Far away in a foreign country, loneliness and incomprehension are the most unbearable burdens. Fortunately, there are several close friends here with me: Eric, Cristina, Zubi, Itu, Roby, and Juan. You have given me a taste of real western life, and I am also very happy to be able to show you the charm of Eastern culture through me.

Finally, I want to thank my parents: Guanghan and Zuomei. Thank you for giving me life. It is the love that across the time zone all last long. It makes me realize once again that even when the world's end is coming, when I turn back, I am extremely convinced that you are always there. I understand that these three years have made countless white hairs to your heads, and your cheeks are no longer rosy. Thank you for your silent effort, please let me use my remaining life to repay you well.

Chuan Cao

Table of contents

Acknowledgement	i
Table of contents	iii
List of figures	vii
List of tables.....	xiii
Abstract.....	xv
1 Introduction.....	1
1.1 Motivation.....	1
1.2 Main contributions of this thesis.....	3
1.3 Contents and structure of this thesis.....	4
2 State of the art	7
2.1 Introduction	7
2.2 Musculoskeletal disorders	7
2.2.1 Risk factors	7
2.2.2 Prevalence rate on body region.....	9
2.2.3 Assessment methods	15
2.2.4 Direct measurements for the human hand.....	24
2.3 Additive Manufacturing	29

2.3.1	Introduction.....	29
2.3.2	AM printing technologies	30
2.3.3	Functional materials for AM in wearables	35
2.4	Conclusions	39
3	Assessment of ergonomic methods	41
3.1	Introduction.....	41
3.2	Selection of the ergonomic methods.....	42
3.2.1	Assessment of Repetitive Tasks (ART).....	42
3.2.2	Rapid Upper Limb Assessment (RULA) and Rapid Entire Body Assessment (REBA).....	44
3.2.3	Biomechanical Assessment (BA).....	46
3.2.4	Optoelectronic Systems (OES)	47
3.2.5	Electro Goniometer (EG)	49
3.2.6	Accelerometry (ACC)	50
3.2.7	Inertial Measurement Unit (IMU)	52
3.3	Questionnaire: criteria.....	53
3.3.1	Before measuring.....	55
3.3.2	While measuring.....	56
3.3.3	After measuring	57
3.4	Expert interview	58
3.5	Results from experts	59
3.6	Conclusions	61
4	Developing finger motion capture device	63
4.1	Introduction.....	63
4.2	Hardware.....	64
4.2.1	Microcontroller	65
4.2.2	Inertial Measurement Unit.....	67
4.2.3	Multiplexer.....	69
4.2.4	SD module	69
4.3	Electrical connection layout.....	70
4.4	Assembling prototype.....	73
4.5	Software	73
4.5.1	System framework.....	73
4.5.2	Orientation format.....	74

4.5.3	Algorithm	80
4.6	Accuracy verification	86
4.7	Conclusions	89
5	Developing 3D printed conductive trace board	91
5.1	Introduction	91
5.2	Cross-contamination factors.....	93
5.3	Fabrication process.....	97
5.4	Design of experiments	99
5.4.1	Step 1. Maximum allowable resistance.....	99
5.4.2	Step 2. Conductive thermoplastic composites.....	101
5.4.3	Step 3. Printing settings: infill	101
5.4.4	Step 4. Printing settings: temperature, speed and layer height 102	
5.4.5	Step 5. Cross-sectional shape of conductive paths	103
5.5	Results of experiments	105
5.5.1	Determination of Maximum allowable resistance.....	105
5.5.2	Selection of conductive thermoplastic composites.....	105
5.5.3	Selection of internal infill pattern	106
5.5.4	Determination of temperature, speed and layer height.....	107
5.5.5	Selection of conductive paths cross-section.....	110
5.6	Prototype design	112
5.6.1	Pin connections	113
5.7	Prototype manufacturing	114
5.7.1	Relevant techniques and improvements	114
5.7.2	Manufacturing	121
5.8	Prototype testing	123
5.8.1	Working verification	123
5.8.2	Bending test	125
5.9	Conclusions	129
6	Developing wrist motion capture glove.....	131
6.1	Introduction	131
6.2	Selection of the textile	132
6.3	Glove design.....	134

6.4	Printing on textile	136
6.4.1	Preparation	136
6.4.2	Effects of bottom layers	137
6.5	Prototype printing and verification	140
6.6	Discussion.....	143
6.7	Conclusions	145
7	Conclusions and future research lines	147
7.1	Conclusions	147
7.2	Future work.....	150
Appendix A: Code library: Adafruit_BNO055.cpp.....		153
Appendix B: Code in Arduino IDE		173
Appendix C: Main Code in Matlab.....		179
Appendix D: Customized function code		
“DistalQuatMultiTransform()” in Matlab		187
Appendix E: Customized function code “VectorAngle()” in Matlab		189
Appendix F: Customized function code “cylinder2P()” in Matlab ..		191
Appendix G: RepRap G-Code Cheat Sheet (excerpted)		193
Appendix H: Starting Script in Simplify3D		195
Appendix I: Tool Change Script in Simplify3D		197
Appendix J: Ending Script in Simplify3D		199
Appendix K: Publications.....		201
List of nomenclature		205

List of figures

Figure 2-1 Unfavourable body postures in preliminary assembly work [17].	8
Figure 2-2 Neck and shoulder sections of the Nordic Musculoskeletal Questionnaire (NMQ) [38].	16
Figure 2-3 Worksheet of rapid upper limb assessment [40].	18
Figure 2-4 (a) Electromyography (EMG) sensors placed on the back; primary components of a desktop EMG system including (b) sensors and input module; and (c) main amplifier [48].	20
Figure 2-5 Industrial Lumbar Motion Monitor™ in real automotive workplace [49].	21
Figure 2-6 Anatomical drawings of the bones of the right hand (palmar view) [61].	24
Figure 2-7 The VICON™ motion capture set-up [64].	27
Figure 2-8 FK hand shape accuracy evaluation using different calibration methods. 4 commonly used hand poses are shown. The cross-coupled stretching effects (e.g. rIM ABD in “pointing” pose) are fixed by LMC-GPR and its SPGPs approximation [62].	27
Figure 2-9 The 3dID glove and the gateway [75].	28
Figure 2-10 Finger motion (Left: Actual, Right: Measured) [63].	29
Figure 2-11 Front view of the object in typical AM process. (Left: Virtual 3D model in software, Right: Actual printing result) ..	30

Figure 2-12 Schematic of an SLS printer [86].	31
Figure 2-13 Schematic of a Material Jetting printer [86].	32
Figure 2-14 Schematic of an SLA printer [86].	33
Figure 2-15 Schematic of a typical FDM printer [86].	34
Figure 2-16 Wearable soft electronics fabricated by hybrid 3D printing: a) image of textile-mounted printed strain sensor and microcontroller circuit. b,c) Images of real-time function of the wearable strain device (identified with arrows) at modest and maximum joint bending, respectively, along with the corresponding LED readout. d) Image of plantar sensor array. e) Illustration of sensor array readout in the absence of applied pressure and f) upon the application of pressure by a human foot [92].	36
Figure 2-17 The multilayer schematic of a 3D printed smart object which integrates advanced IC chips and other solid state components, as well as liquid-state circuit components and liquid metal interconnects [94].	37
Figure 3-1 The frequency/repetition stage of ART [104].	43
Figure 3-2 Worksheet of REBA [105].	45
Figure 3-3 A lifting posture entered in the 3D SSPP window	46
Figure 3-4 Real task, virtual task ergonomic evaluation and Motion Capture System laboratory workplace [111].	47
Figure 3-5 A ConvNet-based marker-less motion capture algorithm reconstructs joint angles of multiple people performing complex motions in outdoor settings, such as in this scene recorded with only three mobile phones: (left) 3D pose overlaid with one camera view, (right) 3D visualization of captured skeletons [102].	48
Figure 3-6 Description of root mean square distance (RMSD) values between angles calculated with the two techniques (marker-less (mkl) and marker-based (mb)); mean, standard deviation, minimum (Min) and maximum (Max) RMSD values are reported [115].	49
Figure 3-7 Placement of EG [119].	50
Figure 3-8 Experimental set-up using the isokinetic dynamometer and smartphone placed at the anterior medial surface of the tibia [121].	51

Figure 3-9 (a) Configuration of the IMU data glove showing individual IMU's.....	52
Figure 3-10 Sample of questionnaire (RULA/REBA) for evaluation.	54
Figure 3-11 Open question sheet.....	58
Figure 4-1 Human hand bones.....	64
Figure 4-2 Components of prototype.	65
Figure 4-3 Architecture of BNO055 [126].	68
Figure 4-4 Main dimensions of IMU (in inch) [127].	69
Figure 4-5 Circuit wiring for two IMUs.	70
Figure 4-6 A division of prototype's circuit wiring.....	71
Figure 4-7 Thumb & Index finger gesture capturing.	72
Figure 4-8 Data process in the system.....	74
Figure 4-9 Euler Angle Sequence z-y'-x".....	75
Figure 4-10 Quaternion for rotation.....	77
Figure 4-11 BNO055 chip remapping.	79
Figure 4-12 Orientation dot on BNO055.....	80
Figure 4-13 Flow chart of data process.	82
Figure 4-14 Remapping gesture: a) before applying the compensation angle, the virtual fingers are aiming to the magnetic north in the real world. b) after applying the compensation angle, the virtual fingers are aiming to the north of the virtual world. The orientation of the digital compass corresponds to the virtual world. Namely, the direction of the letter 'N' refers to the virtual north, and the physical index fingers are aiming to the west in reality.....	83
Figure 4-15 Example of data output on finger joint movements.....	86
Figure 4-16 Measuring gestures of each angle.	87
Figure 4-17 Thumb abduction angle measuring by goniometer (top) and computer (bottom).	87
Figure 5-1 the IMU sensor and Beetle microcontroller.	92
Figure 5-2 a) the Tumaker extruder head and b) disassembled extruder.	92
Figure 5-3 Partly overlapped traces due to the trace width is smaller than the extrusion width.....	93
Figure 5-4 Conductive material overflowed under an insufficient nozzle height.	94

Figure 5-5 Secondary melted materials are mixing together and causing cross-contamination.....	94
Figure 5-6 The extrusion accuracy is improved after configuring extrusion settings.....	95
Figure 5-7 Stringing effect when the nozzle moved to new position. A stringing ball is formed pointed by the left arrow when the stringing is broken.	96
Figure 5-8 a) Hot end changing temperature at the resting position; b) Filament clog in the left nozzle when the hot end suspending at the resting position.	98
Figure 5-9 a) Test for maximum external resistance on the VIN-GND lines b) Test for maximum external resistance on the SDA line c) Test for maximum external resistance on the SCL line.....	100
Figure 5-10 Printing simulation of three infill patterns on Simplify3D preview mode: longitudinal pattern, transversal pattern, alternating layer pattern from left to right.	102
Figure 5-11 Specimen dimensions (a), preview of the specimens in Simplify3D (b).	103
Figure 5-12 Cross-section pattern models: a) Rectangular pattern; b) Diamond pattern; c) Air gap pattern.	104
Figure 5-13 Full interaction plot from the ANOVA.	109
Figure 5-14 Specimens with different cross-section patterns: a) rectangular, b) diamond and c) air gap.	110
Figure 5-15 Microscope image of the 3D-printed sample featuring the air gap strategy.	111
Figure 5-16 Top view of prototype layout. All dimensions in mm. .	112
Figure 5-17 Pin connection: metal pin soldering with 3D printed hole.	113
Figure 5-18 Pin connection: male-female metal pin model.	114
Figure 5-19 Under-filled components. Arrows indicate the interspaces that may occur.....	115
Figure 5-20 Over-filled components. Arrows indicate the overflows that may occur.....	116
Figure 5-21 Prime pillar placed at east side.....	117
Figure 5-22 Prime pillar placed at southwest side.....	118
Figure 5-23 Conductive filament in the oven to remove moisture..	121

Figure 5-24 Assembly process: a specimen a) half printed; b) metal pin mounted; c) expanding the hole; d) soldering 3 mm tin into the hole.....	122
Figure 5-25 Prototype: dual printed conductive trace board.....	123
Figure 5-26 Data transmission through the prototype in real time.	124
Figure 5-27 Signals on the digital oscilloscope screen.....	124
Figure 5-28 Specification of bending test board. Left: board size. Right: trace size.	125
Figure 5-29 The specimen placed in flat with the metal actuator in the middle.	126
Figure 5-30 Measuring the instant resistance value in a bending test.	127
Figure 5-31 Samples after bending test with rebound deformation.	128
Figure 5-32 Resistivity changes at different deformation levels.	128
Figure 6-1 Sandwich structure of Neoprene.	133
Figure 6-2 Nitrile Examination Glove for drawing the fingerless glove shape on real hand.	134
Figure 6-3 Flat unfolded view of the glove.....	135
Figure 6-4 Fingerless glove without trace board.	135
Figure 6-5 Z-axis orientation of covers contacted with the textile. .	136
Figure 6-6 Z-axis orientation of trace board contacted with the textile.	136
Figure 6-7 Textile clung to the bed before printing the base. The printing area is calibrated to the outline of the base.....	137
Figure 6-8 Cross-section of red PLA printed on the white polyester woven [143].	138
Figure 6-9 Ground layer printed with concentric fill shape.	139
Figure 6-10 Ground layer printed with bevel mode.....	139
Figure 6-11 The stability changes under different ground layer thickness. From left to right, the thicker ground layer provides more stable contact interface.	140
Figure 6-12 Flat unfolded view of the glove with printed covers. ...	141
Figure 6-13 Complete glove with trace board prototype.....	142
Figure 6-14 Glove bending test with: a) Wrist in extension; b) Wrist in flexion.....	142

- Figure 6-15 Rebound resistance impact to the chip angle: a) trace board push the textile to generate folds; b) trace board pull the textile to generate gaps. Red line shows the inner layer of the textile..... 144

List of tables

Table 2-1: A comparison of MSDs prevalence studies. Data in %.	14
Table 2-2 Examples of observational methods adapted from [39].	19
Table 2-3 Examples of direct methods adapted from [39].	23
Table 2-4 Range of motion of finger flexion in deg adapted from [58].	26
Table 3-1 Definition of each Criteria: Before measuring.	55
Table 3-2 Definition of each Criteria: While measuring.	56
Table 3-3 Definition of each Criteria: After measuring.	57
Table 3-4 Scale results of main WMSDs assessment methods. Assessment of Repetitive Tasks (ART) Tools, Rapid Upper Limb Assessment / Rapid Entire Body Assessment (RULA/REBA), Biomechanical Assessment (BA), Optoelectronic Systems (OES), Electro Goniometer (EG), Accelerometry (ACC) and Inertial Measurement Units (IMU).	60
Table 4-1 Specification of Arduino UNO.	66
Table 4-2 Pin description of Arduino UNO.	67
Table 4-3 Data flow of one period.	81
Table 4-4 An example of output of calculated finger angles (in degree).	85
Table 4-5 Goniometry experiment results from three participants.	89
Table 5-1 Process variables and their levels for the ANOVA.	103
Table 5-2 Result of resistances for combined VIN and GND.	105

Table 5-3 Results from the comparison of commercially available materials.....	106
Table 5-4 Result of printing parameter test using Black Magic 3D.	107
Table 5-5 Resistance among traces as result of the cross-section pattern test.....	110
Table 5-6 Resistivity by cross-section area.....	111
Table 5-7 Summary of modified printing settings in Simplify3D... ..	120
Table 5-8 Resistivity and the p-value at different deformation levels.	127
Table 6-1 Maximum adhesion forces in N by type of fabric, layer height and printing material [7].	133
Table 6-2 Results of the Bending angles.	143

Abstract

Musculoskeletal disorders (MSDs) are chronic occupational injuries that are common in lean production due to excessive work or repetition. They are considered to be the main cause of disability and absenteeism, reduced production and increased costs. A large number of studies have shown that most of the discomforts are located in the upper body area, but few studies have focused on assessing the degree of exposure in the hand area.

The main objective of this thesis is to develop a low-cost wearable device in order to prevent and assess the potential exposure risks of MSDs in the hand. To that end, this thesis includes an evaluation of ergonomic assessment methods, a prototype development of a low-cost wearable, and experimental research in order to implement functional additive manufactured materials to that prototype.

In the evaluation study, seven ergonomic assessing measurements were selected for comparison and analysis through an optimised questionnaire and expert interview. It has been concluded that the Inertial Measurement Units (IMU) method is currently the most suitable measurement technology for hand MSDs risk assessment.

For the prototype development, Arduino-based hardware modules were selected, and a functional prototype for tracking index finger and thumb movements in real-time is built with the quaternion-based core algorithm.

Finally, a prototype of the wearable is developed using electrically conductive materials deposited via Additive manufacturing. Several

conductive filaments are tested, and an optimised method is employed to avoid cross-contamination effects.

摘要

肌肉骨骼类疾病（MSDs）是在精益生产工作中常见的由过度工作或重复性工作引起的慢性职业病。这些问题被认为是造成残疾和旷工，生产减少和成本增加的主要因素。大量研究表明，多数不适位于上身区域，但是很少有研究专注于评估手部区域的暴露程度。

本文的主要目的是开发一种低成本的可穿戴设备，以预防和评估手部 MSDs 的潜在暴露风险。为此，本文包括对人体工程学评估方法的评估，低成本可穿戴设备的原型开发以及为了将功能性添加剂制造材料应用于该原型而进行的实验研究。

在评估研究中，通过优化的问卷调查与专家面谈，选择了 7 种常用的人机工程评估测量方法进行比较分析，并总结得出惯性测量单位（IMU）是目前最适合作为手部 MSDs 风险评估的测量技术。

在原型开发方面，选择了基于 Arduino 的硬件模块，搭建了以四元数旋转为核心算法的能够实时追踪食指和拇指动作的功能原型。

最后，通过增材制造技术使用石墨烯导电材料实现可穿戴设备的原型。其中对几类线材进行了研究和测试，以及总结了一种合适的避免交叉污染效应的方法。

Resumen

Los trastornos musculo esqueléticos son lesiones crónicas comunes en las líneas de producción debido a movimientos repetitivos. Se consideran como la principal causa de absentismo por bajas, reducción de la producción y aumento de costes. Un gran número de estudios ha mostrado que la mayor parte de las molestias están localizadas en las extremidades superiores, pero pocos estudios se han centrado en la evaluación del grado de exposición de la mano a estas lesiones.

El principal objetivo de esta tesis es desarrollar un wearable de bajo-coste para prevenir y evaluar los riesgos de exposición potenciales a estas lesiones musculoesqueléticas en la mano. A tal fin, esta tesis incluye una evaluación de los métodos de valoración ergonómica, el desarrollo de un prototipo de wearable de bajo-coste y una investigación experimental para implementar materiales funcionales en el prototipo mediante Fabricación Aditiva.

En la parte de evaluación, se seleccionaron siete metodologías ergonómicas para compararlas mediante un cuestionario y entrevistas con expertos. Se concluyó que los sistemas inerciales (IMU) son la tecnología más adecuada para evaluar las lesiones musculo esqueléticas en la mano.

Para el desarrollo, se seleccionaron elementos de hardware basados en Arduino para desarrollar un prototipo que capturaba el movimiento de los dedos índice y pulgar usando el sistema de cuaterniones.

Finalmente, se fabricó un prototipo que incorporaba un material conductor eléctrico depositado mediante Fabricación Aditiva para conectar el hardware. Varios filamentos conductores fueron probados previamente, y se desarrolló una metodología optimizada para evitar los efectos de la contaminación cruzada.

Chapter 1:

Introduction

1.1 Motivation

According to the United States (US) Bureau of Labor Statistics (BLS) definition for 2018 and prior years, Musculoskeletal Disorders (MSDs) “include cases where the nature of the injury or illness is sprains, strains, tears; back pain, hurt back; soreness, pain, hurt, except the back; carpal tunnel syndrome (CTS); hernia; or musculoskeletal system and connective tissue diseases and disorders, when the event or exposure leading to the injury or illness is bodily reaction/bending, climbing, crawling, reaching, twisting, overexertion, or repetition” [1]. They can lead to peripheral nerve entrapments (e.g. ulnar tunnel syndrome, carpal tunnel syndrome), peripheral enthesopathies (e.g. shoulder tendinitis, hand-wrist tendinitis, lateral epicondylitis) and many other non-specific musculoskeletal pain disorders. MSDs are relatively diverse disorders that may affect different structures: tendons, muscles, joints, nerves, and the vascular system. All the different generic names, such as Repetitive Strain Injury (RSI), Cumulative Trauma Disorder (CTD), Upper Limb Syndrome,

Cervicobrachial Disorder, are used to describe nearly the same problem [2]. Those symptoms are the most common injuries in the manufacturing sector that generate pain for chronic suffering but workers are not aware of the fatigue of key body parts until discomfort or pain appears.

Under the development of global economic industry chains, modern lean manufacturing strategies have become a prevailing way of industrial production. When job demands overwhelm an employee's mental and/or physical capacity and lead to MSDs, employee health, comfort, and productivity can be adversely affected [3]. Some studies revealed that increased musculoskeletal risk symptoms were related to increases of work pace and lack of recovery time due to Just-In-Time production, especially in the automotive industry [4].

With respect to the social consequences, main large production economies are facing problems of chronic musculoskeletal illness, which lead to a loss in productivity, increasing costs and worker dissatisfaction. In fact, MSDs are considered as a main factor in disabilities and absenteeism, reduced production and increased costs [5]. With regards to economic cost, MSDs led to 3,138,000 lost workdays in the United Kingdom in the period 2015-2016 [6] and a total cost of lost productivity of € 240 billion, or up to 2% of gross domestic product (GDP) in 2015 in the European Union [7]. Such chronic diseases with low mortality, but high morbidity, impact on the individuals' ability to participate in the labour market [7]. For example, 100 million European citizens suffer from chronic musculoskeletal pain and MSDs [8], including 40 million workers who attribute their MSDs directly to their work [9]. Therefore, it is widely recognised that work can lead and contribute to MSDs. Solving such health problems has always been a topic of great concern to scholars and employers. Nowadays, numerous approaches which meet a variety of situations and apply to different techniques have been developed to prevent and diagnose MSDs.

In order to reduce MSDs risks in the workplace, more proactive strategies can be adopted, which are roughly divided into three levels [10]:

- Primary prevention includes risk assessment processes, technical / ergonomics, organisational and person-oriented interventions.
- Secondary prevention includes the identification and health monitoring of workers in hazardous work environments.
- Tertiary prevention comprises return-to-work measures.

Risk assessment of MSDs is mainly used as a primary or secondary preventive measure. Among them, ergonomic risk assessment is the main intervention and prevention method. However, mainstream ergonomic risk assessment methods still rely on self-reporting and expert observations to come to assessment conclusions, which cannot objectively and effectively identify the true working physical factors. In recent years, many ergonomic experts have tried to introduce various measurement techniques to improve the evaluation results and enable various physical indicators to be accurately quantified. Most of the measurement technologies come from other fields and they have shortcomings such as being oversized, too time-consuming, too limited in measuring objects, or high learning costs. Moreover, the laboratory measuring equipment also interfere with the working state and psychological response of the workers, which cannot accurately reflect the incorrect body posture in the actual work. Therefore, measurement equipment specifically adapted to the actual production environment is a practical requirement for many ergonomic risk assessments.

1.2 Main contributions of this thesis

The main objective of this thesis is to develop a low-cost wearable device that analyses musculoskeletal disorders in the hand. This research project has made the following contributions:

- Identify the body parts with high MSDs exposure risks which have not been catalogued by previous studies.
- Develop a new set of measurement assessment tools to evaluate the ergonomic methods with questionnaire surveys and expert interviews, from which the appropriate technology is selected.

- Develop a cross-platform algorithm for sending and receiving data packets and processing quaternion rotation. Based on this algorithm, a real-time, low-cost and high-precision prototype capable of tracking two fingers is developed.
- Explore the electrical characteristics of different brands of conductive filaments to screen for a filament that is suitable for use as circuit traces, and establish the relationship between key printing parameters and the material's resistivity.
- Experimentally verify the feasibility of the dual-material printed circuit. A set of experiences and innovative methods of dual-material printing focusing on conductive materials are concluded, and the cross-contamination problem is largely resolved.
- In the end, a functional prototype that implements massive signal transmission of Microelectromechanical Systems (MEMS)-type active sensors has been successfully made using the dual-print methodology.

1.3 Contents and structure of this thesis

The thesis is divided into seven chapters including the present chapter where the motivation of the project is presented. A brief description of the remaining chapters is given in the following bullet points:

- Chapter 2 establishes the context of this thesis by summarising the major relevant studies. The basic concept of musculoskeletal disorders is described and the ergonomic assessment methods are introduced. Then the investigation of additive manufacturing techniques and its related functional materials is presented.
- Chapter 3 introduces seven popular ergonomic methods. Each method is evaluated with a questionnaire that takes multiple factors into account for a quantitative assessment. Combining the analysis results of the questionnaire with the experts' points of view, it is possible to select the most suitable measurement technology for the functional implementation of this study.

-
- Using the previously selected technology, Chapter 4 illustrates the process for developing the prototype. The components are selected and the circuit structures are established for the hardware, while for the software the data format and the algorithm principle are introduced. The feasibility verification is carried out.
 - Chapter 5 focuses on how to use dual-printing technology to further develop the previous results into a second-generation prototype that can meet the needs of wearable devices. Firstly, suitable 3D printing conductive materials were screened out and their conductivity was studied. Secondly, a set of methodologies to reduce cross-contamination were given and the printing experiments were carried out. The prototypes were designed and successfully manufactured. Finally, the functional verification was performed.
 - Chapter 6 describes an experimental methodology for dual-printing the previous prototype onto a textile. A glove-like prototype has been fabricated and verified.
 - Finally, Chapter 7 summarises the main results and contributions achieved in the project, and suggestions for future work are proposed.

Chapter 2:

State of the art

2.1 Introduction

In this chapter, the relevant background studies related to each section of this thesis project are collected. The state of the art is distributed into two parts. In the first part, the knowledge of risk factors, prevalence rate on body region about musculoskeletal disorders (MSDs) and three main classes of ergonomic assessment methods are presented. In the second part, the family of Additive Manufacturing techniques, functional materials, and several smart wearable applications are introduced.

2.2 Musculoskeletal disorders

2.2.1 Risk factors

Previous studies indicate that ergonomic (physical, psychosocial and organizational) of the workplace may be associated with the occurrence of MSDs [10]:

- Physical risk factors, including excessive repetitive movements, awkward postures, mechanical over load, manual material handling, exposure time and vibration can increase the risk of MSDs [10][12][13].
- Organizational risk factors such as time constraints, work rate and workload also affect to the prevalence of MSDs [14].
- Psychosocial risk factors, such as low decision latitude (the lack of authority to make important decisions in a company or institute), high psychological demands, job dissatisfaction, effort-reward imbalance, high work stress and low social support may also influence these disorders [13] [14].



Figure 2-1 Unfavourable body postures in preliminary assembly work [17].

It is difficult to individually attribute the cause and effect of MSDs on specific work activities or particular body region. MSDs present serious ergonomic problems, particularly in the automotive industry due to the wide variety of ergonomic high risk tasks including tightening, picking up, lifting, material handling, as well as the characteristics of assembly line work [15]. Figure 2-1 shows a common example of awkward body postures while doing assembly work. Moreover, a higher prevalence of MSDs among females may be related to the situation that they are still mainly in charge of housework [16]. Such non-occupational MSDs may be aggravated even the work is not

the cause. Studies also showed that work aging, smoking, care of responsibilities are some of the key facts that lead to a high prevalence of MSDs [5][13][10]. Additionally, some intrinsic risk factors, which also have a part to play in the onset and deterioration of MSDs, can be altered while other risk factors cannot, such as genetic predisposition [7].

2.2.2 Prevalence rate on body region

MSDs prevalence in epidemiology is understood as a proportion of the patient diagnosed to have musculoskeletal symptoms with the total number of the population studied, which is commonly used for chronic disease with a long course [18]. Depending on the occupation, the workload of each body region is different. Table 2-1 shows eight epidemiologic studies, which focus on automotive assembly sections, where the MSDs prevalence of twelve defined body regions is compared.

Fredriksson et al [12] investigated the influence of a reorganization of work from lineout to line production in physical and psychosocial conditions on MSDs in a car-body-sealing department at an automobile assembly plant in Sweden. Whereas the physical workload was assessed by questionnaires, direct measurements (The type of ergonomic assessments are introduced in the next section) (Physiometer, Aaras and Stranden, 1988) and computer-based observation registration (PEOFlex, SE Staphorst, Holland), and the psychosocial conditions by questionnaires and group discussions. The study group was established with 33 women (mean age of 39.1) and 24 men (mean age in 32.5 years). Among 90% of the women and two thirds of men have been gainfully employed for more than 10 years. More than half of the women and a quarter of the men have worked at the sealing department for more than 10 years. In relation to prevalence, Frederickson discovered that most of the discomforts are located in the upper body regions, including shoulder (37%), wrist (23%), upper back (19).

Hussain et al [19] investigated the prevalence of musculoskeletal symptoms in a group of truck assembly workers in United Kingdom. This cross-sectional study was carried out using a modified version of

the Nordic questionnaire and the General Health Questionnaire (GHQ12). The respondents for the study are 323 truck assembly workers, where the mean age is 36.5 years and the mean period of employment is 13.9 years, and a total of 79% (n = 255) of respondents reported MSDs in one or more of the defined body regions during the previous 12 months before the study is carried out. They pointed out that there is a high prevalence of musculoskeletal symptoms in this group of truck assembly workers, mainly affecting on low back, shoulders, neck and wrist/hand areas.

Landau et al [17] reported a case study at 256 work stations on an assembly line for middle class cars manufactured by a globally active corporation. They wanted to focus on the interaction between age of the assembly workers and the choice of workplace. They utilised Workload Screening Procedure (WSP) to classify work demands, OWAS (OVAKO Working Posture Analysing System) to assess; lifting and carrying activities, the BkA Method to evaluate unfavorable body postures and lifting of loads, EN 614-1-European standard to evaluate ergonomic design of workplaces, National Institute of Occupational Safety and Health (NIOSH) to obtain recommended of weight limits (RWL) in jobs, and finally REFA to evaluate load handing. The respondents for the study were 256 truck assembly workers, where most (57%) of the workers in the sample had been working for between 2 and 4 years, 31 % of the workers had been working there for 4 years or more and 9% for more than 10 years. Finally, Landau reports that age and job strain are not independent variables in their case. Older workers still complain of lumbar spine symptoms although low demands job are assigned. This may due to the long-term cumulative effects and the induced non-occupational multifactorial spine symptoms. Where low back (39%) is the first, and neck (18%) comes with the second-high prevalence in the study.

Anita et al [20] conduct another study to determine the prevalence of musculoskeletal symptoms and the association with awkward posture among automotive assembly line workers in Malaysia. They use Standardized Nordic Questionnaire (SNQ) and Rapid Upper Limb Assessment (RULA) to obtain and estimate the results. The respondents for the study were 232 assembly workers, where the

median age was 24 years (from 20 to 52), and half of the respondents were at their early working career stage (less than 3 years). A total prevalence of musculoskeletal symptoms among all body regions was 78.4%. They concluded that the highest percentage of complaints followed by low back, shoulder, wrist/hand, neck. The prevalence of MSDs increases as the RULA action level and job rotation increases.

Nur et al [21] also investigated the prevalence of MSDs among assembly workers in several automotive manufacturing companies in Malaysia. Similarly, they used Standardized Nordic Musculoskeletal Questionnaires (NMQ) to collect data. The respondents for the study were 152 assembly workers with the age between 25 -44 years old (92.1%), where 39.5% of the respondents has working experiences between 6 -10 years, 25.7% of the respondents with experiences more than 10 years, and 24.3% of the respondents has working experiences between 3 -5 years. A total of 76.97% among respondents reported MSDs in any defined body regions during the last 12 months. Nur reported the workers in the automotive manufacturing companies are exposed to the risk of MSDs especially on the upper limb region, where repetitive task is associated with the prevalence of MSDs pain and discomfort.

Zare et al [14] assessed the ergonomic physical exposure, organizational and psychosocial factors in a truck assembly plant for two different cycle times A (11 min) and B (8 min). The musculoskeletal symptoms were evaluated by a modified version of the Nordic Musculoskeletal Questionnaire. Due to the cycle time A was performed in advance and the cycle time B was carried out after the new workstations and organization were established seven months later. Additional workers were employed for the B cycle by the operators and tested together with the same respondents. Therefore, the respondents were divided into two groups to have four group of results from a to d in Table 2-1. All the subjects in this study were men, with a mean age of 42.0 years for cycle time A and 38.1 years for cycle time B. The mean length of work experience in the current job was 16.0 years for cycle time A and 13.0 years for B. Zare demonstrated that the physical risk factors mainly involving the upper limbs were significant among truck assembly workers (67%, 35%, 55%, 36% on

shoulder region for each groups of cycle time and respondents, and 53%, 40%, 45%, 36% on upper arm region for each groups of cycle time and respondents in Table 2-1). Additionally, they discovered that low degree of decision freedom (also called decision latitude) and high psychological demands were common psychosocial risk factors among subjects, good quality social support reduced the strain. Effective interventions are not only engineering solutions but also organizational and administrative adaptations.

Lee et al [18] investigated the prevalence of MSDs among Korean auto workers in a mission assembly plant (a line which carries heavy metal part). The research was conducted by focus group interview, self-administered questionnaire and survey on musculoskeletal symptoms. There were 137 male respondents (average age was 34.1 years) participated in the survey. This study shows that MSDs symptoms and serious pain were reported in neck, shoulder, back and fingers, which were statistically related to various demographic factors, such as age, stature, stretching, and work satisfaction.

Fazilah et al [22] investigated the prevalence of MSDs and ergonomic risk factors among the production workers at a selected automotive component manufacturer in Malaysia. Data were collected by conducting structure interviews using Cornell Musculoskeletal Discomforts Questionnaire (CMDQ). Respondents were 40% from the total number of production assembly team members, who worked in a different shift, including normal shift (13%), day shift (41%) and night shift (46%), while the exact number of sample size and respondent age are not mentioned in this study. They reported that a higher risk of MSDs was found followed by low back, upper back, right shoulder and right wrist. It is also suggested that special attention should be paid to not only on physical aspect, but also on psychosocial aspect in production team members because the exposure level is high for vibrations, work pace and stress in most of the workstations.

Table 2-1 shows MSDs prevalence on body regions based on the above mentioned eight studies. The body regions are generally distributed in neck, shoulders, upper arm, upper back, lower back,

elbow, forearm, wrist, hand/palm, finger, upper back, low back, hips, knees, ankles/feet.

Summing up, numerous studies have demonstrated the exposure-response relationships between risk factors and major body regions. The comparison reveals that low-back region is in the highest rate among half of the eight studies. Next comes to neck region, then shoulder/upper limb and the hand/wrist region is on the fourth position. Differences among studies can be explained by the type of country, type of the job, ages, assessment methods, period of employment or work cycle time.

However, there is a serious lack of quantitative data regarding epidemiology studies of MSDs on elbow and hand regions [23]. It has been discovered that repetitive tasks, with short work cycles involving quick arm and hand movements, as well as force-demanding tasks are high related to risk factors [24][25], where awkward wrist postures is considered a risk factor lead to carpal tunnel syndrome [26][25]. Due to the overlaying effect of work properties and environments, several risk factors often occur concurrently, and synergistic effects have been proofed [27].

Table 2-1: A comparison of MSDs prevalence studies. Data in %.

Prevalence	Fredriksson [12] *	Hussain [19]	Landau [17] *	Anita [20]	Nur [21]	Zare [14]				Lee [18]	Fazilah [22]
						T1**	T2**	T3**	T4**		
Neck	38	60	18	32.2	49.3	33	10	27	9	72.5	—
Shoulder	37	57	—	37.9	46.7	67	35	55	36	51.7	61.4
Upper arm	—	—	—	—	—	53	40	45	36	25.4	—
Elbow	—	20	12	9.1	6.6	—	—	—	—	15.3	—
Forearm	—	—	—	—	—	47	40	36	27	15.2 ***	—
Wrist	23	46	10	34.1	48	—	—	—	—	35 ***	60
Hand / palm	—	—	—	—	—	33	20	18	18	18.9 ***	—
Finger	—	—	—	—	—	—	—	—	—	64.4 ***	—
Upper back	19	17	6	31	33.6	33	25	45	18	65.1	63.2
Low back	40	65	39	50.9	21.7	47	35	45	27	—	75.4
Hips	8	8	3	16.4	14.5	27	10	27	9	8	—
Knees	15	39	16	25.4	15.8	20	30	27	27	47.4	—
Ankles/feet	18	13	—	24.1	1.3	27	20	27	18	42.3	—

* The data was visually inspected from the figure in the references.

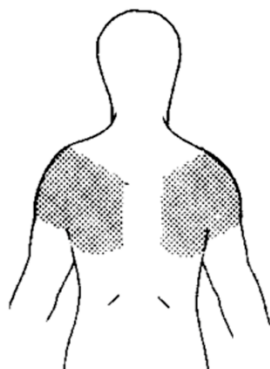
** T1: All respondents on cycle time A; T2: All respondents on cycle time B; T3: Same respondents on cycle time A; T4: Same respondents on cycle time B.

*** This study divided body regions into several unique parts different from other studies.

2.2.3 Assessment methods

On the purpose of evaluating potential MSDs exposures to risk factors, ergonomic specialists use one or multiple ergonomic assessment methods in physical, psychophysical, physiological, and biomechanical demands. The measurement techniques can be identified and categorized under the three main groups that have conventionally been used among earlier studies [28][29]: self-reports, observational methods, and direct measurements.

Self-reports: The experience of ergonomic assessment is originated from this group of method. Self-reports, including rating scales, questionnaire, checklists or interviews, are commonly used for simple and quick evaluations which do not require a high accurate result. In self-report, workers may be asked to estimate the prevalence of postures, the frequency of movements and the presence of levels of force or other physical agents [30]. Figure 2-2 shows a typical self-report questionnaire, named Nordic Musculoskeletal Questionnaire. However, they are not always reliable and could lead to biased interpretation [31][32]. For example, those workers who are suffering from severe low back or neck pain, have a higher probability to report longer durations or frequencies of physical load in comparison with those workers from the same occupational groups who are pain free [33][34]. Although this type of methods is doubtful for quantification of the absolute level of exposure [35], the target group at comparatively higher risk can be identified for more detailed analysis using other types of methods [36]. Their levels of reliability and validity are reportedly too low for use as the basis for ergonomics intervention [37].



SHOULDER

How to answer the questionnaire: By shoulder trouble is meant ache, pain or discomfort in the shaded area. Please concentrate on this area, ignoring any trouble you may have in adjacent parts of the body. There is a separate questionnaire for neck trouble.

Please answer by putting a cross in the appropriate box — one cross for each question. You may be in doubt as to how to answer, but please do your best anyway.

9. Have you **ever** had shoulder trouble (ache, pain or discomfort)?

1 No 2 Yes

If you answered **No** to Question 9, do not answer the questions 10—17.

10. Have you **ever** hurt your shoulder in an **accident**?

1 No 2 Yes, my right shoulder
3 Yes, my left shoulder
4 Yes, both shoulders

11. Have you **ever** had to **change jobs or duties** because of shoulder trouble?

1 No 2 Yes

12. Have you had shoulder trouble during the **last 12 months**?

1 No 2 Yes, in my right shoulder
3 Yes, in my left shoulder
4 Yes, in both shoulders

If you answered **No** to Question 12, do not answer the questions 13—17.

13. What is the **total** length of time that you have had shoulder trouble during the **last 12 months**?

1 1—7 days
2 8—30 days
3 More than 30 days, but not every day
4 Every day

14. Has shoulder trouble caused you to **reduce** your activity during the **last 12 months**?

a. Work activity (at home or away from home)?

1 No 2 Yes

b. Leisure activity?

1 No 2 Yes

15. What is the **total** length of time that shoulder trouble has **prevented** you from doing your normal work (at home or away from home) during the **last 12 months**?

1 0 days
2 1—7 days
3 8—30 days
4 More than 30 days

16. Have you **been seen** by a doctor, physio-therapist, chiropractor or other such person because of shoulder trouble during the **last 12 months**?

1 No 2 Yes

17. Have you had shoulder trouble at any time during the **last 7 days**?

1 No 2 Yes, in my right shoulder
3 Yes, in my left shoulder
4 Yes, in both shoulders

Figure 2-2 Neck and shoulder sections of the Nordic Musculoskeletal Questionnaire (NMQ) [38].

- **Observational methods:** This type of methods is carried out with the help of field observation or video recording. Field observation may be done either by expert checklists or by more detailed recording of work components and actions observed by the researcher [30]. Some field observational techniques allow only postural assessments of various body segments, while the majority provide the assessment of several critical physical exposure factors, such as posture, load/force, movement frequency, duration, recovery, vibration, etc. [39]. Field observations are practical and able to be performed with low-cost equipment, but still cannot avoid subjective bias in terms of intra- and inter-observer variability when choosing among different categories of exposure. They are better to assess static (posture held) or repetitive (simple pattern) jobs [28]. For prescribing acceptable exposures limits for respondents or determining a priority order for intervention across a range of tasks, these methods output overall exposure factor indices or scores. In which epidemiological data upon which these scoring systems are based is limited particularly with respect to how different factors should be weighted [39]. Figure 2-3 shows an example of simple observational assessment, widely known as RULA.

On the other hand, video records provide reproducible evaluations and complete details for highly dynamic movements at a time, due to the reusable video memory or by dedicated computer software. More precise dimensions, such as velocities, rotation angles, movement distance and accelerations are captured and analysed in real time or post-processing for a set of tasks. However, video-based observational techniques require substantial cost and expertise for effective operation. These methods may be time consuming and also have problems such as camera blind area, or limited perspective, which may increase the data error. Basically this type of techniques are more suitable for use in recording and analysing simulated tasks, rather than for conducting practical assessments in the workplace [39]. Table 2-2 introduced a brief comparison of most common observational methods.

Morgan Maxwell
Chartered Ergonomists

RULA Employee Assessment Worksheet

McLennany, L. & Corlett, E.N. (1993) RULA: a survey method for the investigation of work-related upper limb disorders. Applied Ergonomics, 24, 91-99.

© 2012 Morgan Maxwell
All Rights Reserved

TABLE A - Arm & Wrist Analysis

Step 1: Locate Upper Arm Position

Step 1a: Adjust...

- If shoulder is raised; +1
- If upper arm is abducted; +1
- If arm is supported or person is leaning; -1

Step 2: Locate Lower Arm Position

Step 2a: Adjust...

- If arm is working across midline of the body; +1
- If arm out to side of body; +1

Step 3: Locate Wrist Position

Step 3a: Adjust...

- If wrist is bent from the midline; -1

Step 4: Wrist Twist

- If wrist is twisted in mid-range =1
- If twist at or near end of range = 2

Step 5: Look-up Posture Score in TABLE A

- Use values from steps 1,2,3 & 4 to locate Posture Score in table A

Step 6: Add Muscle Use Score

- If posture mainly static (i.e. held for longer than 1 minute) or
- If action repeatedly occurs 4 times per minute or more; +1

Step 7: Add Force/load Score

- If load less than 2 kg (intermittent); -0
- If 2 kg to 10 kg (static or repeated); -2
- If more than 10 kg load or repeated or shocks; +3

TABLE C - Step 8: Find Row in Table C

- The completed score from the Arm/wrist analysis is used to find the row on Table C

TABLE B - Neck, Trunk & Leg Analysis

Step 9: Locate Neck Position

Step 9a: Adjust...

- If neck is twisted; +1
- If neck is side-bending; +1

Step 10: Locate Trunk Position

Step 10a: Adjust...

- If trunk is twisted; +1
- If trunk is side-bending; +1

Step 11: Legs

- If legs & feet supported and balanced; +1
- If not; -2

Step 12: Look-up Posture Score in TABLE B

- Use values from steps 9, 10 & 11 to locate Posture Score in Table B

Step 13: Add Muscle Use Score

- If posture mainly static or
- If action 4 minutes or more; +1

Step 14: Add Force/load Score

- If load less than 2 kg (intermittent); +0
- If 2 kg to 10 kg (static or repeated); -2
- If more than 10 kg load or repeated or shocks; +3

Step 15: Find Column in TABLE C

- If load less than 2 kg (intermittent); -0
- If 2 kg to 10 kg (intermittent); +1
- If 2 kg to 10 kg (static or repeated); -2
- If more than 10 kg load or repeated or shocks; +3

	UPPER ARM				LOWER ARM				WRIST				Final Posture Score	
	1	2	3	4	1	2	3	4	1	2	3	4		
1	1	2	1	2	1	2	1	2	1	2	1	2	1	2
2	1	2	2	3	2	3	2	3	2	3	2	3	3	3
3	2	3	2	3	3	3	3	3	3	3	3	3	4	4
4	2	3	3	4	3	4	3	4	3	4	3	4	4	4
5	2	3	3	4	4	4	4	4	4	4	4	4	5	5
6	2	3	3	4	4	4	4	4	4	4	4	4	5	5
7	3	4	3	4	4	4	4	4	4	4	4	4	5	5
8	3	4	4	5	4	4	4	4	4	4	4	4	5	5
9	3	4	4	5	4	4	4	4	4	4	4	4	5	5
10	3	4	4	5	4	4	4	4	4	4	4	4	5	5
11	3	4	4	5	4	4	4	4	4	4	4	4	5	5
12	3	4	4	5	4	4	4	4	4	4	4	4	5	5
13	3	4	4	5	4	4	4	4	4	4	4	4	5	5
14	3	4	4	5	4	4	4	4	4	4	4	4	5	5
15	3	4	4	5	4	4	4	4	4	4	4	4	5	5
16	3	4	4	5	4	4	4	4	4	4	4	4	5	5
17	3	4	4	5	4	4	4	4	4	4	4	4	5	5
18	3	4	4	5	4	4	4	4	4	4	4	4	5	5
19	3	4	4	5	4	4	4	4	4	4	4	4	5	5
20	3	4	4	5	4	4	4	4	4	4	4	4	5	5
21	3	4	4	5	4	4	4	4	4	4	4	4	5	5
22	3	4	4	5	4	4	4	4	4	4	4	4	5	5
23	3	4	4	5	4	4	4	4	4	4	4	4	5	5
24	3	4	4	5	4	4	4	4	4	4	4	4	5	5
25	3	4	4	5	4	4	4	4	4	4	4	4	5	5
26	3	4	4	5	4	4	4	4	4	4	4	4	5	5
27	3	4	4	5	4	4	4	4	4	4	4	4	5	5
28	3	4	4	5	4	4	4	4	4	4	4	4	5	5
29	3	4	4	5	4	4	4	4	4	4	4	4	5	5
30	3	4	4	5	4	4	4	4	4	4	4	4	5	5
31	3	4	4	5	4	4	4	4	4	4	4	4	5	5
32	3	4	4	5	4	4	4	4	4	4	4	4	5	5
33	3	4	4	5	4	4	4	4	4	4	4	4	5	5
34	3	4	4	5	4	4	4	4	4	4	4	4	5	5
35	3	4	4	5	4	4	4	4	4	4	4	4	5	5
36	3	4	4	5	4	4	4	4	4	4	4	4	5	5
37	3	4	4	5	4	4	4	4	4	4	4	4	5	5
38	3	4	4	5	4	4	4	4	4	4	4	4	5	5
39	3	4	4	5	4	4	4	4	4	4	4	4	5	5
40	3	4	4	5	4	4	4	4	4	4	4	4	5	5
41	3	4	4	5	4	4	4	4	4	4	4	4	5	5
42	3	4	4	5	4	4	4	4	4	4	4	4	5	5
43	3	4	4	5	4	4	4	4	4	4	4	4	5	5
44	3	4	4	5	4	4	4	4	4	4	4	4	5	5
45	3	4	4	5	4	4	4	4	4	4	4	4	5	5
46	3	4	4	5	4	4	4	4	4	4	4	4	5	5
47	3	4	4	5	4	4	4	4	4	4	4	4	5	5
48	3	4	4	5	4	4	4	4	4	4	4	4	5	5
49	3	4	4	5	4	4	4	4	4	4	4	4	5	5
50	3	4	4	5	4	4	4	4	4	4	4	4	5	5
51	3	4	4	5	4	4	4	4	4	4	4	4	5	5
52	3	4	4	5	4	4	4	4	4	4	4	4	5	5
53	3	4	4	5	4	4	4	4	4	4	4	4	5	5
54	3	4	4	5	4	4	4	4	4	4	4	4	5	5
55	3	4	4	5	4	4	4	4	4	4	4	4	5	5
56	3	4	4	5	4	4	4	4	4	4	4	4	5	5
57	3	4	4	5	4	4	4	4	4	4	4	4	5	5
58	3	4	4	5	4	4	4	4	4	4	4	4	5	5
59	3	4	4	5	4	4	4	4	4	4	4	4	5	5
60	3	4	4	5	4	4	4	4	4	4	4	4	5	5
61	3	4	4	5	4	4	4	4	4	4	4	4	5	5
62	3	4	4	5	4	4	4	4	4	4	4	4	5	5
63	3	4	4	5	4	4	4	4	4	4	4	4	5	5
64	3	4	4	5	4	4	4	4	4	4	4	4	5	5
65	3	4	4	5	4	4	4	4	4	4	4	4	5	5
66	3	4	4	5	4	4	4	4	4	4	4	4	5	5
67	3	4	4	5	4	4	4	4	4	4	4	4	5	5
68	3	4	4	5	4	4	4	4	4	4	4	4	5	5
69	3	4	4	5	4	4	4	4	4	4	4	4	5	5
70	3	4	4	5	4	4	4	4	4	4	4	4	5	5
71	3	4	4	5	4	4	4	4	4	4	4	4	5	5
72	3	4	4	5	4	4	4	4	4	4	4	4	5	5
73	3	4	4	5	4	4	4	4	4	4	4	4	5	5
74	3	4	4	5	4	4	4	4	4	4	4	4	5	5
75	3	4	4	5	4	4	4	4	4	4	4	4	5	5
76	3	4	4	5	4	4	4	4	4	4	4	4	5	5
77	3	4	4	5	4	4	4	4	4	4	4	4	5	5
78	3	4	4	5	4	4	4	4	4	4	4	4	5	5
79	3	4	4	5	4	4	4	4	4	4	4	4	5	5
80	3	4	4	5	4	4	4	4	4	4	4	4	5	5

FINAL SCORE: 1 or 2 = Acceptable; 3 or 4 investigate further; 5 or 6 investigate further and change soon; 7 investigate and change immediately

SUBJECT:

COMPANY:

DEPARTMENT:

SCORER:

DATE:

Figure 2-3 Worksheet of rapid upper limb assessment [40].

Table 2-2 Examples of observational methods adapted from [39].

Reference	Technique	Main features	Function
[41]	OWAS	Time sampling for body postures and force	Whole body posture recording and analysis
[42]	Checklist	Assessment of legs, trunk and neck for repetitive task	Checklist for evaluating risk factors
[43]	RULA	Categorization of body postures and force with action levels for assessment	Upper body and limb assessment Identification
[44]	NIOSH Lifting Equation	Measurement of posture related biomechanical load for manual handling	Identification of risk factors and assessment
[45]	QEC	Exposure levels for main body regions with worker responses, and scores to guide intervention	Assessment of exposure of upper body and limb for static and dynamic tasks
[46]	REBA	Categorization of body postures and force with action levels for assessment	Entire body assessment for dynamic tasks
[47]	PATH	Computerized work sampling of posture and activity	Non-repetitive work

- **Direct measurement:** Despite those abundant ergonomic estimation results reported by self-report and observational methods, more quantitative, objective, and accurate data is urgently required. In order to overcome the limitations, ergonomists also use other solutions for more precisely measuring the physical demands by means of different devices that can be directly attached on the human body for the measurement of exposure variables.

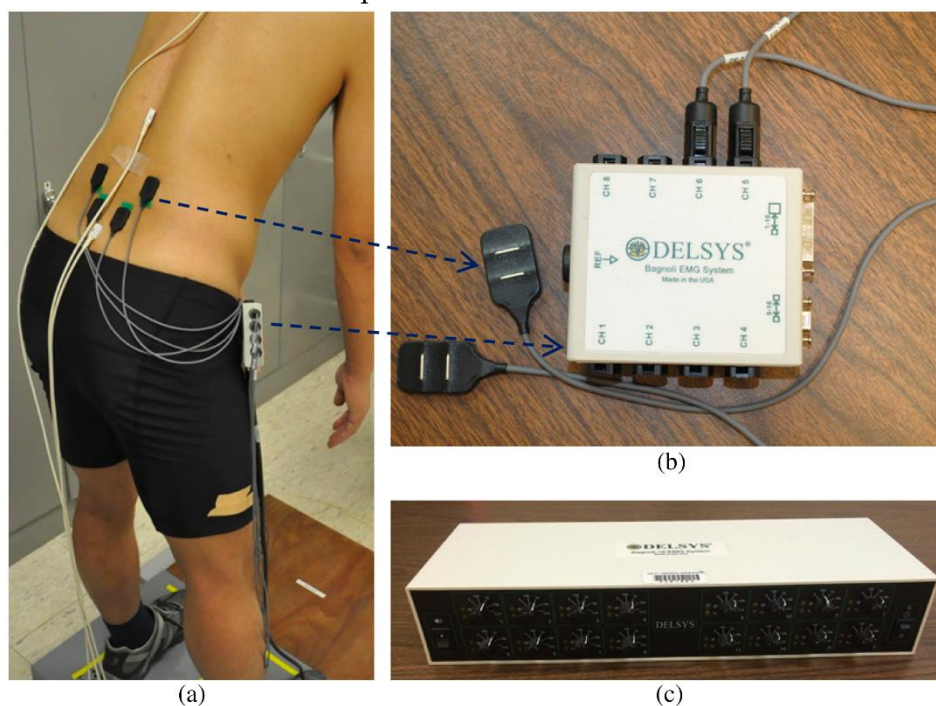


Figure 2-4 (a) Electromyography (EMG) sensors placed on the back; primary components of a desktop EMG system including (b) sensors and input module; and (c) main amplifier [48].

With the impact of many novel technologies, intelligent electronic components came into sight of ergonomic assessment studies. These methods range from simple, hand-held devices for the measurement of the range of joint motion to electronic goniometers that provide continuous recordings of the movement across joints during the performance of a task [39].



Figure 2-5 Industrial Lumbar Motion Monitor™ in real automotive workplace [49].

Some of the direct measurements methods provide lightweight portable devices for the measurement of body joint angles such as finger, wrist and forearm rotation together with corresponding system for computerized data analysis [50]. Others have been further developed for the simultaneous recording [51], myoelectrical activity recording [48] (Figure 2-4) and muscle fatigue [52], electronic exoskeleton such as Lumbar Motion Monitor [53][49] (Figure 2-5), or whole-day ambulatory monitoring of occupational work based on accelerometer sensors [54][55]. In addition, another type of direct measurement, has been developed for collecting posture data using optical, sonic or electromagnetic markers to specific anatomic points on the participant and are used with corresponding scanning units track the position and orientation in three dimensions [37], which is frequently used in film industry. However, equipment

cost, considerable expertise, data storage, usability in the field and data analysis time and error drifting over time can be a hindrance among some of the accelerometer sensors and gyroscope sensors [30][48] generally prevent them from using on large numbers of subjects or for long data collection.

Moreover, the attachment of non-ergonomic hardware device directly to the subject may result in discomfort and some modified work behaviours may occur [39]. For instance, most of the existing devices are using miscellaneous cables, which can result in distraction or discomfort sensations due to fear or risk that wires hook up with elements of the work environment. Table 2-3 introduced a brief comparison of most common direct methods.

There is no limitation to strictly use one single method to assess the risk factor. In fact, ergonomic expert tends more to redundant strategies composing multiple types of measurements to achieve the job. Manghisi et al. [56] developed a semi-automatic RULA evaluation software based on the Microsoft Kinect v2 depth camera, in order to detect awkward postures in real time and in off-line analysis.

Table 2-3 Examples of direct methods adapted from [39].

Reference	Technique	Main features	Function
[53]	LMM	Triaxial electronic goniometer	Assessment of back posture and motion
[50]	Electronic goniometry	Single or dual plane electronic goniometers and torsionometers to record joint posture	Measurement of angular displacement of upper extremity postures
[54][55]	Inclinometers	Tri-axial accelerometers that record movement in two degrees of freedom with reference to the line of gravity	Measurement of postures and movement of the head, back and upper limbs
[37]	Body posture scanning systems	Optical, sonic or electromagnetic registration of markers on body segments	Measurements of displacements, velocities and accelerations of a body segment
[52]	EMG	Recording of myoelectrical activity from exercising muscles	Estimation of variation in muscle tension and force application
[57]	Force measurement	Computer mouse with sensors recording forces applied to side and button	Determination of finger force exposures
[51]	CyberGlove	Lightweight glove incorporating 22 motion sensors and Uniforce pressure sensors	Measurement of wrist, hand and finger motion with superimposed grip pressure

2.2.4 Direct measurements for the human hand

The human hand is composed of a thumb, index finger, middle finger, ring finger, little finger, and palm, which includes the thenar eminence, the hypo thenar eminence, and creases [58]. The fingers contain 19 bones of distal phalanges, middle phalanges, and proximal phalanges, and metacarpal bones. Thus, the fingers have metacarpophalangeal (MCP), proximal interphalangeal (PIP), and distal interphalangeal (DIP) joints in sequence from the proximal to distal part, whereas the thumb has carpometacarpal (CMC), MCP, and interphalangeal (IP) joints. Figure 2-6 clearly depicts an illustration of anatomical human hand. Moreover, a major function of the CMC joints is to form the hollow of the palm, in order to conform the shape of the object being handled [59]. In contrast to the immobile CMC joints of the fingers, the first CMC joint is mobile, and the neutral state is defined when the thumb is positioned on the radial side of the palm, maintaining contact with the second metacarpal [60]. Table 2-4 shows the range of motion (ROM) on each fingers measured from different studies.

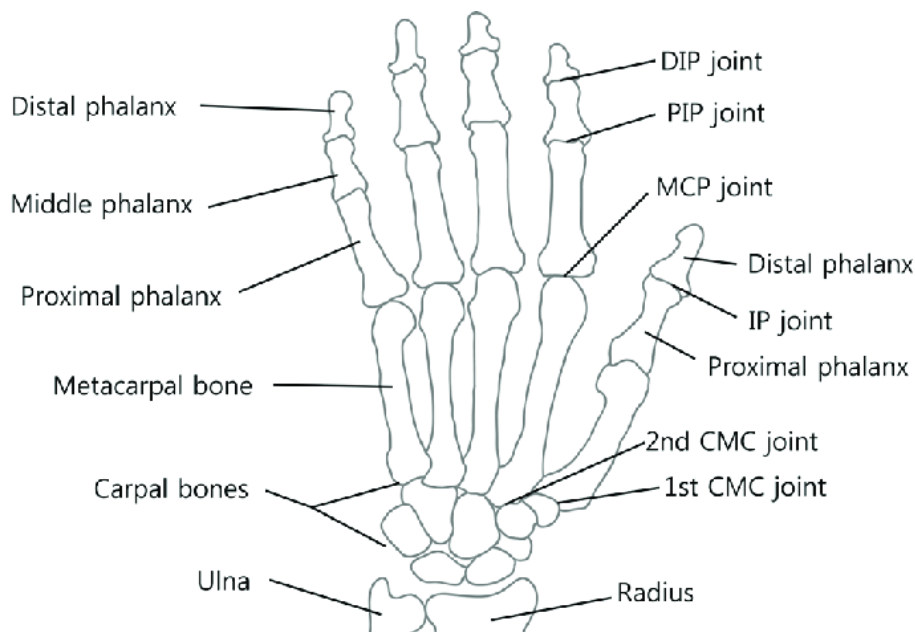


Figure 2-6 Anatomical drawings of the bones of the right hand (palmar view) [61].

This complex anatomy and the limited space in hands for hardware placement in comparison with other body regions, lead to

the existence of very few devices that directly measure hand movement. Following we summarized the state of the art of these devices. [62][63].

Regarding optical systems, Baker et al. [64] used a marker-based motion analysis system, known as VICON™ motion measurement system, to capture digit movements during typing and calculate digit angles, angular velocities, and angular accelerations for comparing the ergonomic differences between a standard keyboard and an ergonomic keyboard (Figure 2-7).

However, the occurrence of occlusions is one of the major problems in real workplace. Reconstructed joints may encounter critical errors in specific postures [65] or be occluded by the workstation. In addition, direct daylight conditions could also affect to the accuracy of the optical cameras [66] and the large device arrangement is hardly applied to the real sites which are in compact layout or the work type with frequent and wide range of movements.

Wang et al. [62] used CyberGlove®, which is supported by incorporating 18 flex sensors and Uniforce pressure sensors as the core technique for presenting a calibration approach for hand motion capture (Figure 2-8). In this study they indicated a satisfying sensor resolution of approximately 1° , repeatability $\pm 3^\circ$ and maximum nonlinearity of 0.6% from official CyberGlove specification [67].

Table 2-4 Range of motion of finger flexion in deg adapted from [58].

Finger	Swanson [74]	Becker and Thakor [73]	Chao [72]	Hume [71]	Degeorges and Oberlin [70]	Yoshida [69]	Zheng and Li [68]	Mean (STD)
Thumb	—	—	52.9	—	—	—	45	49 (6)
MCP	—	—	—	56	—	77	50	61 (14)
IP	—	—	—	—	—	81	80	81 (1)
MCP	62	71	83	—	97	—	85	80 (13)
PIP	—	104	101	—	110	—	100	104 (5)
DIP	—	61	73	—	57	—	80	68 (11)
MCP	64	85	90	—	100	—	—	85 (15)
PIP	—	104	103	—	114	—	—	107 (6)
DIP	—	74	80	—	57	—	—	70 (12)
MCP	67	85	88	—	107	—	—	87 (16)
PIP	—	107	105	—	110	—	—	107 (3)
DIP	—	67	75	—	57	—	—	66 (9)
MCP	64	86	90	—	105	—	—	86 (17)
PIP	—	99	103	—	111	—	—	104 (6)
DIP	—	71	78	—	58	—	—	69 (10)

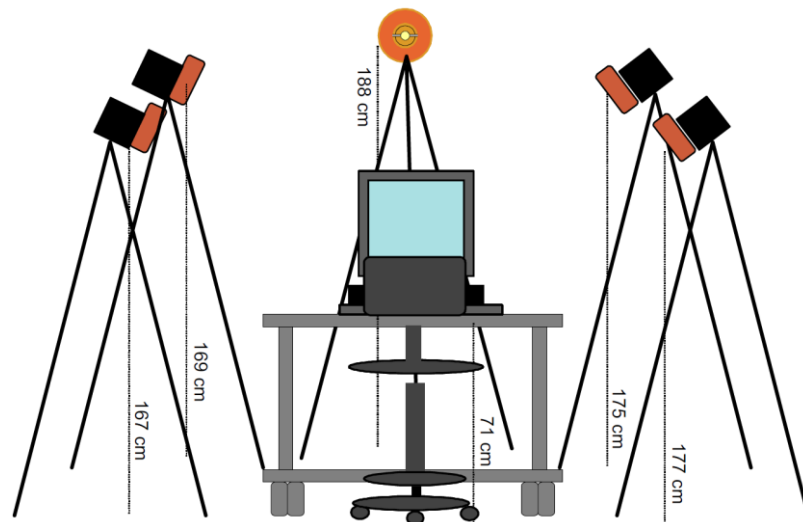


Figure 2-7 The VICON™ motion capture set-up [64].

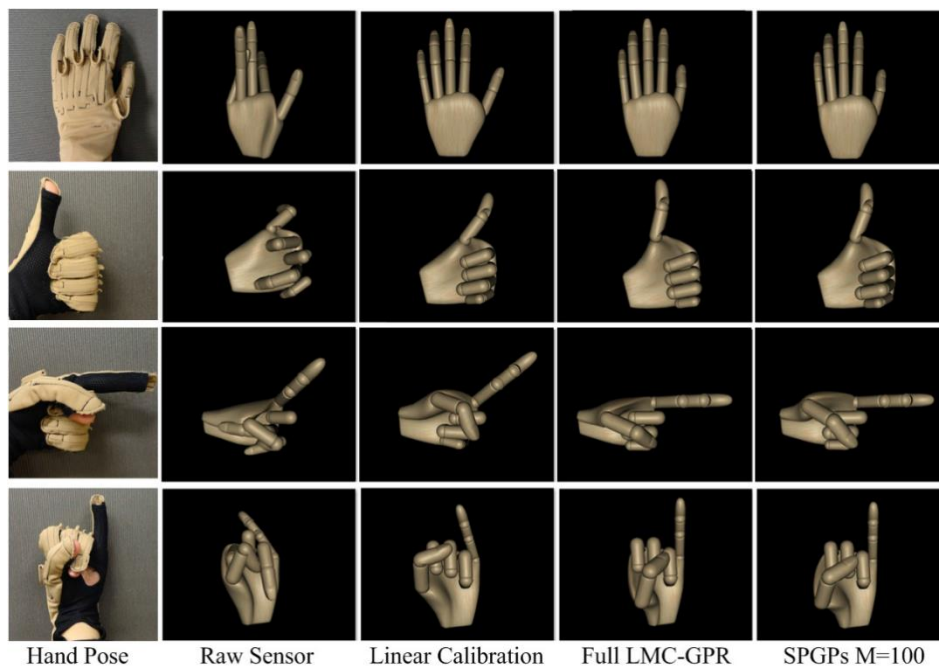


Figure 2-8 FK hand shape accuracy evaluation using different calibration methods. 4 commonly used hand poses are shown. The cross-coupled stretching effects (e.g. rIM ABD in “pointing” pose) are fixed by LMC-GPR and its SPGPs approximation [62].

Sama et al. [75] developed a low power and low-cost hand motion capture glove by utilising a set of flex sensors, gyroscopes and

accelerometers (Figure 2-9). Their prototype provides Bluetooth-based wireless node and has an estimated average working duration of 14 hours with a total cost around 150 € and low power consumption of 113 mW.

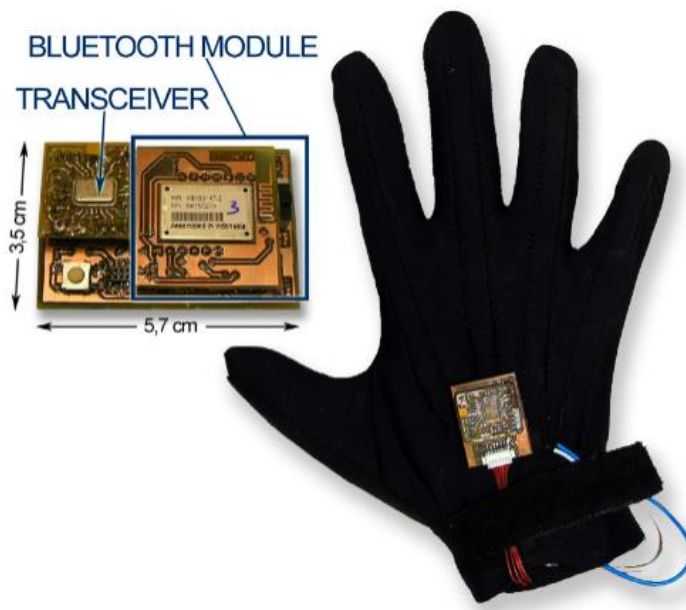


Figure 2-9 The 3dID glove and the gateway [75].

In terms of data loss through wireless node, the prototype has an acceptable packet loss (4.83%) distance of 5 meters between the gateway and the glove. However, the data accuracy is not clearly mentioned in the study.

Kitano et al. [63] presented a wearable finger motion measurement system using 9-axis inertial and geomagnetic sensors that works with the Euler angle system (Figure 2-10). The estimation error is within 4 millimeters. However, the practicability of the prototype is still needed to be improved for a real workplace in terms of the size of the wires and printed circuit board.

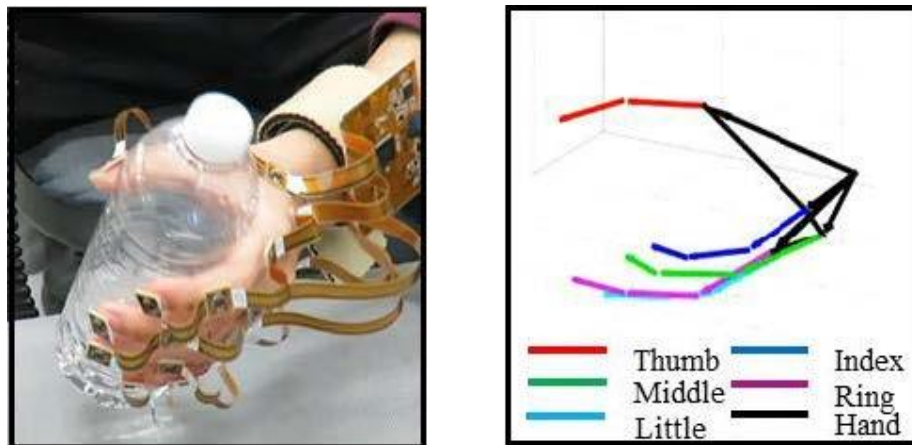


Figure 2-10 Finger motion (Left: Actual, Right: Measured) [63].

The majority of commercially available wearables are manufactured based on high-volume–low-mix economics and their designs are not tailored to specific requirements (e.g., body shape, aesthetic preference, etc.) of the users. Customization of wearables (e.g., hearing aids and prosthetics) using traditional manufacturing techniques often incurs high cost, which is passed on to the end user [76].

In short, for measuring instruments used in industrial production line scenarios, there are more requirements in terms of comfort, safety, and durability. Although the existing products have certain measurement accuracy guarantees, there are still disadvantages such as oversize, irrational design, and physical wiring. Therefore, research and development of a new generation of ergonomic measurement equipment is a work direction that can meet better user's expectations.

2.3 Additive Manufacturing

2.3.1 Introduction

Additive Manufacturing (AM), commonly known as 3D printing, is a booming technology that enables the computerized 3D solid model to be directly transformed to the final complex shape by adding materials

layer upon layer [77][78]. Figure 2-11 shows a common AM printing result that how layer height affects to the object's surface resolution.

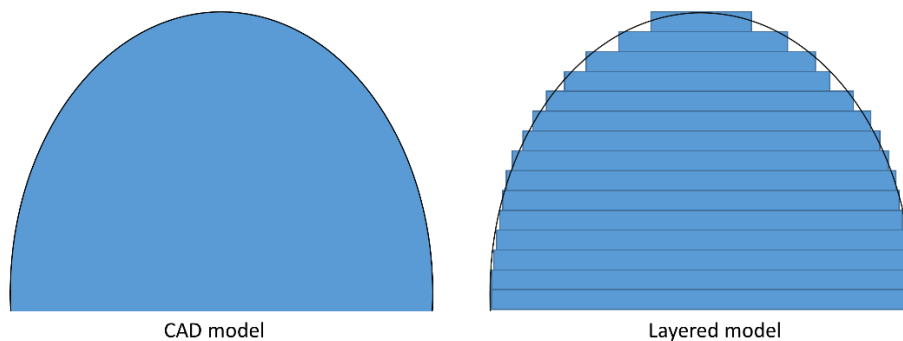


Figure 2-11 Front view of the object in typical AM process. (Left: Virtual 3D model in software, Right: Actual printing result)

Additive manufacturing has been widely applied in different fields, such as biomedical [79], biomechanical, construction [80], art [81], fast prototyping [82], electronics [82], aerospace [82] and military [83], due to the possibility of easily manufacturing customized products. Wohlers Associates envisioned that about 50% of 3D printing will revolve around the manufacturing of commercial products in 2020 [84].

2.3.2 AM printing technologies

Charles Hull developed the first AM technology in 1986 in a process known as stereolithography (SLA). Since then, subsequent developments such as powder bed fusion, fused deposition modelling (FDM), inkjet printing and contour crafting [78] were developed. This section briefly introduces the most important AM groups created by the American Society for Testing and Materials [85], all of them aimed to satisfy different materials, precisions, printing conditions, and workplaces.

- Powder bed fusion (Figure 2-12): Powder bed fusion processes consist of thin layers of very fine powders, which are spread and closely packed on a platform. The powders in each layer are fused together with a laser or an electron beam. Subsequent layers of powders are rolled on top of previous layers and fused

together until the final 3D part is built. The excess powder is then removed and if necessary, further processing and detailing such as coating or infiltration are carried out. Powder size distribution and packing, which determine the density of the printed part, are the most crucial factors to the efficacy of this method [78]. Selective Laser Sintering (SLS), Selective Laser Melting (SLM), Direct Metal Laser Sintering (DMLS) are AM processes under the Powder Bed Fusion family.

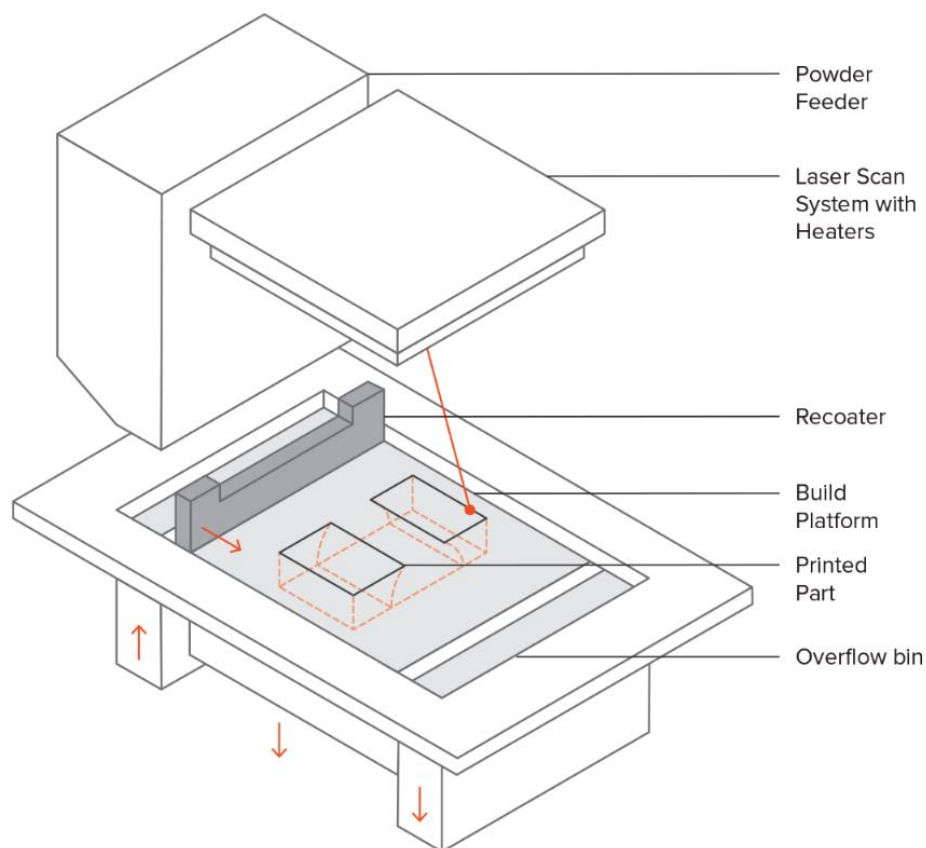


Figure 2-12 Schematic of an SLS printer [86].

- **Material Jetting (Figure 2-13):** It is one kind of inject printing whereby printheads are used to dispense droplets of a photoreactive ink that solidifies under ultraviolet light onto a substrate layer-by-layer. Wax-based inks and liquid suspensions are the two main types of inks in the market. The

particle size distribution of ceramics, viscosity of the ink and solid content, as well as the extrusion rate, nozzle size and speed of printing, are factors that determine the quality of inkjet-printed parts [87].

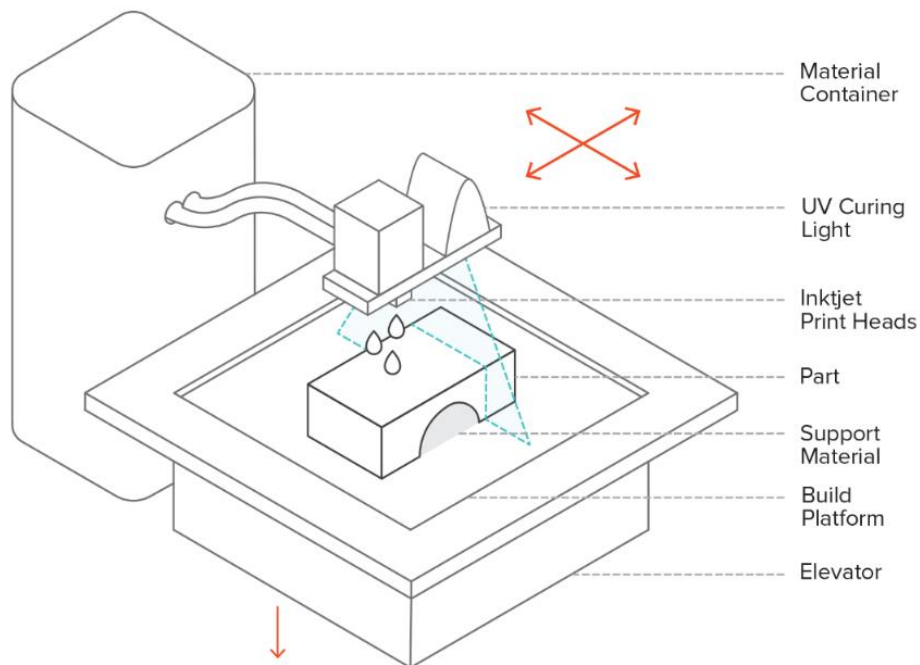


Figure 2-13 Schematic of a Material Jetting printer [86].

- Vat polymerization (Figure 2-14): Stereolithography is a kind of AM process which belongs to Vat Polymerization family. It uses UV light to initiate a chain reaction on a layer of resin or monomer solution. The monomers (mainly acrylic or epoxy-based) are UV-active and instantly convert to polymer chains after activation. After polymerization, a pattern inside the resin layer is solidified in order to hold the subsequent layers [78].

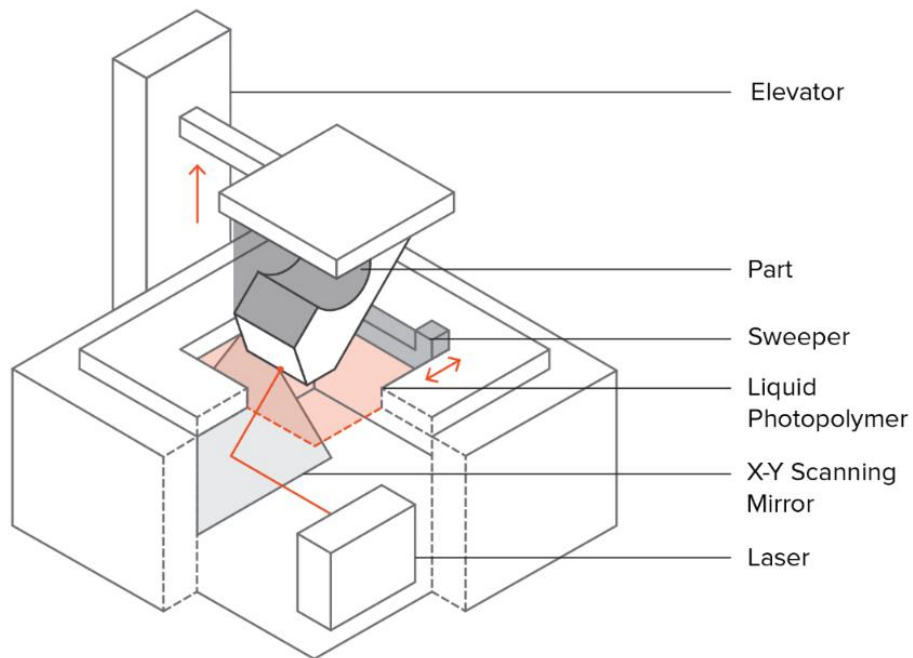


Figure 2-14 Schematic of an SLA printer [86].

- Material extrusion (Figure 2-15): Among AM devices, material extrusion is one of the fastest, lowest-cost, easiest-to-use and widely available techniques available on the market for AM printers [88] due to the expiry of key patents that lead to economy-friendly printers. In order to avoid conflict on protected acronyms, people use FDM, Fused Filament Fabrication (FFF), or Fused Layer Modelling (FLM) to name this additive manufacturing process that belongs to the material extrusion family.

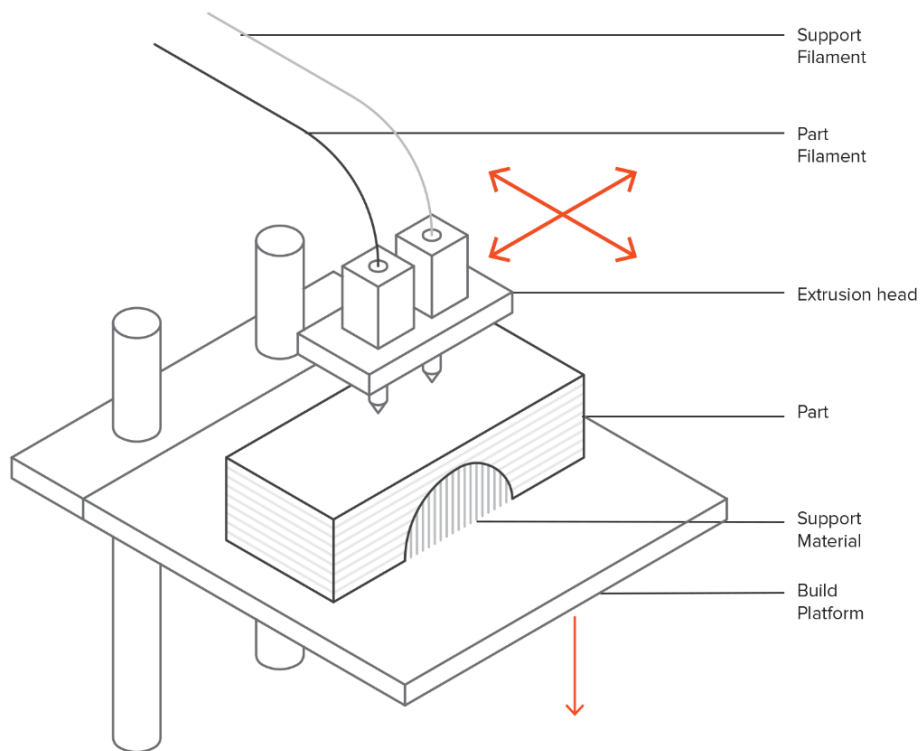


Figure 2-15 Schematic of a typical FDM printer [86].

The raw material used in material extrusion is supplied by a solid filament in a spool. The filaments are pushed into an extrusion head by a Direct Driver (setting on the top of the hotend) or Bowden Driver (away from the hotend), heated and molten in a specific chamber called “hotend”. While the driver is continuously supplying the solid filament into the extrusion head, a certain pressure is created inside the hotend, then the semi-liquid thermoplastic material is squeezed out of an orifice of a nozzle at the bottom of the head. Thus, the print head keep moving and traveling along the digital path controlled by a 3D printing software on a PC while selectively deposit the filament on a heated bed or the top of previously printed layers. Finally, the shaped material is solidified at room temperature after printing to form each layer of the object till the last. During material deposition, it is of great importance that the extrusion of hot polymer melts and the traveling printing head is well

concerted to each other. Furthermore, the molten extruded polymer must be deposited precisely. Any deviation will end up as an optical defect on the final part. The first layer of material is extruded on the printing platform, which also can be heated. Further layers are deposited directly on cooled down, solidified polymeric material. To ensure that there is a good connection between the existing layer and the new deposit layer, molten filaments are extruded with some contact pressure and overlap. The process is similar to a polymer welding process. The quality of weld lines between each layer is responsible for the mechanical and optical properties of the printed part. [89][4, 8, 22, 23]

2.3.3 Functional materials for AM in wearables

The development of AM technology has inspired the wearable designing field by the freedom of appearance and structure format. A wearable is a smart device that can be worn by a consumer and is composed of sensors that allow human physical activity and behaviour to be monitored [90].

Researchers are currently trying to develop wearables where AM technologies are used in the electronic part of the wearable [91]. As showed in Figure 2-16, several soft electronics for wearables are manufactured using a direct writing technique in order to deposit AgTPU on a textile substrate and a pick-and-place technique to mount integrated circuit (IC) chips during the printing process [92].

An nScrypt tabletop series 3D direct write dispensing system was used to deposit a stretchable silver conductor directly onto an elastic band in order to create Radio Frequency Identification (RFID) antennas [93]. Similarly, a glove with an embedded programmable heater, combining a 3D printer and the injection of liquid metal was developed to form the liquid-based circuit components [94], the schematic and electronics fabrication process is shown in Figure 2-17. However, most of those researches require high-cost equipment or can hardly be applied to office or household usage.

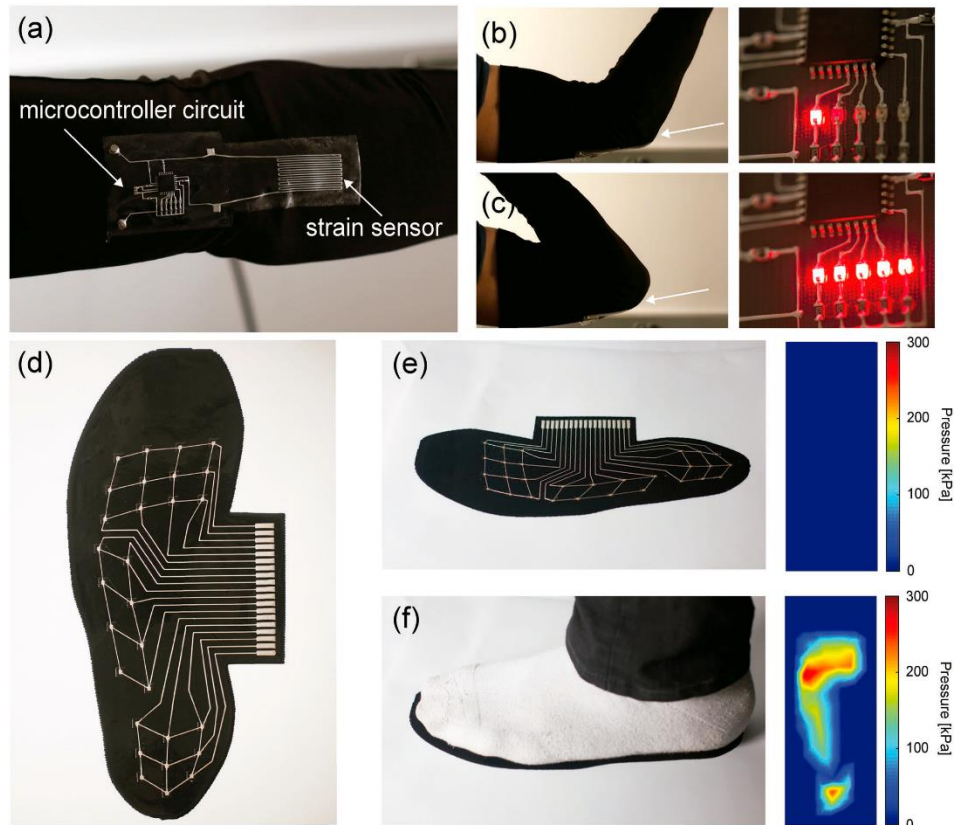


Figure 2-16 Wearable soft electronics fabricated by hybrid 3D printing: a) image of textile-mounted printed strain sensor and microcontroller circuit. b,c) Images of real-time function of the wearable strain device (identified with arrows) at modest and maximum joint bending, respectively, along with the corresponding LED readout. d) Image of plantar sensor array. e) Illustration of sensor array readout in the absence of applied pressure and f) upon the application of pressure by a human foot [92].

Due to the expiration of key patents, new functional materials are being developed for extrusion devices. Current commercial filaments, such as Acrylonitrile Butadiene Styrene (ABS) or Polylactic Acid (PLA), are hardly to meet specific functional requirements [95]. Aiming on this, the addition of nanomaterials into polymers for printing could enable the creation of high-performance functional composites [82]. Thus, researchers have focused on developing further composite materials mixed with several additives, fillers or reinforcements. A study from Tekinalp et al. [96] successfully reinforced composites made from carbon fiber and ABS resin feedstock and samples fabricated through FDM and compression-molding, which have been

evaluated and shows a significant increase in strength and stiffness. Moreover, a new attempt of nanomaterials was used to mix into the host matrix. The nanocomposites reveal many attractive properties, such as good thermal conductivity, enhanced fire performance, excellent strength and lightweight [97].

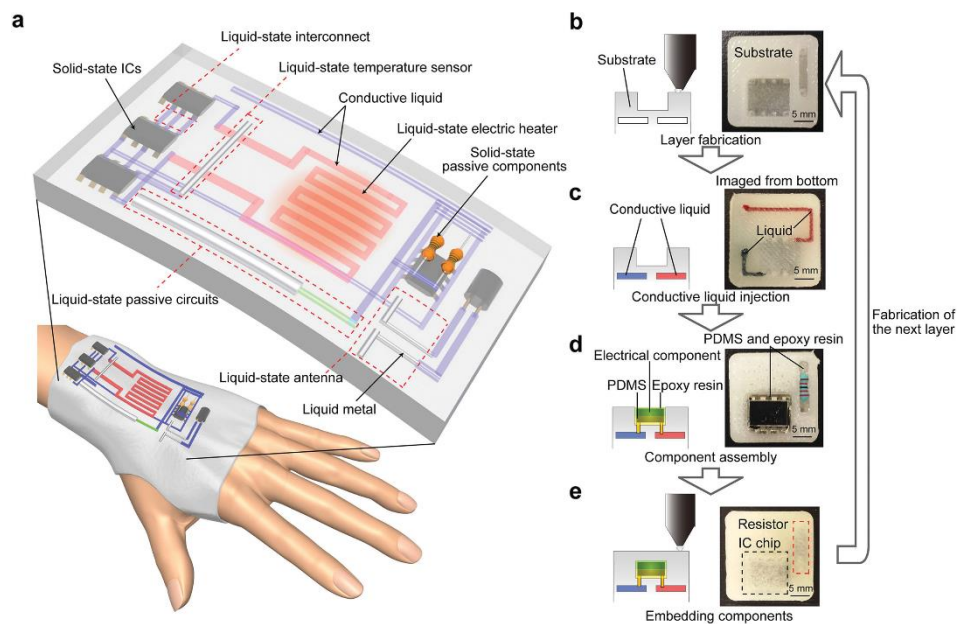


Figure 2-17 The multilayer schematic of a 3D printed smart object which integrates advanced IC chips and other solid state components, as well as liquid-state circuit components and liquid metal interconnects [94].

Not only to enhance the mechanical and chemical properties, researchers are starting to focus on electrical properties as well. In recent years, several studies have developed electrically-conductive compounds for extrusion devices based on a matrix of PLA or Thermoplastic Polyurethane (TPU) mixed with conductive powders. These commercial materials feature low resistivity (in ohm cm) and a reasonable cost per gram, as well as different stiffness values (12-150 USD). Various vendors and researchers are attempting to utilise conductive metal-based and carbon-based nanocomposites to replace traditional copper wires. Based on the reviewed study by Diogo et al [98], the prevailing type of conductive polymer matrix appeared in the commercial market is categorized as follow:

- Carbon Nanotubes (CNT): CNT are well known for their optimal mechanical, electrical and thermal properties. But the aggregation in polymeric solutions of CNT is possibly causing blockages at the nozzle and flux instability while printing [98].
- Graphene (Gr): this type of polymer matrix has been widely used in some novel electronic applications, for instance, sensors, trackpads, or electromagnetic. Graphene exhibits a range of exceptional properties such as low resistivity, excellent thermal conductivity, high electron mobility, and optical transparency. Due to the structural rigidity and poor liquid-phase processing capability of graphene sheets, low mechanical performance (including strength, toughness and resiliency) is the most challenging shortcomings for Gr-based polymers to overcome.
- Carbon Black (CB): carbon Black is a form of paracrystalline carbon that is formed by the accumulation of spherical or chain particles with an average diameter of 5 to 30 nm. It is commonly filled with ABS (CB-ABS) for printing basic capacitance. Moreover, CB is also used with graphene and copper as a better conductive composite, which was developed and used to embed LED as horn antennas [99] with extraordinary electrical properties and certain flexibility.
- Carbon Fibers (CF): it is popular in aerospace, civil engineering, military, racing, and other competitive sports products due to its properties of high tensile strength and flexural strength, light weight, etc. CF has been utilized to fill with conductive silicon rubbers (CSRs) for developing better electrical and mechanical properties. Huang et al. (2018) [100] found an anisotropic electrical and mechanical behaviour, in which the volume resistivity at the orientation direction was 6.8 times lower than that at perpendicular direction in particular.

More importantly, all of them are intended to be used with low-cost 3D extrusion printers without any particular add-on. Nonetheless, as far as the authors know, existing studies 3D-print the conductive filament so as to connect simple passive electronics, while in the literature there aren't references where these materials are used for connecting MEMS sensors.

2.4 Conclusions

This chapter covers the two big knowledge areas to achieve the aim of this project, that is, to develop a wearable device that incorporates new AM functional materials for tracking worker's hand movements in an automotive assembly plant so as to subsequently analyse if the worker is exposed to WMSDs. After depicting the current status of both fields several conclusions are obtained:

- MSDs present a major occupational healthcare problem in automotive manufacturing industry. However, although important, the hand region is undervalued in terms of MSDs exposure risks and its consequences among most of the epidemiology studies. Designing measurement device for hands is a challenge due to the flexibility of range of movement, the skeleton complexity and limited space in fingers and palm.
- Comparing the three types of ergonomic assessments from different researches, direct measurement is becoming a trend and is more frequently used by experts. An intelligent electronic measurement device is suitable for the situations that require objective measuring result and high accuracy, while sufficient expertise and funds are needed for preparation.
- Current direct measurement tools are hard to apply for tracking fingers movements in real workplace, in terms of sight occlusions, data drift, unreasonable size, and short duration.
- Among most of the studies focusing on hand measuring, a glove-like pattern is widely accepted and considered as a wearable device. However, those prototypes are still incorporating copper wires and standard Printed Circuit Board (PCB), which constrain the development of user-friendly devices for being used in real industrial environments.
- The material extrusion technology has met the demands of customization of wearable device and specific ergonomic demands for individuals. There are remarkable advantages in terms of high reliability, cost-effective, good freedom of designing and modifying. Moreover, numerous functional printing materials are able to be printed by dual-extrusion 3D printers, including conductive filaments. Such kind of

conductive nanopolymer materials inspire the potential of developing and 3D printing MEMS electrical elements.

Chapter 3:

Assessment of ergonomic methods

3.1 Introduction

In order to find a reliable and practical methodology for measuring and analysing the hand region, an evaluation of several ergonomic methods is carried out in this chapter. Due to each assessment method features advantages and drawbacks, there is no optimal universal method for all body regions. Herein, several criteria arranged by the steps to follow in the measuring process will be formulated in a questionnaire. Later on, several interviews based on the questionnaire will be carried out with ergonomic specialists to know their preference, requirement and expectation on the ergonomic methods will be determined. Finally, the design principles for hand region wearable measurement will be summarized, and one feasible technology will be selected.

3.2 Selection of the ergonomic methods

The first step is the selection of the ergonomic methods that specialist will evaluate in a subsequent step. For this step, seven of the prevailing ergonomic methods are selected:

- 1) Assessment of Repetitive Tasks (ART) Tools
- 2) Rapid Upper Limb Assessment/Rapid Entire Body Assessment (RULA/REBA)
- 3) Biomechanical Assessment (BA)
- 4) Optoelectronic Systems (OES)
- 5) Electro Goniometer (EG)
- 6) Accelerometry (ACC)
- 7) Inertial Measurement Unit (IMU).

These methods are selected mainly based on a combined consideration of fully covered on self-report, observation, and direct measurement from various reviewing studies ([101], [48], [102], [37] and [103]). Only those representative methods which frequently mentioned or used in studies are considered. These methods are described in the following subsections.

3.2.1 Assessment of Repetitive Tasks (ART)

ART tool was developed by the Health and Safety Executive (HSE) in UK for estimating repetitive tasks usually behaved on assembly, production, processing, packaging, and storing works [104]. This method focuses on the posture of the upper limb, neck and trunk by scoring the level of exposure to identify the risk factors and its potential incentives to MSDs.

The ART process involves: completing the task description form, following the flow chart or assessment guide to make an assessment, and, finally, completing the score sheet.

The task description form, as can be seen in Figure 3-1, includes first, the measurement of frequency and repetition of movements, secondly the force measurement, thirdly the identification of awkward postures, and the last stage are additional factors such as breaks,

workplace, duration, etc. For each stage, the levels of risk for each risk factor, are classified by understandable coloured traffic lights. With the task score determined by completing the score sheet, significant risks are able to be identified.

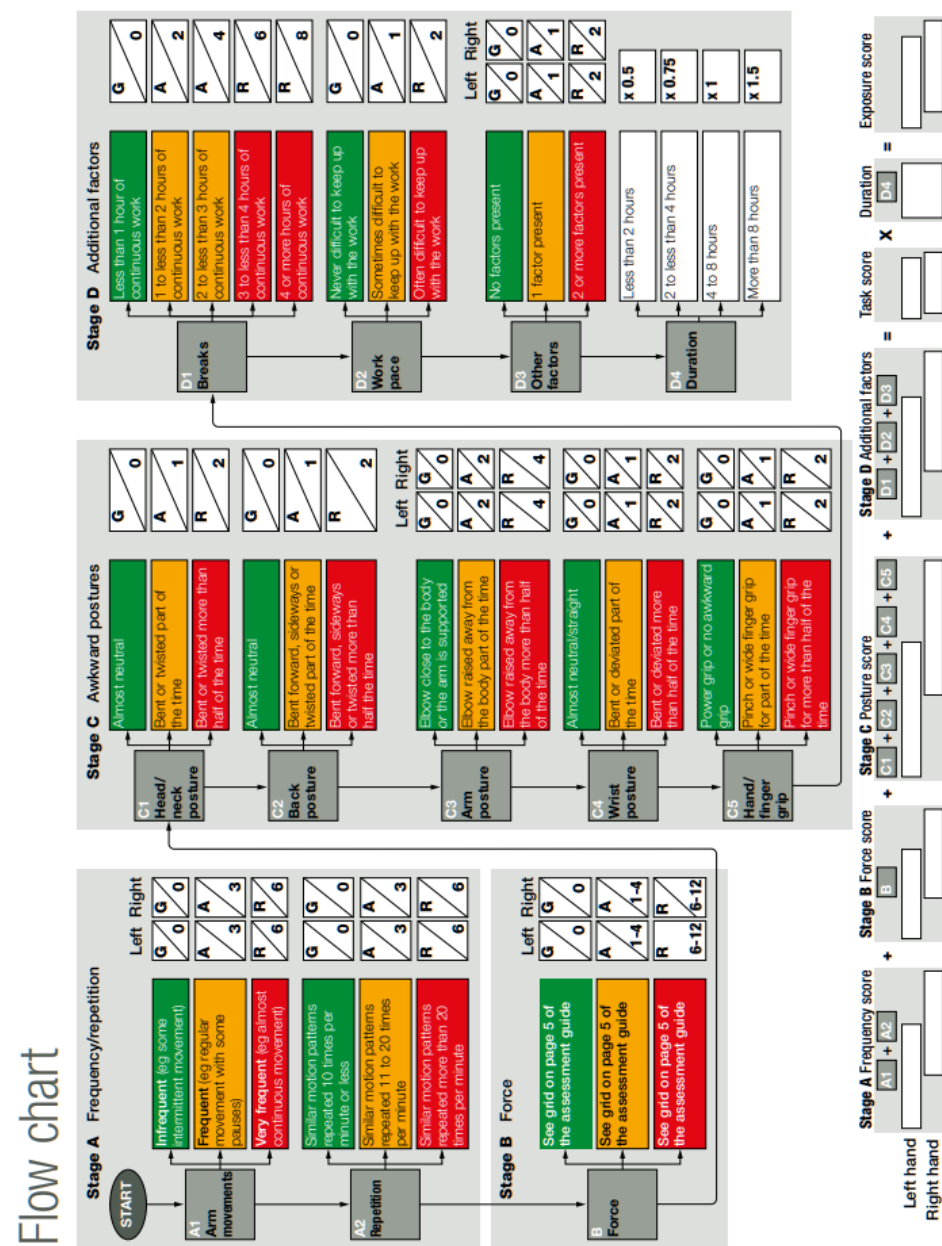


Figure 3-1 The frequency/repetition stage of ART [104].

The task scores and exposure scores help to prioritise those tasks that need most urgent attention and help check the effectiveness of any improvements [104]. Figure 3-1 shows the flow chart that a risk assessment expert subjectively evaluate while the subjects are doing their tasks.

3.2.2 Rapid Upper Limb Assessment (RULA) and Rapid Entire Body Assessment (REBA)

The RULA method was developed by McAtamney et al. [43] in 1993 for evaluating the posture of the neck, trunk and upper limbs along with muscle function and the external loads on the body (see Figure 2-3 on Section 2.2.3). Ergonomic investigation is conducted by coding an action list which contains a set of fixed body angles, and obtaining the scores for judging whether a movement is acceptable or risky.

This REBA assessment method was developed based on RULA by Hignett and McAtamney [46]. Apart from the same postures taken from RULA, this method extended it by visually evaluating the positions of the legs, awkward position in upper limbs and considering postural loading factors [101]. Figure 3-2 shows an example of the REBA method. The ergonomist will follow the steps to evaluate the tester and obtain several region scores to fill table A, table B and table C in order. Then with the table value and additional steps, score A, score B and score C will be carried out. At last, the final REBA score will be obtained by summing up table C score with activity score.

Morgan Maxwell
Chartered Ergonomists

REBA Employee Assessment Worksheet
Hignett, S. and McAtamney, L. (2000) Rapid Entire Body Assessment: REBA, Applied Ergonomics, 31, 201-5.

TABLE A - Neck, Trunk and Leg Analysis

Step 1: Locate Neck Position
+1 (20°) +2 (15° flexion) +3 (20-60°)

Step 1a: Adjust...
- If neck is twisted: +1
- If neck is side bending: +1

Step 2: Locate Trunk Position
+2 (in extension) +1 (0°) +2 (20-60°)

Step 2a: Adjust...
- If trunk is twisted: +1
- If trunk is side bending: +1

Step 3: Legs
+1 +2 +3 +4

TABLE B - Arm and Wrist Position

Step 7: Locate Upper Arm Position
+1 (20°) +2 (in extension) +3 (20-45°) +4 (90°)

Step 7a: Adjust...
- If shoulder is raised: +1
- If upper arm is abducted: +1
- If arm is supported or person is leaning: -1

Step 8: Locate Lower Arm Position
+1 (100°) +2 (60°)

Step 9: Locate Wrist Position
+1 (15°) +2 (15°+)

	NECK		
	1	2	3
Legs	1 2 3 4	1 2 3 4	1 2 3 4
Trunk Posture Score	1 2 3 4 5 6 7 8 9	1 2 3 4 5 6 7 8 9	1 2 3 4 5 6 7 8 9
Upper Arm Score	1 2 3 4 5 6 7 8 9	1 2 3 4 5 6 7 8 9	1 2 3 4 5 6 7 8 9
Lower Arm Score	1 2 3 4 5 6 7 8 9	1 2 3 4 5 6 7 8 9	1 2 3 4 5 6 7 8 9
Wrist	1 2 3 4 5 6 7 8 9	1 2 3 4 5 6 7 8 9	1 2 3 4 5 6 7 8 9

SCORE A (score from table A + load/force score)

1	1	1	2	3	4	5	6	7	8	9	10	11	12
2	1	1	2	3	4	5	6	7	8	9	10	11	12
3	2	3	3	4	5	6	7	8	9	10	11	12	12
4	3	4	4	5	6	7	8	9	10	11	12	12	12
5	4	4	5	6	7	8	9	10	11	12	12	12	12
6	6	6	7	8	9	10	10	10	10	10	10	10	10
7	7	7	7	8	9	10	10	10	11	11	11	11	11
8	8	8	9	10	10	10	10	11	11	11	11	11	11
9	9	9	10	10	10	11	11	11	12	12	12	12	12
10	10	10	11	11	11	12	12	12	12	12	12	12	12
11	11	11	12	12	12	12	12	12	12	12	12	12	12
12	12	12	12	12	12	12	12	12	12	12	12	12	12

SCORE B (table B value + coupling score)

1	1	2	3	4	5	6	7	8	9	10	11	12
2	1	1	2	3	4	5	6	7	7	7	7	7
3	2	3	3	4	5	6	7	8	8	8	8	8
4	3	4	4	5	6	7	8	9	9	9	9	9
5	4	4	5	6	7	8	9	9	9	9	9	9
6	6	6	7	8	9	10	10	10	10	10	10	10
7	7	7	7	8	9	10	10	10	11	11	11	11
8	8	8	9	10	10	10	10	11	11	11	11	11
9	9	9	10	10	10	11	11	11	12	12	12	12
10	10	10	11	11	11	12	12	12	12	12	12	12
11	11	11	12	12	12	12	12	12	12	12	12	12
12	12	12	12	12	12	12	12	12	12	12	12	12

Step 4: Look-up Posture Score in TABLE A
Using values from steps 1-3 above.

Step 5: Add Force/Load Score
- If load < 11 lbs: +0 - If load 11 to 22 lbs: +1
- If load > 22 lbs: +2

Step 5a: Adjust...
- If shock or rapid build up of force: add +1

Step 6: Score A = [] + [] = []

Step 6: Score B = [] + [] = []

TABLE C - Step 6: Score A, Find Row in Table C
Add values from steps 4 & 5 to obtain Score A. Find Row in Table C.

SCORE A	SCORE B	ACTIVITY SCORE
1	1	1
2	1	2
3	2	3
4	3	4
5	4	5
6	6	6
7	7	7
8	8	8
9	9	9
10	10	10
11	11	11
12	12	12

Step 7a: Adjust...
- If shoulder is raised: +1
- If upper arm is abducted: +1
- If arm is supported or person is leaning: -1

Step 9a: Adjust...
- If wrist is bent from midline or twisted: Add +1

Step 10: Look-up Posture Score in TABLE B
Using values from steps 7-9 above. Locate score in Table B

Step 11: Add Coupling Score
- Well fitting Handle and not long power grip: good: +0
- Acceptable but not ideal hand hold or coupling acceptable with another body part: fair: +1
- Hand hold not acceptable but possible: poor: +2
- No handles, awkward, unsafe with any body part: Unacceptable: +3

Step 12: Score B, Find Column in TABLE C
Add values from steps 10 & 11 to obtain Score B. Find column in Table C and match with Score A in row from step 6 to obtain Table C Score.

Step 13: Activity Score
+11 or more body parts are held for longer than 1 minute (static)
+1 Repeated small range motions (more than 4x per minute) +1
Action causes rapid large range changes in postures or unstable base

FINAL REBA SCORE [] + [] = []

SUBJECT: [] **COMPANY:** [] **DEPARTMENT:** [] **SCORER:** [] **DATE:** []

Figure 3-2 Worksheet of REBA [105].

3.2.3 Biomechanical Assessment (BA)

Biomechanical Assessment (BA) is a kinetic analysing system focus on human body limbs. Using motion capturing devices, experts collect and process movements data. The basic data are commonly later used for mathematical modelling, such as inverse kinematics analysis and finite element analysis. This method tends to utilize algorithms to obtain key biomechanical metrics, such as joint torque, joint reaction force, major muscle forces around the joints, and muscle activity. Apart from direct measurements, researches on the relationships between joints movements and its forces, and between body regions and machine are also included in BA. Currently, several computerized software packages such as Three-Dimensional Static Strength Prediction Program (3DSSPP, Figure 3-3) [106], OpenSim [107], Visual 3D [108], and AnyBody [109] are available to estimate joint loadings and are proven to have the potential of processing motion data captured by remote sensing [110]. Figure 3-3 shows an operating interface of 3DSSPP.

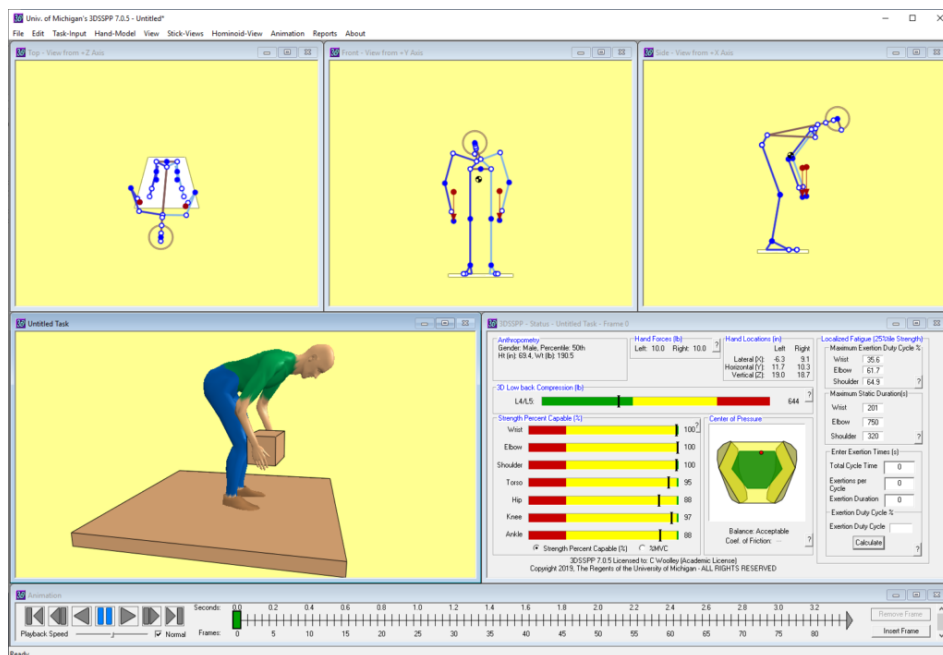


Figure 3-3 A lifting posture entered in the 3D SSPP window

3.2.4 Optoelectronic Systems (OES)

It is a motion capture system that needs a distributed camera network system to track human movement. This movement can be achieved either by marker-based system or by marker-less system.

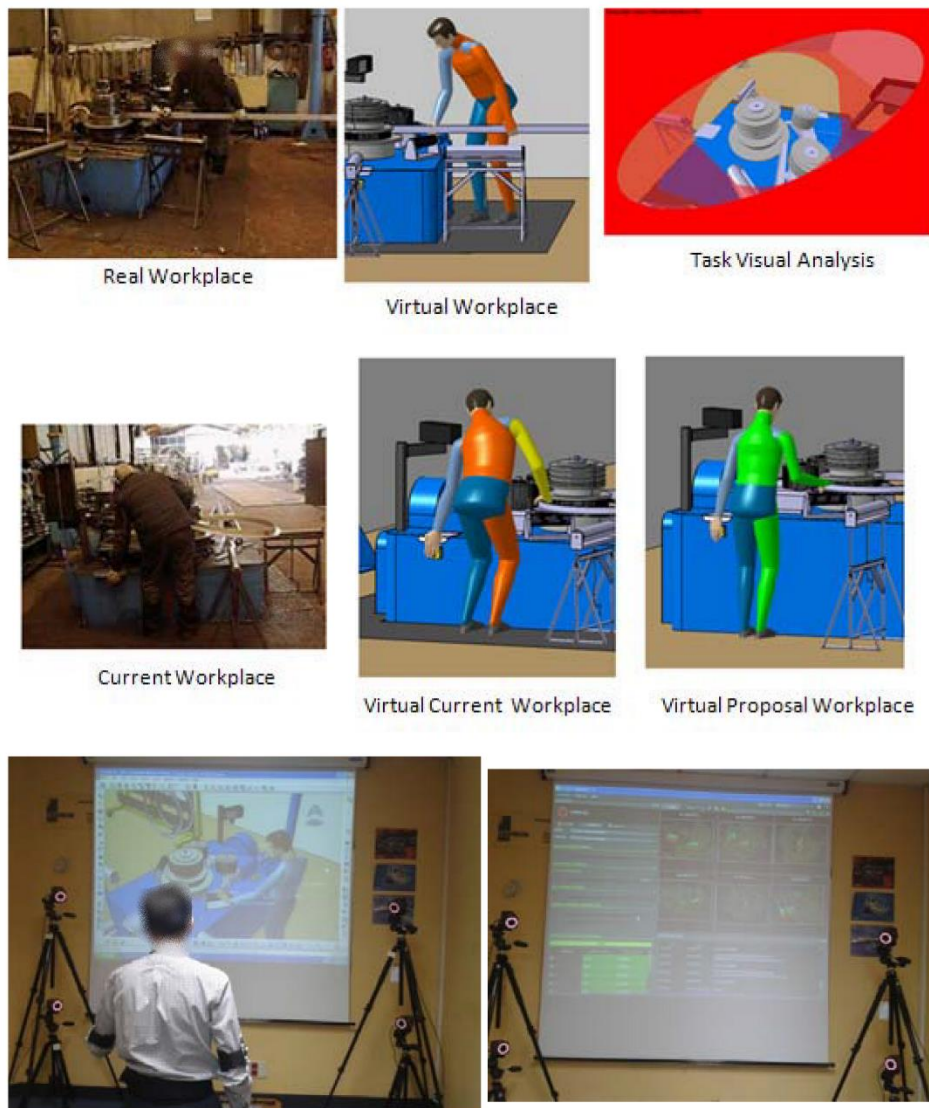


Figure 3-4 Real task, virtual task ergonomic evaluation and Motion Capture System laboratory workplace [111].

The marker-based approach relies on sensors attached to the human body; a receiver processes the signals from these sensors to

reconstruct the shape of the body and detect its movements [112] [113]. VICON for instance, used some infrared cameras that are pointed to a working space. This system requires a certain room scale space, multiple cameras with resolution up to 2048x1088 [114], a three-axes grid on the ground for global frame of reference, an acquisition system for recording and saving synchronous video data, moreover, several processes such as markers configuration, initialization, camera calibration, world coordinate system alignment, background subtraction, skeleton body modelling, and post-processing are needed [115] [116]. The price of a complete marker-based system can reach around 55,000 EUR.

These cameras transmit the movement of the markers to a computer where a distributed estimation algorithm is set up to track human motion used an information-weighted consensus filter (ICF) as a distributed estimation algorithm to track human motion in a camera network inside the sensing range. Figure 3-4 shows a laboratory workplace set up of mark-based systems study.



Figure 3-5 A ConvNet-based marker-less motion capture algorithm reconstructs joint angles of multiple people performing complex motions in outdoor settings, such as in this scene recorded with only three mobile phones: (left) 3D pose overlaid with one camera view, (right) 3D visualization of captured skeletons [102].

The marker-less approach uses affordable, unobtrusive devices ranging from a webcam and digital single-lens reflex (DSLR) camera to video recorders and depth sensing cameras, and uses computationally intensive techniques to recognize depth information in 2D projection from recorded images [117]. This type of systems is

more focus on the image detection method and algorithm development. For example, a study presented an approach unites a discriminative image-based joint detection method with a model-based generative motion tracking algorithm through a combined pose optimization energy (Figure 3-5) [118]. The price of a complete commercial marker-less system, as Kinect for instance, can be around 5,000 EUR. Figure 3-6 shows a study of angles precision comparison between marker-based system and marker less system.

	Hip	Hip	Hip	Knee	Ankle	Ankle	Ankle
	AA	InEx	FE	FE	InEv	InEx	DP
Mean mkl (deg)	3.4	4.6	37.4	-21.6	1.6	-6.1	93.6
SD mkl (deg)	3.7	9.6	11.3	4.0	3.8	8.6	3.8
Mean mb (deg)	5.6	3.2	16.8	-20.9	-0.4	-10.6	42.6
SD mb (deg)	6.3	11.6	7.4	32.2	10.2	37.3	22.3
Mean RMSD (deg)	14.1	21.6	17.6	11.8	7.0	12.9	7.2
SD RMSD (deg)	2.3	9.3	8.5	2.5	3.6	7.0	1.8
Min RMSD (deg)	9.6	7.7	6.4	8.1	3.4	5.3	5.0
Max RMSD (deg)	17.3	34.7	29.0	16.0	13.8	29.4	11.0
RMSD % range of motion	91.5	129.6	44.7	18.3	54.8	88.2	33.1

Each joint rotation RMSD % of the marker-based range of motion is reported. Each joint rotations mean, standard deviation (SD), minimum (Min) and maximum (Max) values are also reported: Abduction-Adduction (AA), Flexion-Extension (FE), Internal-External Rotation (InEx), Inversion-Eversion (InEv), Dorsi-Plantarflexion (DP).
doi:10.1371/journal.pone.0087640.t001

Figure 3-6 Description of root mean square distance (RMSD) values between angles calculated with the two techniques (marker-less (mkl) and marker-based (mb)); mean, standard deviation, minimum (Min) and maximum (Max) RMSD values are reported [115].

3.2.5 Electro Goniometer (EG)

Electro goniometers are one of the most popular instruments in laboratory measuring and clinical monitoring. It uses a strain gauge spring connected to two rigid bodies in order to determine both active and passive Range of Motion along one single axis. It is used to measure local (internal) joint angles during human movement by attaching it across two or more joint segments. The corresponding angular output can then be used for quantitative clinical evaluation [119].

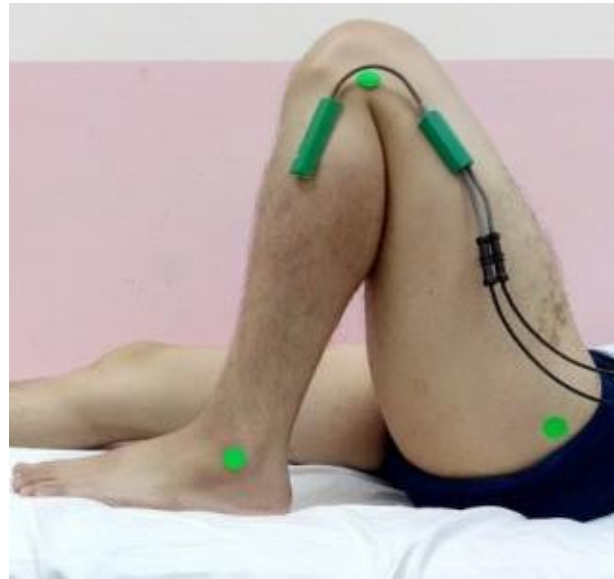


Figure 3-7 Placement of EG [119].

3.2.6 Accelerometry (ACC)

Accelerometers measure acceleration, direction, and angles (with more than one accelerometer) through a linearization technique. This system integrate an accelerometer sensor into comfortable garments or directly attached to the human body [120] for actively monitoring multi-axis angles in real-time. By combining sensors with actuators, wireless communication modules and signal processing units, different viable real-time wearable health monitoring systems could be developed for various applications such as activity monitoring, fall detection, gait pattern and posture analysis [102]. Figure 3-8 shows an application of measuring knee angle using smartphone integrated with accelerator sensors.



Figure 3-8 Experimental set-up using the isokinetic dynamometer and smartphone placed at the anterior medial surface of the tibia [121].

3.2.7 Inertial Measurement Unit (IMU)

The microelectromechanical technology has significantly reduced the size of electronic components and allow the development of small and wearable devices. The Inertial Measurement Unit is one of these applications, integrating sensors together, such as accelerometers, magnetometers, and gyroscopes. It is able to measure acceleration, velocity, orientation, and the Earth's gravitational forces and magnetic

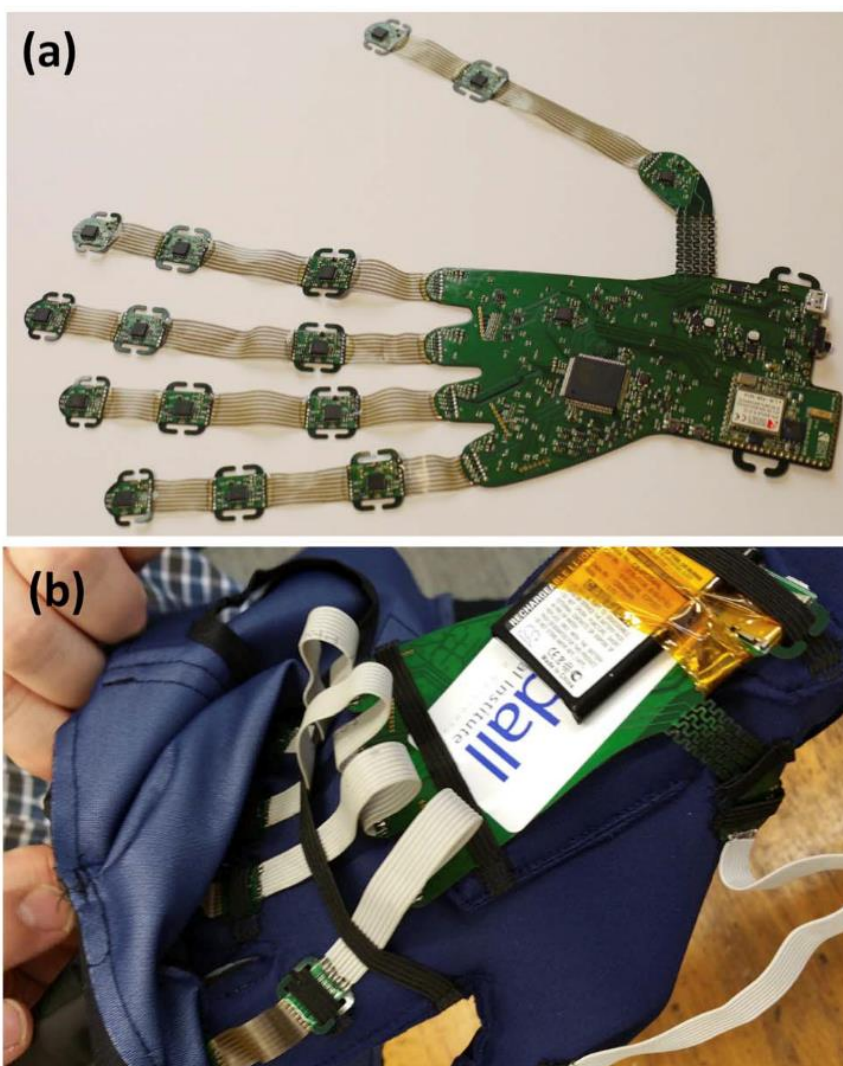


Figure 3-9 (a) Configuration of the IMU data glove showing individual IMU's for each finger joint. (b) Integration of the IMU data glove into a two-layered glove structure [122].

fields in real time. However, the cumulative drift error, a difference between the actual position and system detected position is the main deficiency. Growth of quadratic error in position and linear error in velocity occurs due to constant error of acceleration in the time of integration. On the contrary, quadratic error in velocity and growth of cubic error in position appears because of constant error of gyroscope [123]. To mitigate drift error, MEMS based low cost system provides a new approach. These capabilities have raised significant interest among researchers aiming to measure postures and body motions in various contexts, from daily activities (e.g. walking, running and sitting) to complex work-related tasks (e.g. climbing, hammering and lifting) [101]. Figure 3-9 shows an application of IMU sensor-based data glove for clinical finger movement analysis.

3.3 Questionnaire: criteria

The suitability of each method is evaluated through several questions grouped by timing, that is, the evaluation of how good this method is before, during, and after the ergonomic measuring. The structure of assessing metrics is built and optimized according to a workload evaluating guideline of an American aircraft company, which named as Assessment of Crew Workload Measurement Methods, Techniques and Procedures [124]. Questions require to fill some basic information such as target body region and work attribute, and a yes/no answer or followed a five-level Likert Scale from negative (1) to positive (5) (Figure 3-10). As showed in Table 3-1, Table 3-2 and Table 3-3, each metric is explained with a combination of description, example scenarios and after reading this information of each metric the expert has to answer their corresponding question.

		RULA / REBA							
		Rapid Upper Limb Assessment / Rapid Entire Body Assessment							
Description									
Before measuring	Body Region: Can you tell us the body regions this method could be applied to?	Repetitive movements							
		Nonrepetitive movements							
		High loads							
		Low loads							
		Static loads							
		Dynamic loads							
		Work attribute: What is the type of work this method can measure? (Yes or No)	negative	1	2	3	4	5	positive
		Validity: How good can this method measure _____?							
		Movement repetition							
	While measuring	Independence: Can this method work alone or need another associated method to optimize it?							
Numbers: How objective/subjective this method is when analysing the ergonomics?									subjective
Learning difficulty: How difficult is the learning process to apply this method?									expertise
Physical space: What is the required room space so as to hold the experiment?									much
Equipment costs: How expensive is the necessary equipment to run ergonomic assessment?									high
Preparation time: How much preparation time does this method need to start the assessment?									much
Operating difficulty: How hard is it to apply this method in reality?									laboratory
Test time: How much time does this method need to evaluate the ergonomics?									much
Inter-rater: How similar are the results if you use twice this method to measure?									different
Manual error: How similar are the results if two different testers use this method to measure the same person?									different
After measuring	Psychological collaboration: Do workers need the help in psychological aspect from tester during the test?								easy
	Physical collaboration: Do workers need the help in physical aspect from tester during the test?								much
	Safety: How dangerous is the application of this method for the worker?								high
	Result communication: How understandable are the results achieved with this method?								low
	Correlation: How close are results from this method with results from other method when evaluating the same work?								low
	Career threat: Can results from this method be a health concern for workers without a previous ergonomic background?								high
									low

Figure 3-10 Sample of questionnaire (RULA/REBA) for evaluation.

3.3.1 Before measuring

Table 3-1 Definition of each Criteria: Before measuring

Metric	Description	Scenario
<i>Validity</i>	The extent to which an actual method is able to measure the desired workload features.	Tester A wants to know the sudden impacts when workers are installing the centre panel.
<i>Independence:</i>	The ability of measuring the variable representatively without any reference to other measurement in most of the use.	Testers think the strength result of this force measuring instrument is only able to measure static and consistent force. They usually have to add another sensor to measure impact force on the hand.
<i>Numbers</i>	The ability of which a measurement addresses levels for each metrics.	This force measuring method offers real-time data (objective numbers), while workload assessment scale is based on workers' feeling (subjective opinion).
<i>Learning difficulty:</i>	The difficulty the researcher has to understand the entire measurement system in a short term.	An intern tester took 3 days to know how to use force measuring method and 1 week for mastering under supervision, while most of such measurements take 1 day for learning in average.
<i>Physical space:</i>	The room space required for measuring.	/
<i>Equipment costs:</i>	The costs of hardware devices/facilities needed in total to apply this method.	/
<i>Preparation time:</i>	The average time for preparing experiment in advance. Related to the costs of experts preparing all devices for measuring the workload.	/

3.3.2 While measuring

Table 3-2 Definition of each Criteria: While measuring

Metric	Description	Scenario
Operating difficulty:	The extent of workload and skills needed from researchers so as to properly apply this method.	/
Test time:	The average time for running the measuring experiment. Related to the costs of retaining expert and assistant and subjects in total.	/
Test-retest:	The correlation between two sets of scores obtained by the same tester on the two administrations of the method with the same worker.	Tester B uses force measuring method to measure the same workers twice, in order to check if the results are the same or not between two times.
Inter-rater:	The consistency of a method across different people.	Tester A and Test B use force measuring method separately to measure the same workers, in order to check if the results are the same or not between two times.
Manual error:	The extent to deviation caused by human mistake or operating error.	Tester A mistakes left hand for right hand in side view, and tester B installs the force sensor in an opposite direction.
Psychological Collaboration:	The extent of worker collaboration while measuring the workload.	Workers are easy to get impatient because they think the task of force measuring instrument is tedious because it always asks for doing boring and repetitive things.
Physical Collaboration:	The extent to which a measurement interferes while workers are being measured during working activities.	This force measuring method requires workers to press the sensor in advance for calibration every time, while other method without extra task. It hinders them for daily working and lead to distraction sometimes.

3.3.3 After measuring

Table 3-3 Definition of each Criteria: After measuring

Metric	Description	Scenario
Result communication:	The extent to which the results are understandable.	This force measuring method is able to show the force distribution in a coloured hand shape image also, which indicates high pressure in yellow, neutral pressure in green, and low pressure in blue. While other methods only show value or percentage.
Correlation:	The extent to the agreement and correlation of method results compared to other methods.	Tester A uses other two types of measuring methods with this force measuring instrument to measure the same workers third times, in order to check if the result is similar or not compare to other methods.
Career threat:	The possibility of which a measurement gives subjects the diagnostic medical information that may threatening their career during evaluating.	Workers might worry or blind to think if they got any disorder or potential risk on their hand since they find out some high values of a certain metric from force measuring results, which possibly causes dissatisfaction or strike.

3.4 Expert interview

Can you tell us the challenges you think are important when running an ergonomic experiment? Why?

Can you indicate us what you miss from the current ergonomic methods? What would be your wish list for a new and innovative ergonomic method?

What is your favorite ergonomic method for measuring upper limb? Why?

Which features you think are the most important for a wearable measuring device?

Is there any other feature for an ergonomic method or a wearable measuring device that we did not considered here and you think it could be critical?

Figure 3-11 Open question sheet.

Subsequently, this questionnaire is distributed among three experts. One of the experts is a professional who works for a company that is involved in ergonomics in the product design cycle. She is also a lecturer in ergonomics. The second expert is a PhD in mechanical engineering who did this PhD in the motion capture field and now works in a research centre with these systems. The third expert worked for a research centre with motion capture systems and now is lecturer on motion capture systems at an engineering university. All of them are asked to fill out only those questionnaires that they considered themselves experts on. Results are listed in the Table 3-4. Additionally, the experts are interviewed to answer five open questions (Figure 3-11) after they complete the sheets.

3.5 Results from experts

Results from ART Tools and RULA/REBA, show that observation methods almost comprehensively cover all the metrics with good validity, accessibility, practicability and cost-effective (Avg. = 3.7), except “Movement velocity”, “Vibration” and “Sudden impact” (Avg. = 1.3). Direct measurement systems (OES, EG, ACC and IMU) are the most objective methods to measure (Avg. = 4.4 on “Numbers”). The kinetic validity (Avg. = 3.6 on “Movement repetition”, “Body angles”, “Velocity of movements”, “Vibration” and “Sudden impacts”) and the reliability (Avg. = 4.1 on “Test-retest” and “Inter-rater”) are also important features of the four methods. Regarding to the order of “Operating difficulty” among direct measurements, EG is the easiest to handle (4.5), then IMU is the next (3.5), whereas OES and ACC are the hardest two (2 and 2.3). Additionally, IMU and EG approximately have the same level on “Manual error” with the other methods. From the interviews with the experts, it is said that although the precision of the captured repetitive movement depends on the capability of different products, the market trends still reveal that nowadays ergonomic experts tend to choose this type of methods to assist or replace expert observation. However, they evaluate these measuring data (angles, movements) later based on biomechanical or ergonomic database meaning that objectivity would slightly reduce somehow. Then, commercial measurement products are generally with less learning difficulty and more user-friendly, although prices are higher

as well. Thus, based on the overall feedback of the questionnaires and the interviews, we discussed and summarized that the four of the most requested critical feature demands of WMSDs exposure assessment in automotive assembly line are: portability, compactness, precision and the ability to let the user move naturally.

Table 3-4 Scale results of main WMSDs assessment methods. Assessment of Repetitive Tasks (ART) Tools, Rapid Upper Limb Assessment / Rapid Entire Body Assessment (RULA/REBA), Biomechanical Assessment (BA), Optoelectronic Systems (OES), Electro Goniometer (EG), Accelerometry (ACC) and Inertial Measurement Units (IMU).

Assessing Metrics	ART Tools	RULA/REBA	BA	OES	EG	ACC	IMU
Movement repetition	5	5	5	4.5	4.5	4	2.5
Body loads	4	5	5	1	3	1	1
Body angles	4	4	5	4	4	2.3	4
Velocity of movements	2	1	4	4	4	4	3.5
Duration of movements	4	4	3	4.5	4.5	3.3	2
Vibration	1	1	3	3	2.5	4.3	3.5
Sudden impacts	1	2	1	1.5	2	5	4
Muscles activity	3	3	5	2	3	2.3	2
Lifting	5	5	5	2.5	3	1.3	2.5
Independence	5	5	1	4	3	1	3
Numbers	4	4	5	4.5	4	4.7	4.5
Learning difficulty	5	4	1	1.5	3	2.7	3.5
Physical space	5	5	5	1	4.5	4.7	4.5
Equipment costs	5	5	2	1	3.5	3.7	4.5
Preparation time	4	4	1	1.5	3	3.3	3
Operating difficulty	5	5	1	2	4.5	2.3	3.5
Test time	4	4	3	4	4	3.5	4
Test-reTest	4	4	5	5	3.5	3.7	4
Inter-rater	4	4	5	4.5	3.5	4.3	4
Manual error	3	3	3	4	3	3.7	3
Psychological collaboration	5	5	4	1.5	4	3.7	2.5
Physical collaboration	5	5	4	3	4.5	4.7	4
Safety	5	5	5	5	4	5	5
Result communication	5	5	5	5	4	4.3	5
Correlation	4	4	3	5	3.5	3.3	4
Career threat	2	2	4	5	4	4	5

3.6 Conclusions

According to the findings of the questionnaire assessment, it must be pointed out that the evaluations are relative within their individual knowledge. For example, in terms of the expert observation methods, the metrics of numbers, Test-reTest, Inter-rater, as well as most of the validity factors have incomprehensible high values. This is because subjects are divided into the expert observation group and the direct measurement group, and they answered without getting a bare idea about the capabilities of the other methods from the other groups. The actual relationship between these two groups has been understood from the interview with experts who have the experience across technologies or methods from both groups. Furthermore, measurement validity, learning difficulty, price and preparation time, those metrics may depend on different tasks, and different features from immensely wide product choices in the current market. Similarly, in the OES for instance, the effective coverage and resolution involve the quantity of camera used, which is related to the demands on real site. Additionally, from the current studies and interviews, the fact is that more and more experts and researchers apply assessment table and direct measurements together, merging the advantages of evaluating convenience and measuring accuracy from multiple types of methods. We have tried to generalize each metrics as much as possible for a more objective conclusion.

With respect to the selection of the technology, combined with the actual demands of automotive assembly plant workplace, it is believed that IMU is the most advisable technique among the present measurements. On the one hand, self-report and expert observation do not meet the requirement of positive observing, objective and accurate results, productivity guarantee, even real time monitoring. As such, selection is focused on direct measurements. On the other hand, noticing that nearly all the facilities in the assembly line are made of metal, OES systems can suffer from “ghost marker” to obstruct the recognition of the camera. Moreover, poor illumination, occlusion, expertise requirement, large operating space, high costs on money and time determine that OES are hardly used on real work site. Likewise, the EG has the problem of size and weight, which will hamper the

worker's activities, especially in the intensive and complex assembly environment. Regarding to ACC, experts claimed that there is not any single ACC measurement currently in the market, because of its critical drift error and poor independence. Additionally, productivity and cost-effectiveness are commonly undervalued in existing ergonomic studies [48]. Throughout the analysis of the State of the Art about direct measurement devices, the IMU system has become increasingly acceptable, and so has the potential for physical exposure detection of precise movements in the hand region. Meanwhile, the IMU have the advantage of being applicable to both indoor and outdoor settings [48]. Though the system takes advantage of the low cost and small size of inertial sensors, it can be affected to render erroneous data from surrounding metal infrastructures or buildings [125]. Summing everything up, it can be said that there is not a perfect measurement system, but currently IMU is the most suitable.

Chapter 4:

Developing finger motion capture device

4.1 Introduction

In this chapter, a functional IMU-based motion capturing prototype is implemented. Section 4.2 briefly introduced the specification of components and their circuit wiring. Section 4.5 explained the system framework, and data format selection based on mathematical theories. Moreover, the programming works are presented in detail. Section 4.6 demonstrated an accuracy experiment to verify the feasibility of the prototype.

Due to the nature of body displacement in the lower limb movements, all remaining body movements are rotations of varying ROM. From another point of view, overuse, high frequency repetition, excessive range and angular velocity are based on rotation movements. All manual fatigue exposure factors except bio-mechanical metrics such as compression or impulsive force, which are not included in our review, are also dependent on rotational movements. Therefore, only

rotational movements are involved in this study, rather than displacement movements.

For the early prototype, only two fingers are tracked. Since mostly human daily hand actions, such as picking and gripping, are done by the thumb and the index finger, those two of the most essential fingers are adopted. Additionally, the length of each phalanx of a volunteer is physically measured in advance. Namely, first metacarpal (6.5 cm), proximal phalanx (4 cm), distal phalanx (3cm) of the thumb, and second metacarpal (8.5 cm), proximal phalanx (5 cm), Intermediate phalanx (3 cm), distal phalanx (2.5 cm) of the index finger, of which seven IMU sensors in total are required. Figure 4-1 shows a division on the (right) human hand.

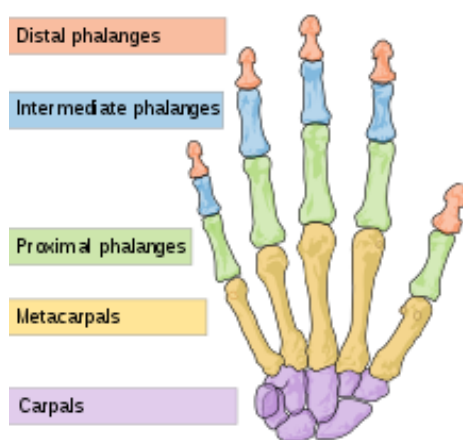


Figure 4-1 Human hand bones.

4.2 Hardware

Several components are implemented to build the prototype (Figure 4-2). These include:

- 1 x Arduino microcontroller
- 7 x IMUs
- 1 x Multiplexer
- 1 x MicroSD card module (plus and SD card)

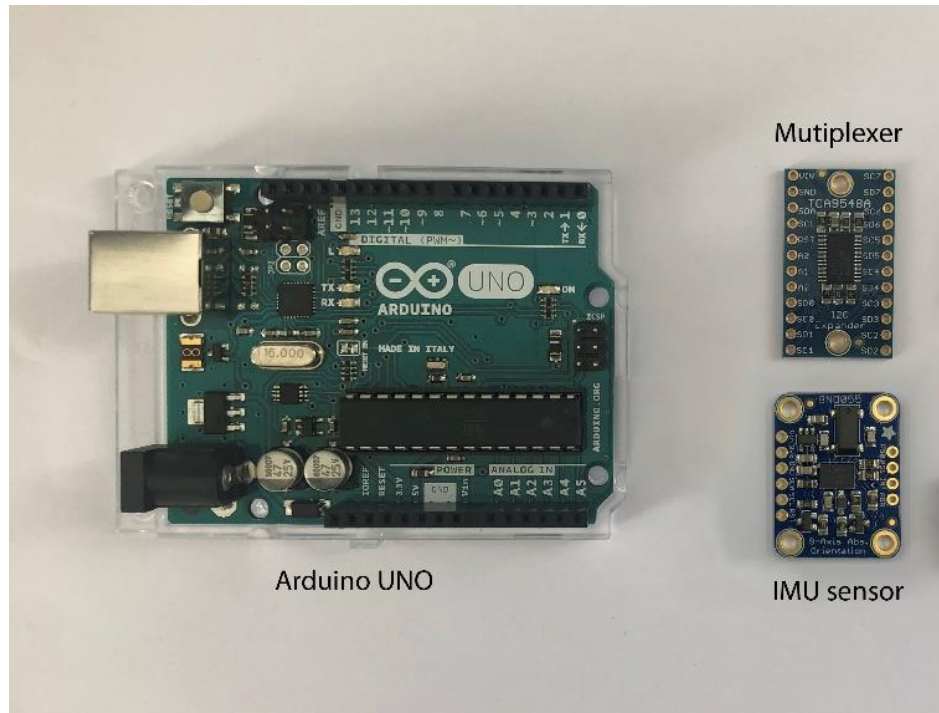


Figure 4-2 Components of prototype.

4.2.1 Microcontroller

There are many open source hardware devices on the market that can be used as microcontrollers, such as Arduino, Raspberry Pi, STM32 Development Boards, etc. In terms of hardware performance, different brands have various performance gradients to meet user needs, which is not enough to be a reason to choose a microcontroller. In the microcontroller market in recent years, Arduino has become one of the most successful open source hardware developers. The important reasons are:

1. Open source: Arduino has a high degree of freedom, and its concept of sharing and collaboration is also more secure and flexible than professional products.
2. Supporting community: the huge number of projects and teams has created an amazing ecosystem of accessories and libraries. Developers are able to focus more on creative work. This is

unmatched by traditional products, which is also one of the reasons why Arduino is superior to other open-source hardware.

3. **Commercial channels:** because of its excellent product quality and market penetration rate, Arduino has become a representative platform, rich module production, and third-party developers, resulting in low consumption costs and diverse choices.
4. **Low learning costs:** mature product manuals and community services. Compared to other open-source hardware, Arduino makes it easy for many beginners to find resources and learn.

In this study, Arduino UNO is utilized first. The specifications are showed in Table 4-1. The pin description is showed in Table 4-2.

Table 4-1 Specification of Arduino UNO.

Specification	Detail
Microcontroller	ATmega328P – 8 bit AVR family microcontroller
Operating Voltage	5V
Recommended Input Voltage	7-12V
Input Voltage Limits	6-20V
Analog Input Pins	6 (A0 – A5)
Digital I/O Pins	14 (Out of which 6 provide PWM output)
DC Current on I/O Pins	40 mA
DC Current on 3.3V Pin	50 mA
Flash Memory	32 KB (0.5 KB is used for Bootloader)
SRAM	2 KB
EEPROM	1 KB
Frequency (Clock Speed)	16 MHz

Table 4-2 Pin description of Arduino UNO.

Pin Category	Pin Name	Details
Power	V _{in} , 3.3V, 5V, GND	V _{in} : Input voltage to Arduino when using an external power source. 5V: Regulated power supply used to power microcontroller and other components on the board. 3.3V: 3.3V supply generated by on-board voltage regulator. Maximum current draw is 50mA. GND: ground pins.
Reset	Reset	Resets the microcontroller.
Analog Pins	A0 – A5	Used to provide analog input in the range of 0-5V
Input/Output Pins	Digital Pins 0 - 13	Can be used as input or output pins.
Serial	0(Rx), 1(Tx)	Used to receive and transmit TTL serial data.
External Interrupts	2, 3	To trigger an interrupt.
PWM	3, 5, 6, 9, 11	Provides 8-bit PWM output.
SPI	10 (SS), 11 (MOSI), 12 (MISO) and 13 (SCK)	Used for SPI communication.
Inbuilt LED	13	To turn on the inbuilt LED.
TWI	A4 (SDA), A5 (SCL)	Used for TWI communication.
AREF	AREF	To provide reference voltage for input voltage.

4.2.2 Inertial Measurement Unit

According to the experts' responses on Chapter 3, a MEMS-based motion capturing sensor (IMU) is the one selected for the prototype. In particular, the Bosch BNO055 absolute orientation sensor, a 9 degrees of freedom (DoF) IMU with a thumbnail scale (Figure 4-4), is selected. It integrates a 14-bit triaxial accelerometer, a 16-bit triaxial gyroscope,

a full performance magnetometer and a 32-bit ARM Cortex-M0 based microcontroller, communicating via Inter-Integrated Circuit (I2C) bus line with other components.

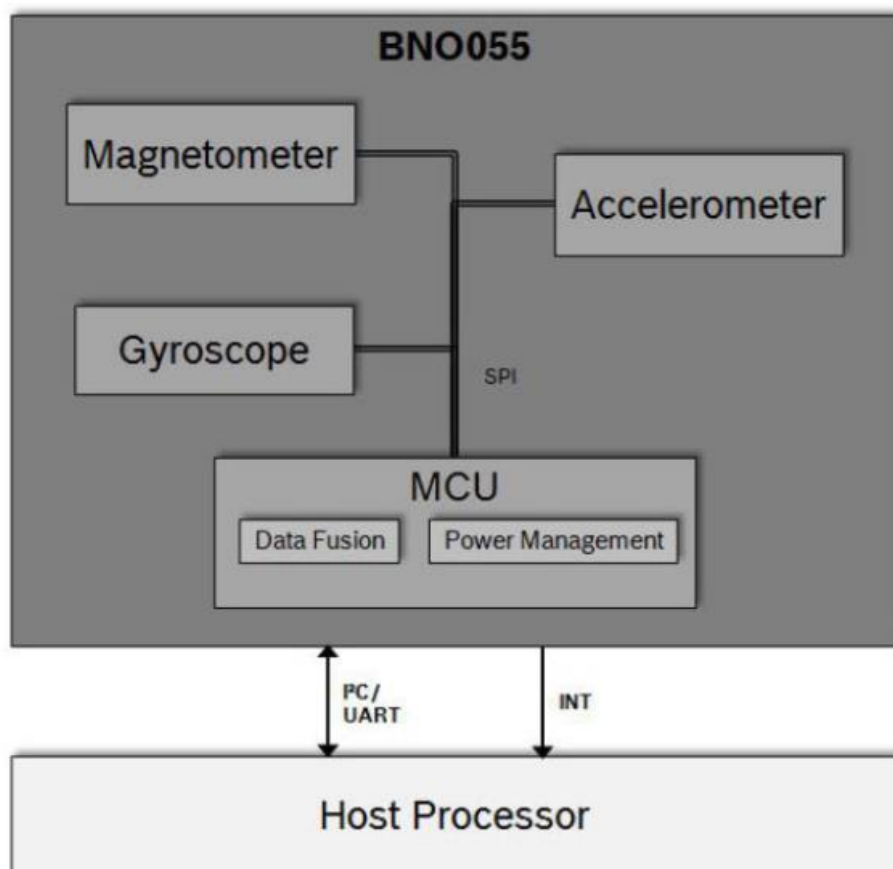


Figure 4-3 Architecture of BNO055 [126].

Figure 4-3 shows a basic building block of the BNO055 device. In addition, this IMU sensor includes a complete calibration algorithm. It is necessary to take approximately one minute to do some

calibration movements that are introduced by the Bosch standard calibrating method (later introduced in Section 4.6).

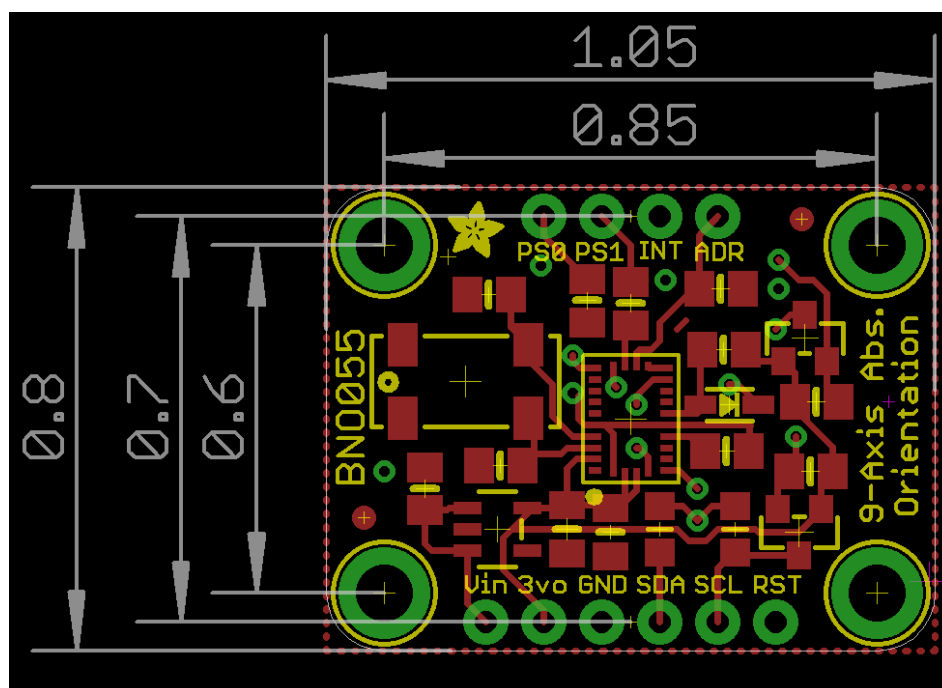


Figure 4-4 Main dimensions of IMU (in inch) [127].

4.2.3 Multiplexer

A 1-to-8 I2C multiplexer (as shown in Figure 4-2), or called expander (TCA9548A, Adafruit) which acts as a gatekeeper, is used to extend up to 8 same-address IMU sensors and hook up to a central controller (Arduino UNO, Arduino.cc), transmitting the commands to the selected set of I2C pins.

4.2.4 SD module

Data storage can be addressed by direct serial port monitoring on Arduino integrated development environment (IDE) during real-time capturing, or using a Micro-SD card module. For the latter work, a microSD adapter (MicroSD card breakout board+, Adafruit, United States) is utilized to store the data after recording and processing. It uses a proper level shifting chip without extra resistors and can read

and write 2Gb+ of storage. To use this module correctly, an Arduino IDE's SD library which supports File Allocation Table (FAT) and FAT32 SD card is needed.

4.3 Electrical connection layout

When only two IMUs are necessary, the connections are pretty simple. The two I2C data lines are merged on the same I2C bus to pin A4 and A5 of Arduino. To activate this mode, a jump wire from VIN of the second IMU connect to address pin (ADR) is needed. This will change the default I2C address from 0x28 to 0x29 if this sensor is connected to 3V. The wire connection is shown on Figure 4-5.

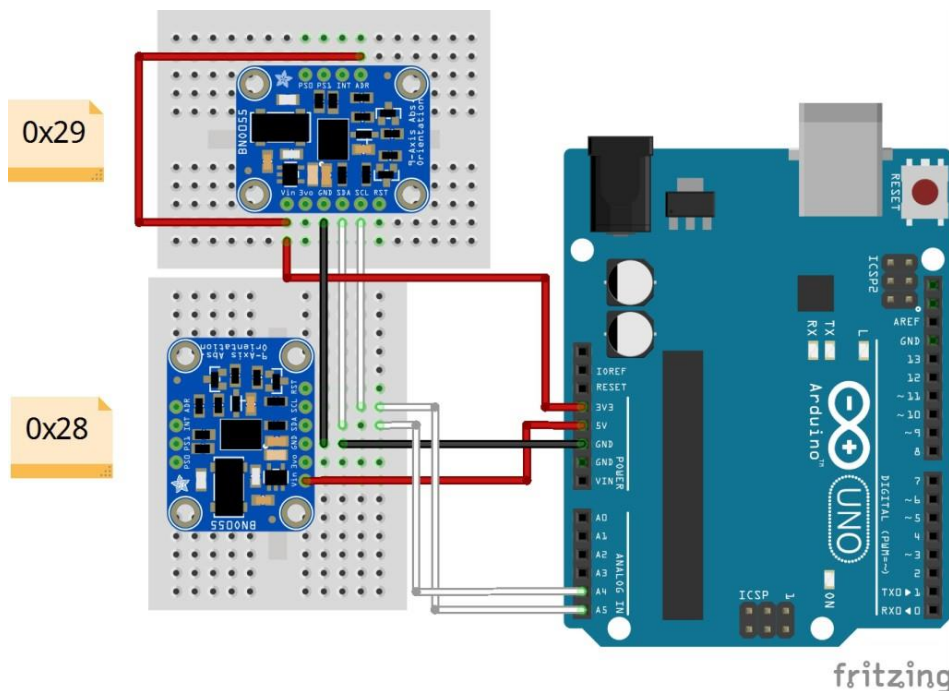


Figure 4-5 Circuit wiring for two IMUs.

However, due to the limits of power supply and number of I2C ports from Arduino UNO, a tree structure circuit connection is applied to connect the 7 IMUs, which is also corresponding to the anatomy of human hand. Power lines start from Arduino to pin VIN and GND of multiplexer in serial, then distributed in seven sub-line in parallel. I2C lines start from pin A4 (SDA line) and A5 (SCL line) of Arduino

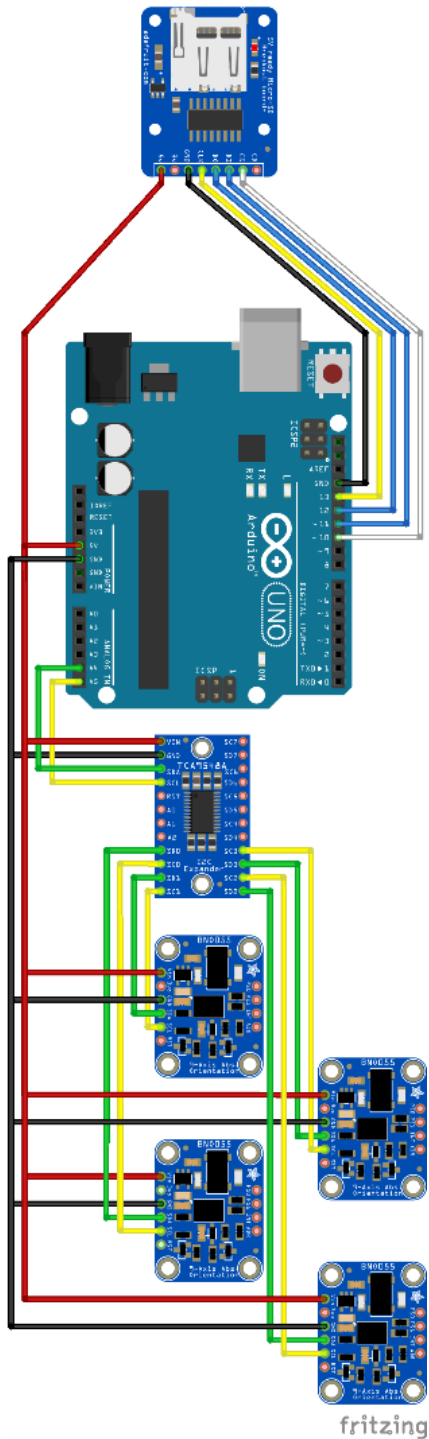


Figure 4-6 A division of prototype's circuit wiring.



Figure 4-7 Thumb & Index finger gesture capturing.

and connect to Serial Data (SDA) pin and Serial Clock (SCL) pin of multiplexer. On this board, 8 pair of I2C ports from 0 to 7 are arranged on two sides. Each pair of ports connect to pin SDA and SCL of each IMU sensor.

Moreover, in the occasion of data storage via Micro-SD card, pin 13, 12, ~11, ~10 of Arduino are connected to pin CLK, DO, DI, CS of Micro-SD card module correspondingly. Figure 4-6 shows the connection layout of four IMUs of seven. To add the rest of the IMUs, the process is straightforward.

4.4 Assembling prototype

In an early attempt based on two IMUs sensors, a container with Velcro tape is made to bind the IMU to the surface of the upper and lower arms. However, the container is not suitable for fingers due to its excessive volume. Therefore, the use of rubber bands is the most convenient and simple method to temporarily fix the IMU.

Each IMU is attached to a dorsal surface of the thumb and index finger phalanges with the help of rubber bands. Figure 4-7 shows several representative gestures that are successfully captured and visualized by this prototype.

4.5 Software

4.5.1 System framework

The tracking process of the fingers began with the IMU sensors collecting orientation data in the form of unit quaternion vector. Then, data pass through the multiplexer via I2C bus lines to Arduino UNO. Next, those data are packaged at Arduino and sent to MATLAB for visualization. In MATLAB, several processes are executed to calculate the coordinates of each finger joint in the local and global reference system. The whole progress is shown in Figure 4-8.

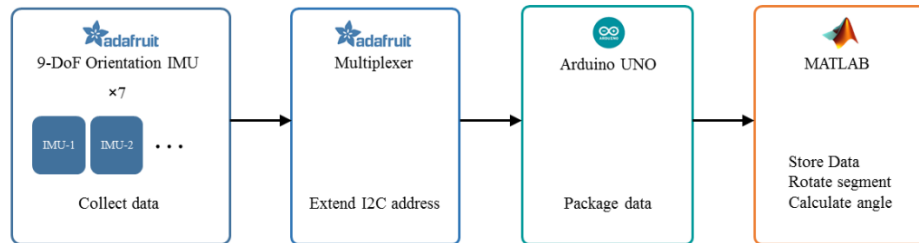


Figure 4-8 Data process in the system.

4.5.2 Orientation format

The orientation of a rigid body can be described with a vector in 3-dimensional Euclidean space, hence the change of orientation is depicted with a rotation around a fixed axis. There are four equivalent ways to describe such a rotation, which exploit the concept of Euler angle, Rotation matrix (or Direction Cosine Matrix), axis-angle, and Quaternion, respectively. In this section, each method is introduced and then evaluated. The pose of IMU sensor is also introduced at the end.

Euler angle

The three-elemental rotation of a rigid body can be global or local, which means, the axes xyz of the original coordinate system remains motionless in the global system, or changes xyz orientation after each elemental rotation in the local system. In computer vision, local rotation is more often used. Euler angle is a group of angles that a rigid body used to rotate around a fixed coordinate system based on its volume centre. Moreover, rotation sequence changes the final orientation of rigid body. Namely, if the object needs to rotate to the same orientation by different sequences, the values of the Euler angles are disparate. Therefore, any discussion employing Euler angles should define its rotation sequence. Most of the studies employ Tait–Bryan angles, which are known as yaw, pitch and roll. In Figure 4-9, following the sequence z - y - x , a rotation is decomposed by three steps in which the first rotation is an angle ψ about z -axis (yaw), the second rotation is an angle θ about N -axis (pitch), and the third rotation is an angle φ about X -axis (roll). For notational brevity, the rotation is defined as $E(\psi, \theta, \varphi)$.

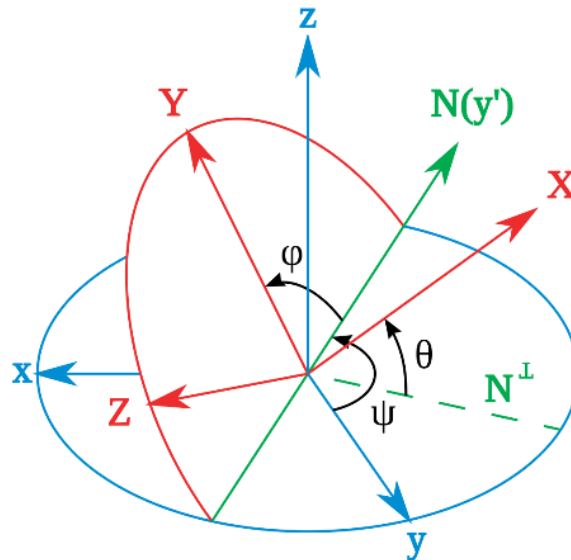


Figure 4-9 Euler Angle Sequence z-y'-x".

Although Euler angle system is intuitive, several drawbacks are critical to use it in kinematic study. Firstly, the expression is not unique, which is a singularity of Euler angle, called “Gimbal lock”. It arises from the indistinguishability of changes in the first and third Euler angles when the second Euler angle is at some critical value [128]. For instance, following the same sequence (ψ, θ, φ) , $E_1(0, 90, 0)$ will rotate to the same orientation as $E_2(90, 90, 90)$. Secondly, Euler angle is very ill-behaved for interpolation and should be converted to other forms for interpolation purposes [129]. Thirdly, the amount of calculation is huge, due to an extra transformation from Euler angle to rotation matrix at run time is needed.

Rotation matrix

A more popular form to calculate coordinate transformations, is using rotation matrix. This can be described as a matrix defined by

$$R(\alpha, \beta, \gamma) = R_z(\alpha)R_y(\beta)R_x(\gamma)$$

$$= \begin{bmatrix} \cos \alpha & -\sin \alpha & 0 \\ \sin \alpha & \cos \alpha & 0 \\ 0 & 0 & 1 \end{bmatrix} \begin{bmatrix} \cos \beta & 0 & \sin \beta \\ 0 & 1 & 0 \\ -\sin \beta & 0 & \cos \beta \end{bmatrix} \begin{bmatrix} 1 & 0 & 0 \\ 0 & \cos \gamma & -\sin \gamma \\ 0 & \sin \gamma & \cos \gamma \end{bmatrix},$$

If the sequence of yaw, pitch and roll changes, the matrix has to be multiplied in the same sequence, which will affect to the results. Moreover, a rotation matrix must be an orthogonal matrix due to a limitation of 3-DoF although containing 9 elements. For composing rotations, that is to multiply two matrices, a total of 27 multiplications and 18 additions are required [130], which causes three-time redundant calculations. In some real applications, rounding errors are accumulated inevitably when composing several rotations. Nonetheless, the computational error after composing rotation matrices, will make it not be orthogonal anymore and is harder to convert back to a proper orthogonal matrix [130].

Quaternion

Quaternion is a type of higher-order complex number, which can be represented as:

$$Q = (x, y, z, w) = xi + yj + zk + w, \quad [1]$$

where \mathbf{i} , \mathbf{j} , \mathbf{k} can be viewed as the unit vector along the x , y , and z axis, respectively. The multiplication rule follows.

$$i^2 = j^2 = k^2 = -1, \quad [2]$$

$$ij = k, jk = i, ki = j. \quad [3]$$

In this context, quaternion is composed of a vector part, $\vec{v} = xi + yj + zk$, and a scalar part, w :

$$Q = (\vec{v} + w) = ((x, y, z), w). \quad [4]$$

Due to its four dimensions, quaternion is flexible to transform into a universal form of the other representations. Thus, any vector can be treated as a quaternion of which the scalar part is zero (called pure quaternion), $p = [\vec{v}, 0]$. In this circumstance, quaternion can be exploited for expressing a rotation operation in 3-dimensional space. Different from the case of Euler angles, the spatial rotation can be performed on an arbitrary axis, which is called Axis-angle representation. If the axis direction is represented by a unit vector $\mathbf{u}(x, y, z)$ and the rotation angle is σ , the rotation operation can be represented as a unit quaternion \mathbf{q} (shown in Figure 4-10).

$$q = ((x, y, z) \sin \frac{\sigma}{2}, \cos \frac{\sigma}{2}). \tag{5}$$

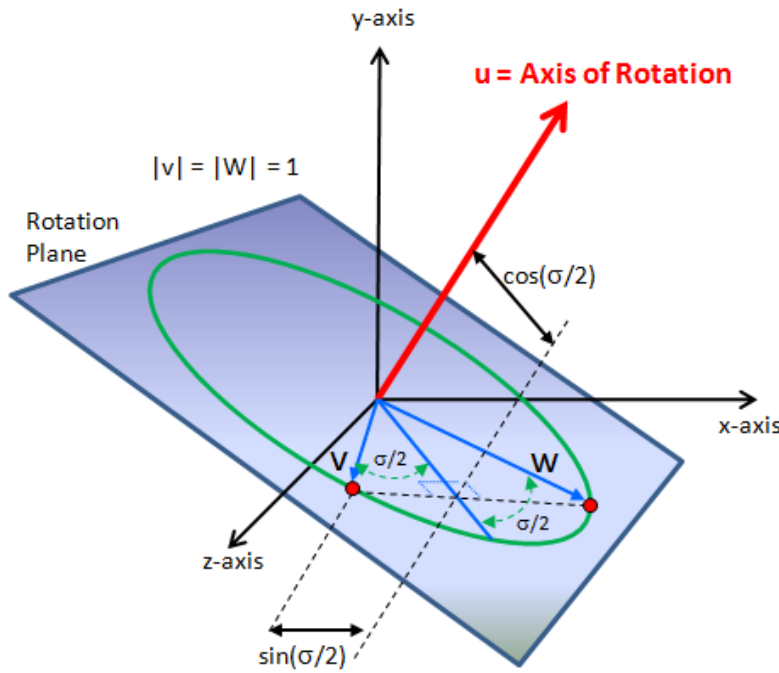


Figure 4-10 Quaternion for rotation.

Hence, a coordinate rotating transformation can be directly implemented by multiplying with spatial coordinates \mathbf{p} and rotation amount \mathbf{q} both in quaternion form. Yet, if we only multiply \mathbf{p} and \mathbf{q} , the quaternion obtained may fall into a four-dimension form when the scalar part is not zero, which means a point not in three-dimension reality. Thus, in order to transpose \mathbf{p} back to the original coordinate system, the inversed quaternion of \mathbf{q} is required. Fortunately, the feature of unit quaternion is that the conjugation of \mathbf{p} is equal to the reciprocal of quaternion, due to the norm of a unit quaternion is 1.

$$q^{-1} = \frac{q^*}{N(q)} = q^*. \tag{6}$$

Then, after the rotation around $\mathbf{u}(x, y, z)$ by an angle of σ point $\mathbf{p}((x_p, y_p, z_p), 0)$ transforms into point \mathbf{p}' ,

$$p' = qpq^{-1}. \tag{7}$$

This is the three-dimension rotation theorem in quaternion form and general case. It is noted that, this multiplication is not commutative, namely the order of multiplication should not be reversed. The order of multiply direction between \mathbf{p} and \mathbf{q} is equal to its reciprocal relationship. Moreover, the convention of the coordinate system with the right-handed rule is employed in this paper.

Quaternion-based rotation has an advantage of completely avoiding the gimbal lock issue because of its properties. Compared with the aforementioned rotation matrix method, quaternion-based one needs fewer parameters (4 numbers in a quaternion versus 9 numbers for an orthogonal matrix), thus less amount of calculations and more efficiency are expected (a quaternion product needs for a total of 16 multiplications and 12 additions [130]). Furthermore, it has a well-communication on axis-angle system, which is able to construct a rotation quaternion easily, and also easy to read off conversely from a quaternion. Regarded to composing rotations, a quaternion after multiplying will become non-unit length, but it is able to be fixed easily by normalization. Finally, for some later process, quaternion is adaptable to spherical linear interpolation (SLERP). The only disadvantage about quaternion, is literally difficult to understand and master it. For those reasons above, quaternions are selected instead of Euler angles and rotation matrix in this study.

Pose

After selecting the data format, due to the pose of IMU sensor applied to varied projects is different, the orientation of coordinate system mapping on the sensor chip is vital. Figure 4-11 shows a collection of IMU chip remapping orientations which are defined on the code library file `Adafruit_BNO055.cpp` (see Appendix A). A function called “`setAxisP()`” is customized into this library file (line 146-157). A black dot on a surface of each cuboid on Figure 4-11, corresponding to the light grey dot on real BNO055 chip is worked as the remapping reference (Figure 4-12). In this study, it is found that the default set is P1. By reason of the very narrow space of human finger, the IMU sensor is assigned upright along the phalanx. Hence,

after several actual tests with the plotting at Matlab, the coordinate system orientation in this study, is modified to pattern P6.

The default values correspond to the following coordinate system

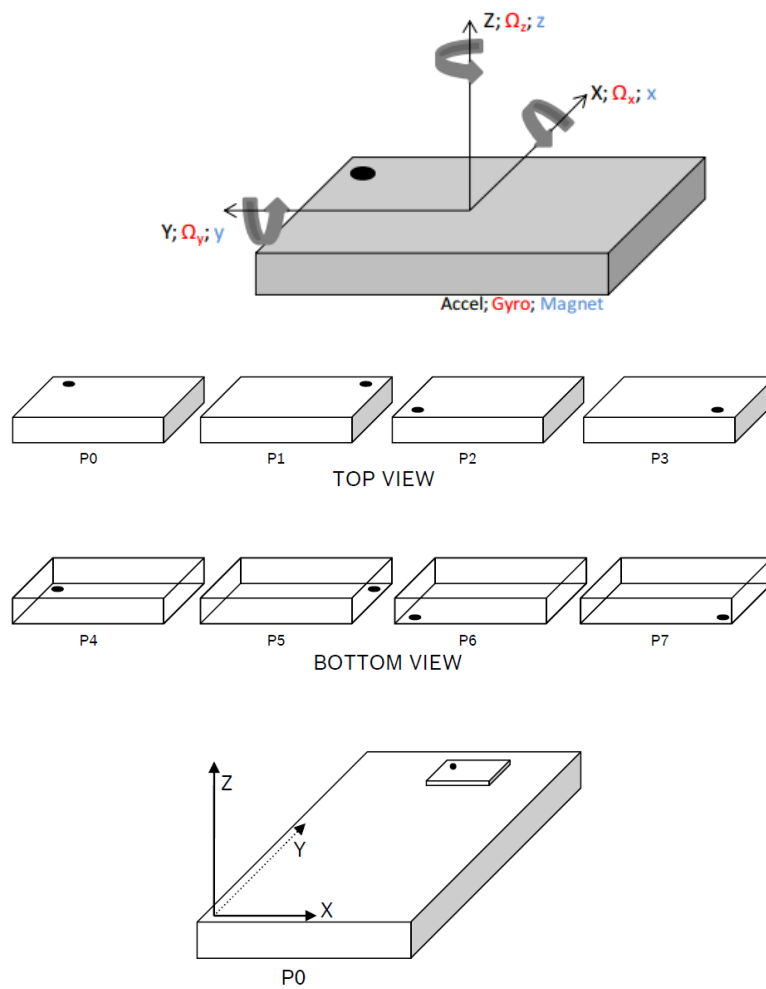


Figure 4-11 BNO055 chip remapping.



Figure 4-12 Orientation dot on BNO055.

4.5.3 Algorithm

Arduino IDE section

The programming starts with Arduino IDE (See Appendix B).

In coding part, firstly, several basic and sensor-related libraries are included (line 1-6), and necessary variables are defined in advance: devices address, indicators, array memory, etc (line 11-25).

Secondly, a function called “tcselect”, is declared for switching multiplexer port to respond each IMU when data is sampling (line 30-34).

Thirdly, in setup part, the setup is executed, including procedures: defining communication bit rate, activating each sensor, connection error self-detection, and coordinate axis remapping (line 39-76). Lastly, at the loop part, the quaternion data is received from each IMU using function “.getQuat()” by order (line 126), together with the current calibration status using function “.getCalibration()” (line 128) and time period using function “micros()” (line 184). Next, taking data from “bno[]” array, command “Serial.print();” is used to output the quaternion, calibration status, and time to the serial monitor to have the real-time data flow (line 132-151).

Due to the selected Arduino specifications, the performance and memory are not enough to complete a massive data acquisition and

processing synchronously. In order to avoid the response delay caused by excessive calculation, the data processing part is transferred to the subsequent professional processing software (which is Matlab). In addition, for some real work scenarios, SD storage is more practical than real-time monitoring. This study goes for a second choice to manage data: Micro-SD module. It is integrated and packaged together with the main program as a complete user-oriented application. In Arduino IDE, using function “.print()” (line 155-177), data are output to a text file which is generated to store IMU data when each time task is recorded. In line 43-53, the codes check the existing TXT files and execute initialization. In line 85-119, the codes define the file name following the number of the previous file name. If there is no file existed, it will start with “D0001.txt” every time, this will count up to D9999. User has to move out files from the SD card if the file counts arrived to maximum. Following this, user can easily import recorded files into internal data store cell in Matlab.

Herein, by using the function “Serial.print()” and “.print()”, all the data can output to any post-processing terminals or documents correspondingly. This code provides a simplified and compact data flow for later use, which is shown as an example of one rotation in Table 4-3.

Table 4-3 Data flow of one period.

Time	w	x	y	z	System	Gyro	Accel	Mag	ID
0.4066	0.4067	-0.2980	0.6866	0.5238	3	3	3	2	0
0.4066	0.2900	-0.2902	0.6476	0.6420	3	3	3	3	1
0.4066	0.9755	-0.2130	-0.0165	0.0536	3	3	3	2	2
0.4066	0.4778	0.1616	0.5480	0.6674	3	3	3	3	3
0.4066	0.5635	0.0486	0.3305	0.7556	3	3	3	2	4
0.4066	0.5229	-0.2891	-0.1661	0.7845	3	3	3	3	5
0.4066	0.4882	-0.2890	-0.3306	0.7543	3	3	3	3	6

The first column keeps in the same value, representing that the time consumption of this rotation, where seven sensors record quaternions nearly at the same time in this period. Columns from “w” to “z” are the main data flow. Status columns monitor hardware situations including system, gyroscope, accelerator and magnetometer

by scoring between ‘0’ (uncalibrated data) and ‘3’ (fully calibrated) [127]. The whole code has introduced in the Appendix B.

Matlab section

Figure 4-13 shows an overview of the steps programmed in Matlab and shown in Appendix C.

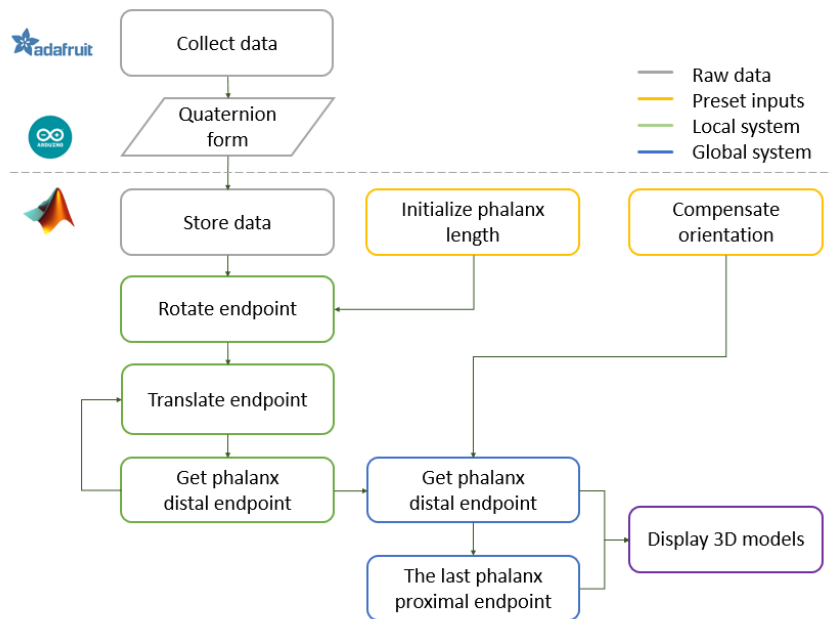


Figure 4-13 Flow chart of data process.

Once the code has been uploaded to Arduino board and correctly connect to PC, using two commands “serial()” and “fopen()”, data flow is able to be imported into Matlab for real-time motion capturing (line 29-33). The serial port must keep the same one as in Arduino. Coordinate origin, phalanx length and data storage cell, etc are pre-defined (line 65-78).

In order to have the same perspectives between operator’s view and plotting camera on the screen, a concept called “compensation angle” is introduced. A digital compass is used to measure the angle value from magnetic north to the direction orthogonal to the terminal screen, representing an offset left-handed rotation angle around the

upward Z axis. Figure 4-14 demonstrates the result difference between uncompensated and compensated virtual gestures.

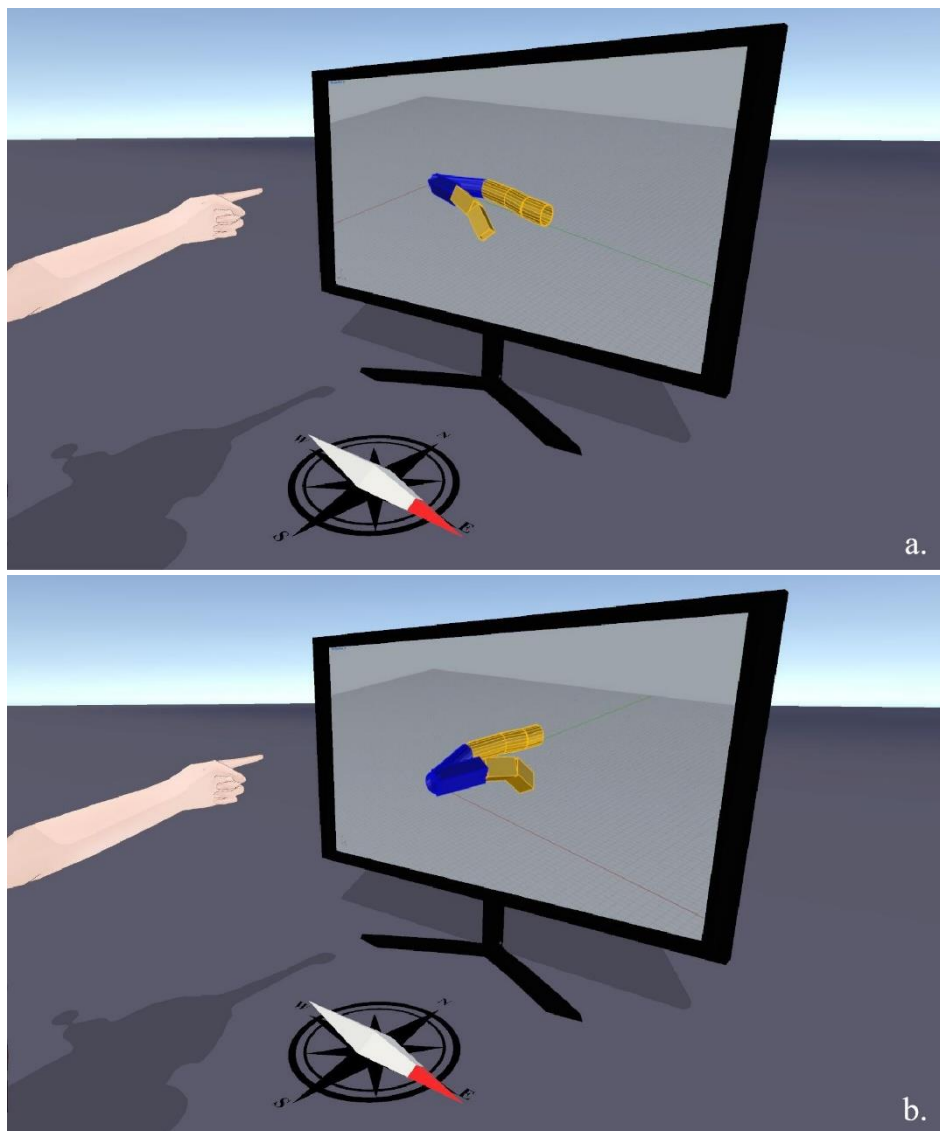


Figure 4-14 Remapping gesture: a) before applying the compensation angle, the virtual fingers are aiming to the magnetic north in the real world. b) after applying the compensation angle, the virtual fingers are aiming to the north of the virtual world. The orientation of the digital compass corresponds to the virtual world. Namely, the direction of the letter 'N' refers to the virtual north, and the physical index fingers are aiming to the west in reality.

Next, by input this value, it is transformed to a global compensation unit quaternion for later calculation. This angle value varies, due to each workplace heads to different orientations in reality. The whole code has introduced in the Appendix C. The main processes are executed as following steps:

1. As mentioned above, there are two ways to receive data. To read data from the TXT file, a function called “fgetl()” is used (line 105). To obtain data from the serial port, function “fscanf()” is used (line 108). In the real task, these two functions are mutually exclusive, otherwise, a conflict on variable “str” will occurred.
2. Raw data are transferred from string to double float format and stored in a zero matrix (line 110-115). The data flow is displayed on command window at the same time in Matlab (line 117-124).
3. Define seven points on the local rigid body coordinate system in quaternion form (w value equals to zero) along positive direction of Y axis in a corresponding real phalanx length (line 74 and line 10-11 in Appendix D).
4. As mentioned before in 4.5.2, the conjugation of the quaternion is equal to its reciprocal here because of the unit quaternion. Hence, rotate each local points with sensor quaternions from the data storage (representing the rotation movements) via the quaternion rotation formula sequentially to attain the triple cross product, where each local point is multiplied first by its reciprocal quaternion then by the sensor quaternion (line 10-11 in Appendix D), which, due to the cross product is not commutative. Thus the local rotated points are obtained correctly. Apart from the CMC joints of each finger, which are located on the original point, the rest of the joints are translationally connected to the previous endpoint of its phalanx (line 13-14 in Appendix D).
5. Given a compensation quaternion, multiply joints via the same quaternion rotation formula mentioned above. Hereto the local rotated joints are converted to the global coordinate system (line 17-18 in Appendix D). Step 2, 3, 4 are integrated into a customized function “DistalQuatMultiTransform()”.

6. Calculate the finger angles between every two normalised segment vectors by the arccosine of the dot product. Specific steps are also integrated into a customized function “VectorAngle()” (see in Appendix E).
7. Use a two-point type 3D cylinder function to model and plot each virtual segment by connecting each proximal joint with the previous distal joint. Specific steps are integrated into a customized function “cylinder2P()” (see in Appendix F).

Table 4-4 An example of output of calculated finger angles (in degree).

Time (s)	MCP T2I	TMCP	TIP	IMCP	IPIP	IDIP
00:00.4	26.37	16.83	131.59	9.04	62.71	17.11
00:00.9	26.41	17.49	133.05	8.85	62.69	17.12
00:01.3	24.68	15.27	129.95	10.09	62.33	17.4
00:01.8	24.38	14.22	117.91	15.52	62.41	17.11
00:02.2	23.99	17.61	108.16	16.04	62.43	17.01
00:02.7	24.01	16.85	104.44	15.96	62.33	16.88
00:03.1	23.47	16.27	102.71	15.47	62.47	16.78
00:03.5	23.47	15.79	102.72	15.3	62.26	16.85
00:03.9	23.6	13.01	104.7	15.27	62.3	16.96
00:04.3	23.54	11.89	105.96	15.22	62.22	16.9
00:04.7	23.26	10.52	106.81	15.17	62.3	16.83
00:05.1	23.08	5.35	110.73	14.4	62.82	18.5
00:05.5	22.24	8.06	112.45	29.41	76.96	17.71
00:05.9	23.66	5.69	112.39	29.47	74.57	17.16
00:06.4	27.97	4.33	103.92	28.77	76.65	18.74
00:06.8	34.19	19.96	106.46	27.78	76.16	16.61
00:07.2	34.64	19.38	101.38	30.69	70.13	17.08
00:07.6	29	12.27	97.66	15.07	38	11.73

Performing the data calculation process as mentioned before in Matlab section, two type of output files are obtained: coordinate output file and angle output file. Thanks to the formatting operator, data are loaded and saved in a table format orderly by conversion character and horizontal tab. Thus both of the two outputs are convenient to be imported into any statistical software such as Excel or Minitab (shows

in Table 4-4 and Figure 4-15), and adaptable for later 3D restoring simulation or biomechanical analysing. All of those procedures have been converted into an executable file by Matlab compiler for independent use. Moreover, the 3D model plotting function which used before is also added for a quick check of finger movement records in this application.

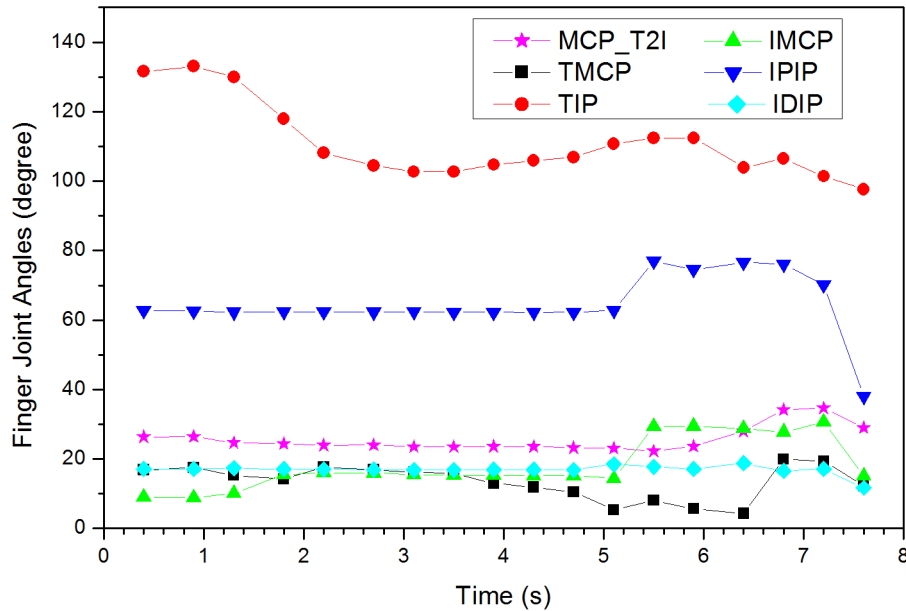


Figure 4-15 Example of data output on finger joint movements.

4.6 Accuracy verification

To verify the feasibility of this prototype, a laboratory goniometry experiment is designed and conducted. Although, the sensors are factory trimmed to reasonably tight offsets, meaning valid data are must be obtained even before the calibration process is complete [127], The calibration process is introduced as following criteria [127]:

- **Gyroscope:** the device must be standing still in any position.
- **Magnetometer:** in the past, 'figure 8' motions were required in 3 dimensions, but with recent devices fast magnetic compensation takes place with sufficient normal movement of the device.

- Accelerometer:** the BNO055 must be placed in 6 standing positions for +X, -X, +Y, -Y, +Z and -Z. This is the most onerous sensor to calibrate, but the best solution to generate the calibration data is to find a block of wood or similar object, and place the sensor on each of the 6 'faces' of the block, which will help to maintain sensor alignment during the calibration process. You should still be able to get reasonable quality data from the BNO055, however, even if the accelerometer isn't entirely or perfectly calibrated.

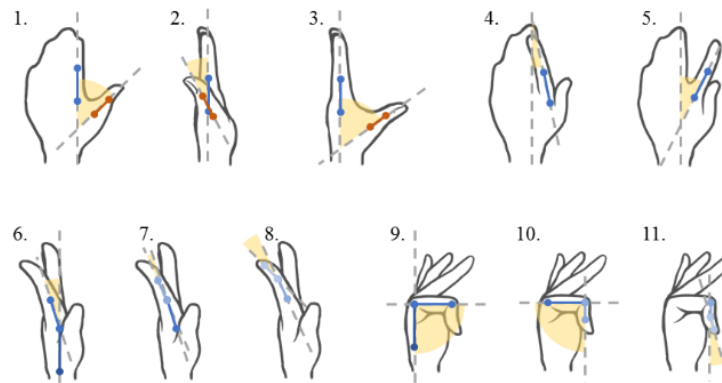


Figure 4-16 Measuring gestures of each angle.

After calibrating IMU sensors, three participants are asked to physically measure those knuckle angles while a fourth volunteer wore the IMU and performed some designed gestures with his hand (Figure 4-17). Simultaneously, the virtual angles are calculated and displayed in MATLAB. Eleven virtual and physical angles are measured and compared in real time.

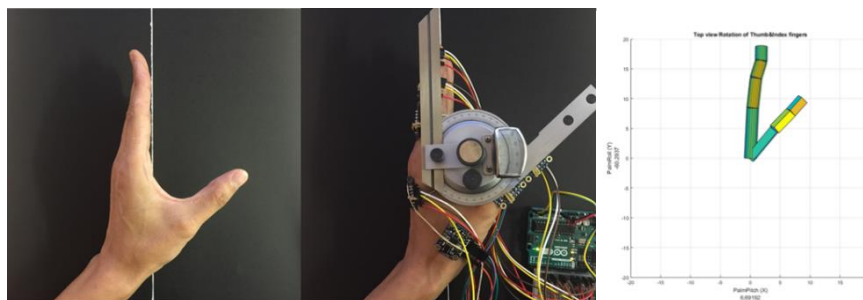


Figure 4-17 Thumb abduction angle measuring by goniometer (top) and computer (bottom).

A set of finger goniometry methods in anatomy is adopted to measure the angles (Figure 4-16) . Considering the accuracy and convenience of this experiment, active radial abduction and ulnar adduction are measured mainly via the CMC joint of the thumb (Angle No. 2, 3) but also the MCP joint of the index finger (Angle No. 4, 5). In the same way, active palmar flexion and dorsal extension are measured via the DIP and the PIP of the index finger (Angle No. 7, 8, 10, 11), same as the MCP joint of the index finger and the CMC joint of the thumb (Angle No. 1, 6, 9). More specifically, each gestures are maintained by following the goniometry procedures: 1) for measuring each index finger stretch and thumb abduction/adduction, the examiner stabilises the volunteer's finger and maintains the palm in a vertical position along the white reference line, then aligns each arm of the goniometer with the dorsal midline of the corresponding phalanx; 2) for measuring each thumb stretch and index finger abduction/adduction, the examiner places the volunteer's index finger along the white reference line, maintains the metacarpal in a neutral position and prevents radial deviation at the wrist, then aligns arms of goniometer with the dorsal midline of the corresponding phalanx [131].

The three participants are researchers from an engineering university. Their age range is from 25 to 40 years old, and they are all male. All of them have received basic training with the goniometer. Table 4-5 represents the angle results of each joint: the thumb carpometacarpal (TCMC) joint; the thumb metacarpophalangeal (TMCP) joint; the index metacarpophalangeal (IMCP) joint; the index proximal interphalangeal (IPIP) and the index distal interphalangeal (IDIP). For each participant the virtual angle results are correspondingly compared with the manual measuring results. Average differences between the virtual angles and the manual measured angles from the three participants are 1.68° , 3.20° and 3.15° .

To confirm the significance of the results with respect to the angles measured and the participants, an analysis of variance (ANOVA) is held. "Participant" and "Joint" are considered as independent variables, and angle error value as the response variable. The results from the analysis indicated that, "Participant" is not

statistically significant (P-value of 0.291). “Joint” is not also statistically significant (P-value of 0.822). These results indicate that neither the “Participant” nor the “Joint” they are measuring are key parameters for the angle error obtained.

Table 4-5 Goniometry experiment results from three participants.

		Participant A			Participant B			Participant C		
		(deg)			(deg)			(deg)		
		Real	Virtual	Dif.	Real	Virtual	Dif.	Real	Virtual	Dif.
1.	TCMC extension	50.00	50.84	0.84	41.30	43.59	2.29	49.00	50.10	1.10
2.	TCMC adduction	16.00	15.33	0.67	22.85	25.49	2.64	26.00	20.90	5.10
3.	TCMC abduction	54.60	56.43	1.83	46.30	45.14	1.16	50.00	56.20	6.20
4.	IMCP adduction	19.00	17.23	1.77	17.80	15.6	2.20	28.00	23.70	4.30
5.	IMCP abduction	34.00	34.67	0.67	40.4	41.53	1.13	42.00	41.70	0.30
6.	IMCP extension	16.00	15.46	0.54	14.3	21.10	6.80	15.00	12.40	2.60
7.	IPIP extension	6.00	5.94	0.06	6.00	15.19	9.19	3.00	6.50	3.50
8.	IDIP extension	14.50	14.97	0.47	20.30	18.39	1.91	14.00	15.60	1.60
9.	IMCP flexion	91.00	91.46	0.46	84.15	80.9	3.25	86.00	81.00	5.00
10.	IPIP flexion	88.20	79.74	8.46	84.15	82.9	1.25	88.00	89.00	1.00
11.	IDIP Flexion	3.70	6.48	2.78	1.00	4.47	3.47	9.00	5.00	4.00

4.7 Conclusions

A prototype to measure fingers motion is presented in this chapter. Several points deserve discussion beginning with the validation process with volunteers. Due to the different motives of measuring angle, this paper does not strictly follow the standard joints measurement flow. With the aim of better verification, some specific gestures, such as flexion close to 90° at IMCP and IPIP joints, are required instead of extreme flexion because the angle has to do with the elasticity of the tendon and joint when close to extreme limits, which may cause the instability of actual angle value. It is more important to verify the precision of this device rather than to obtain each finger range of motion. However, there are still some extreme gestures remaining for covering as many situations as possible.

Nonetheless, the observers’ errors when using the universal goniometer is the limitation for the reference group. Additional experiment is worth be carried out to make a better comparison with

the virtual angles obtained from our prototype, against real angles measured by other advanced direct measurement systems such as OES or flexible EG. Taking into account the accuracy of other prevailing measurements, the Vicon mocap system provided mean accuracy of 89.33% with root mean square error of 5.19° [122], the CyberGlove specification claimed sensor resolution is under 1° with repeatability of $\pm 3^\circ$ [132]. Based on the above, we are able to indicate that the value of virtual angles is very close to the real angles, and the precision is at the same level of the mainstream measurement devices and products.

It is worth mentioning that, the whole hardware system so far, including seven sensors for two fingers, costs around 225 EUR in total, purchased from Arduino component supplier. Considering the price of other direct measurement systems, the commercial inertial sensor product such as Xsens MVN, is approximately 12,000 EUR; referring to the OES, the price range is approximately from 5,000 EUR of Kinect to 55,000 EUR of Vicon. It is interesting to get a device that would relatively keep in the low-cost level in the market.

For assessing the ergonomic risk and preventing MSDs exposures, capturing motion angle data is only the pre-step for the entire progress. The next technical stage should be to analyse those movements together with force data by using a mathematical model within a software and the help of an expert. To achieve this, various biomechanical analysis software applications are available, such as 3DSSPP [133]. Likewise, based on its adaptability, the use of this system can also be extended to assembly lines in the other industrial fields where the worker's safety is a concern.

Chapter 5:

Developing 3D printed conductive trace board

5.1 Introduction

This chapter is focused on developing a non-conventional wired solution to connect motion capturing components. To do so, a functional prototype is further developed with the combination of additive manufacturing techniques and electrically conductive thermoplastics.

As for the electronics, the BNO055 9-degree-of-freedom IMU sensor model (Adafruit, New York City, NY, United States) and a Beetle microcontroller model (DFRobot, Shanghai, China) is used as the main functional hardware (Figure 5-1). The open-source Arduino IDE is considered reliable multi-functional software for the purpose of prototyping a smart device because of its high compatibility and accessibility. Likewise, the Beetle is chosen because it is one of the smallest microcontrollers on the market that works with the Arduino

IDE and for the purpose of being worn in a wearable device. According to its datasheet, the IMU sensor needs a power line (VIN), a ground line (GND) and an I2C bus line, which are represented by a SDA line and a SCL line. These four pins connect to the Beetle, which has 2 through-hole pins on the VIN and GND lines, and 2 surface-mount pins on the SDA and SCL lines.

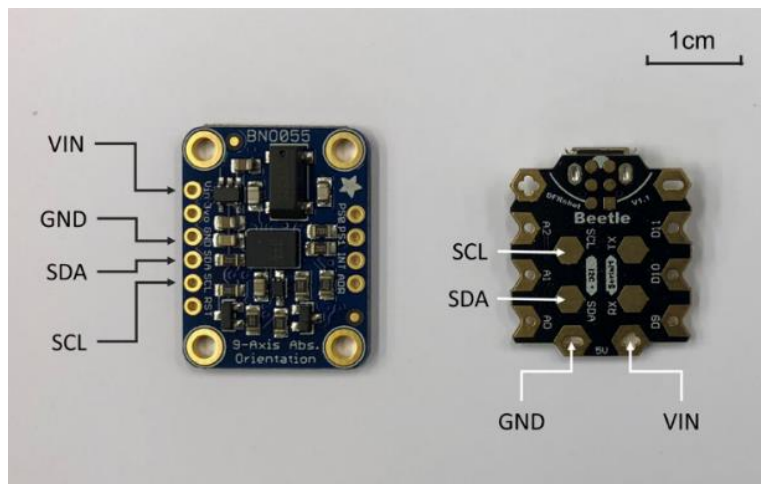


Figure 5-1 the IMU sensor and Beetle microcontroller.

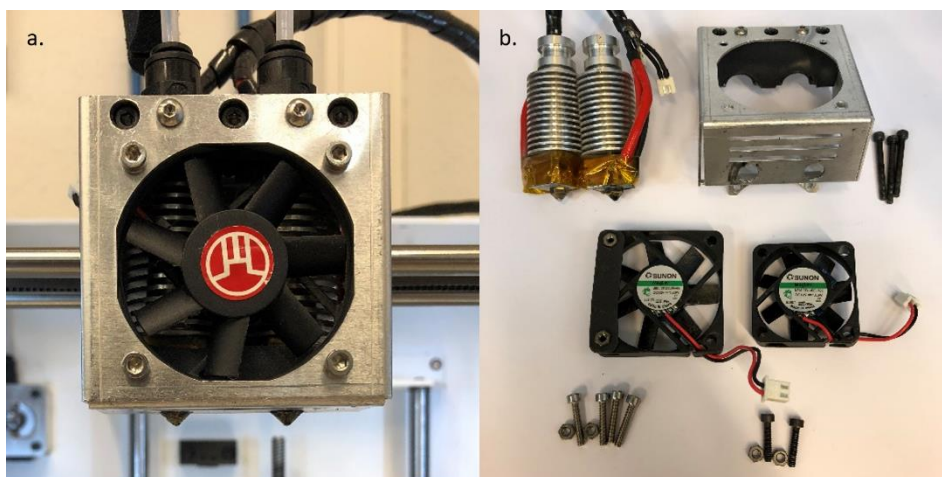


Figure 5-2 a) the Tumaker extruder head and b) disassembled extruder.

For the Additive Manufacturing technology, the selected low-cost extrusion printer is the Tumaker Voladora Dual™ (Tumaker, Oiartzun, Spain), which uses two Bowden extruders with 0.6 mm

diameter nozzles with a separation of 2.6 cm (Figure 5-2.a). A disassembled hotend is showed in Figure 5-2.b. The printer uses Simplify3D (Simplify3D, Blue Ash, OH, United States) to control the printing process. This dual extrusion will allow to print the conductive thermoplastic composite material for circuit traces, and the non-conductive plastic material for an integrated shell to fix components.

5.2 Cross-contamination factors

The regular dual printing process introduces the inherent issue of cross-contamination. For this study, since the conductive filament is going to be deposited along with a non-conductive material in order to electrically isolate adjacent conductive paths, cross-contamination could result in either a short circuit between two adjacent conductive traces or an interruption of a conductive trace with non-conductive material [99]. Through an early test of dual printing, multiple aspects are considered to cause cross-contamination occurred.

- **Over-tight spatial arrangement:** it leads to a merge of several regions of the two trace as Figure 5-3 shows. When some part of the component size is designed smaller than the extrusion width, different materials are overflowed and mixed together, or even the printing path is not calculated. However, a proper outline overlapping still conduces to a strong adhesion to avoid internal shedding among different components. This will be further discussed together with Infill Extrusion Width in Section 5.7.1.

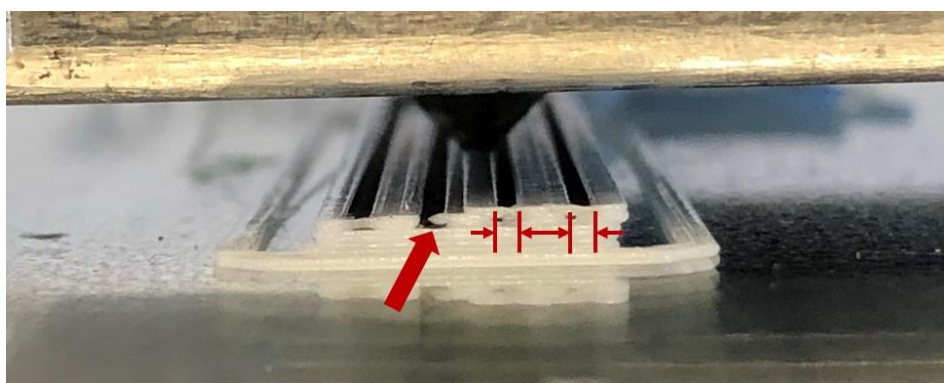


Figure 5-3 Partly overlapped traces due to the trace width is smaller than the extrusion width.

- **Excessive pressure:** if the distance between the nozzle and the bed is too small, it will hinder or block normal extrusion, causing irregular overflowing as Figure 5-4 shows. In some cases, excessive resistance will even cause the filament knot at the Bowden driver.

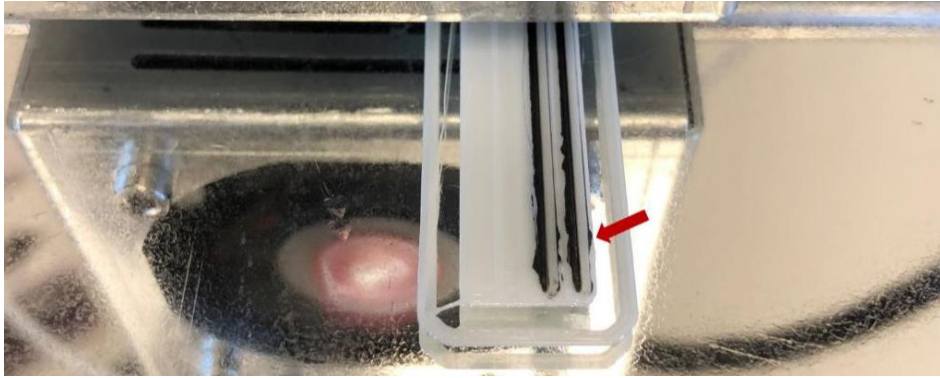


Figure 5-4 Conductive material overflowed under an insufficient nozzle height.

- **Secondary melt:** if the nozzle with the conductive material is at high temperature and it moves on the surface of the non-conductive material, the nozzle will melt all the printed external material again. Then the mixed materials will become stringing or form to droplets and adhere to the nozzle or other part of the object, causing cross-contamination as Figure 5-5 shows.

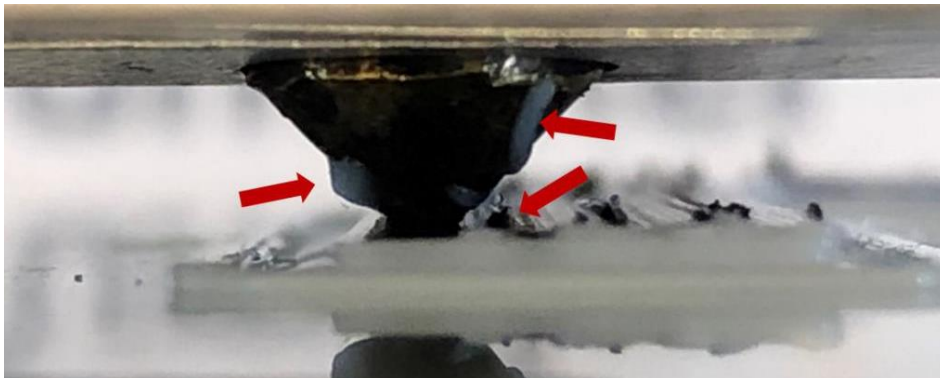


Figure 5-5 Secondary melted materials are mixing together and causing cross-contamination.

- **Incorrect extrusion configuration:** it may cause different types of failure. The conductive material is overflowed to the white

intervals because overheating or extrusion multiplier value is set too high. In fact, most 3D printers do not provide a way to monitor how much filament is actually extruded out. Due to the fact that the hydrodynamic properties and expansion coefficients of each material are different, this precise extrusion requires a big amount of operator effort in order to adjust relevant settings of individual print materials (an example of improvements is showed in Figure 5-6).

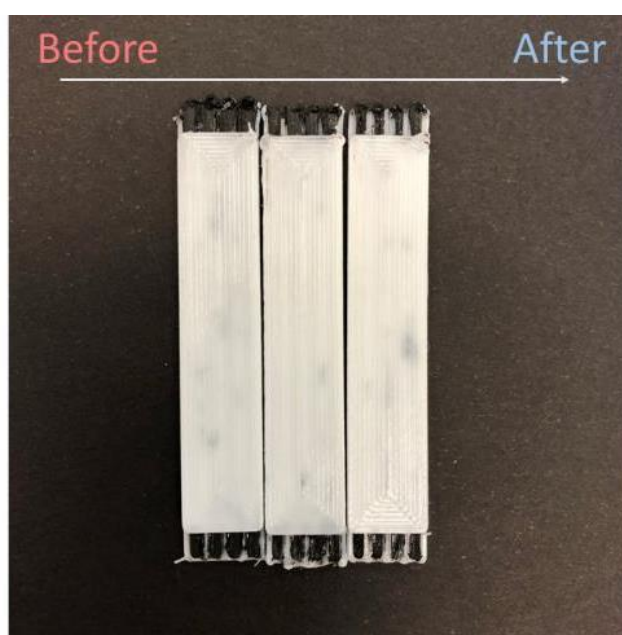


Figure 5-6 The extrusion accuracy is improved after configuring extrusion settings.

- Stringing (otherwise known as oozing, whiskers, or “hairy” prints): stringing is a fundamental obstacle when facing the cross-contamination problem. Technically speaking, melted filament always tends to continuously leak out of the nozzle with a certain oozing velocity while the extruder is moving to a new position, which is the reason of stringing as Figure 5-7 shows. Most of the 3D printing software applications offers a function called “retraction” to improve the oozing issue. If retraction is enabled, when the extruder is finishing the current path, the filament will be pulled backwards into the nozzle with a certain distance and retracting speed against oozing. Next, the extruder moves rapidly

to a new route starting point while the retraction movement is still effective, or namely just before the filament is about to ooze out of the nozzle. When it begins printing again, the filament will be pushed forwards in order to extrude in perfect timing just before drawing the route. Although it is effective, this over-frequent pull & push movement of the filament in the nozzle will make filament extrude inaccurately, or even causes material clogged inside the nozzle.

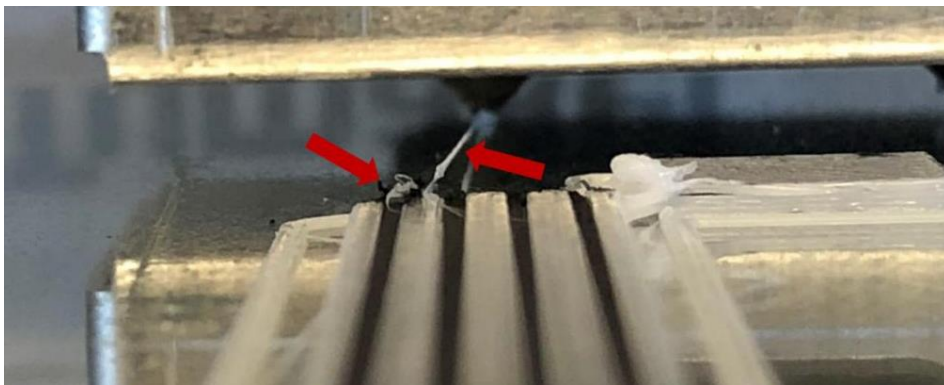


Figure 5-7 Stringing effect when the nozzle moved to new position. A stringing ball is formed pointed by the left arrow when the stringing is broken.

- **Unreasonable routing planning:** affected by the stringing problem, unreasonable route planning also worsens the printing quality. The object usually is heavily contaminated when the extruder is crossing different components. To solve this, there are two ways of optimizing the route planning. On one hand, one idea is to find a travel path that avoids crossing different materials, which means that less chance to create a string, because the nozzle will be on top of the same polymer and will not travel outside the part most of the time. In “advanced tab” of Simplify3D, to enable the option “Avoid crossing outline for travel movements” can significantly improve the route calculation result. The detour factor is depending on the specific printing object. In the present case, this value is included in Table 5-7 of section 5.7.1. On the other hand, due to the nozzle’s alignment in the printer, proper object orientation is also critical to prevent cross-contamination. Specifically, the conductive paths should be perpendicular to the imaginary line connecting the two nozzles. Otherwise, if the path

and imaginary line are in parallel, another nozzle will always leak following/ahead of the working nozzle.

Finally, it must say that each factor can cross-affect to others. For instance, a poor retraction will cause stringing on the nozzle or remain on the printing object, which also leads to the hot nozzle make the material a secondary melt on the nozzle, or merged into the object. Another example, incorrect extrusion configuration, such as over-high printing speed, together with complex route planning and stringing, would mess up the result.

5.3 Fabrication process

In this study, two main novel approaches are combined and preformed to reduce the cross-contamination effect: 1) switching nozzle temperatures while printing and 2) selecting the proper cross-section of the conductive paths (this will be introduced in section 5.4.5). An optimized printing setting is concluded at Table 5-7.

Regarding the first approach, in terms of printing strategy, a specific G-Code procedure is implemented without any hardware add-on. In appendix G [134], a description and explanation of most important g-code lines are presented. These codes are implemented within the “Tool Change Script” sub-tag of Simplify3D to dynamically control the nozzle movements and temperatures. Three scripts are created ad hoc:

- Starting script (Appendix H): this script starts after the print task is uploaded to the printer. Several parameters are initialized such as metric values and absolute mode. Next, the nozzle moves to the home position and receives two nozzle temperatures which are defined in “Per-layer Temperature Setpoints” of Temperature tab. Then the extruder is zeroed and extrudes 35 mm of filament to avoid under-extrusion while the printing task begins.
- Tool change script (Appendix I): after the two nozzles are loaded with conductive and non-conductive filaments, the first nozzle prints the corresponding layer (220°C) while the second nozzle is kept at a semi-melting temperature (160 °C). When the first nozzle

finishes depositing the material on the layer, the second nozzle must continue printing the layer. This last step includes the execution of several commands before the second nozzle starts printing:

- a. Switch to absolute positioning mode (“G90”) and move the printing head to a pre-set standby coordinate, in this case, the south-west position of the tray (“G1 X100 Y10 F5000”).
- b. Zero the Z value (“G1 Z0 F1200”), namely lift the bed along the Z axis until both nozzles are in close contact with the bed (Figure 5-8.a). Otherwise, the material may keep leaking and form a blob while the head is idle, leading to a clog in the nozzle and pasting the blob to the printing object, as Figure 5-8.b shows.
- c. Stay in the resting position, change the nozzle temperatures (“T[old_tool]; M109 S160 T[old_tool]; T[new_tool]; M109 S220 T[new_tool];”): Cool down the first nozzle and heat the second nozzle.
- d. Switch to relative positioning mode (“G91”), lift the head to a height that is higher than the object that is being printed (“G1 Z3 F1200”).
- e. Switch back to absolute positioning mode (“G90”), finish all moves and go back to print the new layer (“M400”).

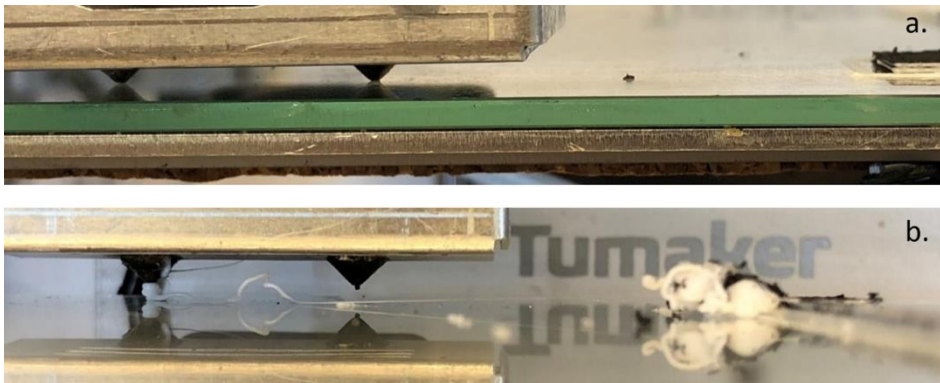


Figure 5-8 a) Hot end changing temperature at the resting position; b) Filament clog in the left nozzle when the hot end suspending at the resting position.

- Ending script (Appendix J): after finishing the printing progress, the extruder heater and bed heater are turned off. Then retracts 10 mm filament to avoid leaking on the object surface. In the meantime, moving the extruder to the upper left corner of the printer, and lowering the bed so as to easily take off the printed object. Lastly shut down the steppers.

5.4 Design of experiments

At this stage, several parameters need to be determined before manufacturing the final prototype that connects the IMU with the microcontroller. First, the maximum allowable resistance for the four conductive paths (VIN, GND, SDA, SCL) that will connect the two boards have to be calculated. Then, a test will be run to select the most suitable commercially available conductive filament. Finally, important cross-contamination factor (infill pattern) and several printing settings (temperature, speed and layer height) are studied in order to minimize the resistivity of the printed conductive path. In each one of the experiments, the ends of the testing specimens are painted with Silver Conductive Paint (Electrolube, Ashby de la Zouch LE65, United Kingdom) and dried at room temperature (20 °C) overnight, so as to reduce contact resistance as much as possible. Next, the resistances of each specimen will be measured using a multimeter.

5.4.1 Step 1. Maximum allowable resistance

When connecting PCBs with copper wires, the connection will not feature any voltage loss due to the low copper resistivity (1.7×10^{-8} ohm · cm). As all electrically-conductive filaments feature an inherent resistance due to the presence of the polymer matrix, the first step is to determine the maximum path resistance to ensure a proper connection between the IMU and the Beetle. To that end, three tests are carried out with the following set-up.

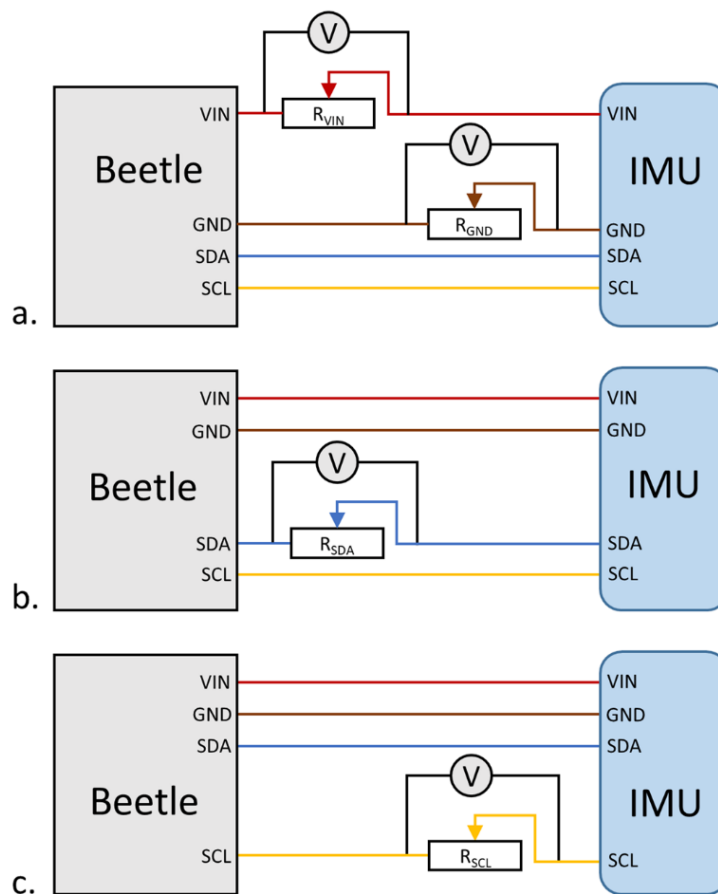


Figure 5-9 a) Test for maximum external resistance on the VIN-GND lines b) Test for maximum external resistance on the SDA line c) Test for maximum external resistance on the SCL line.

For the first test, two potentiometers are placed on the VIN line and the GND line simultaneously and in parallel with a voltage meter, while the data lines (SDA and SCL) are directly connected by copper wires (Figure 4-2.a). A series of values for the potentiometer resistance are adjusted while the communication status is evaluated by monitoring the correct data flow on a PC connected to the Beetle. For the second test, the SDA line is connected to a potentiometer along with the voltage meter, while the other lines are copper-wired (Figure

4-2.b). The last test is similar, but the SCL line is evaluated (Figure 4-2.c). The results obtained from these tests are shown in section 5.5.1.

5.4.2 Step 2. Conductive thermoplastic composites

The next step involves selecting the best commercially available conductive material. For the initial selection of the conductive materials, two main constraints are considered. Firstly, it has to be a commercially available material, so other researchers are able to consider the result of this project as a baseline for their developments. Then, the cost of the material needs to be reasonable (< 150 USD). Moreover, the materials have to feature the lowest possible resistance while also meet other parameters such as ease of printing and material handling. Considering this, three different materials are analysed: Rubber 3D Printing PI-ETPU 95-250 Carbon Black™ (Palmiga Innovation, Höganäs, Sweden), XF Nano Conductive Flexible TPU Filament (XFNANO, Nanjing, China), and Black Magic 3D Conductive Graphene PLA filament (Graphene 3D Lab, New York City, NY, United States). The three materials are acquired from regular suppliers and several specimens are printed in accordance with manufacturer recommendations to verify the theoretical resistivity value provided by the specification sheet. Three prism specimens with a cross-section of 2 by 2 mm and a length of 50 mm are printed for each material. The volume resistivity is calculated:

$$\rho = R \ S / L \quad [8]$$

Where R is the resistance, L is the specimen length and S is the cross-sectional area. The results of these tests are shown in Section 5.5.2.

5.4.3 Step 3. Printing settings: infill

After selecting the material, the printing settings are established beginning with the infill option. Three types of infill patterns are examined with prism specimens (50 mm long, 4.8 mm width and 2 mm height). A rectilinear infill pattern is selected for the internal volume, where the angle offsets are set to 90° (longitudinal pattern, along the

trace), 0° (transversal pattern, across the trace) and 0° / 90° (alternatively along or across the trace by layers), as shown in Figure 5-10 respectively. All the specimens are printed at a nozzle temperature of 200 °C, a speed of 30 mm/s and a layer height of 0.2 mm. Within Simplify3D, other settings are fixed: the extrusion multiplier is set to 1.0, the number of top, bottom and outline solid shells is set to 1, the extrusion width is fixed at 0.6 mm; at the same time, in order to minimize the presence of air pours within the conductive material, an infill percentage of 100%, an outline overlap of 30% and an infill extrusion width of 60% are set. This resulted in a distance of 0.36 mm between beads. Three specimens are printed for each type of infill; the results of these tests are shown in section 5.5.3.

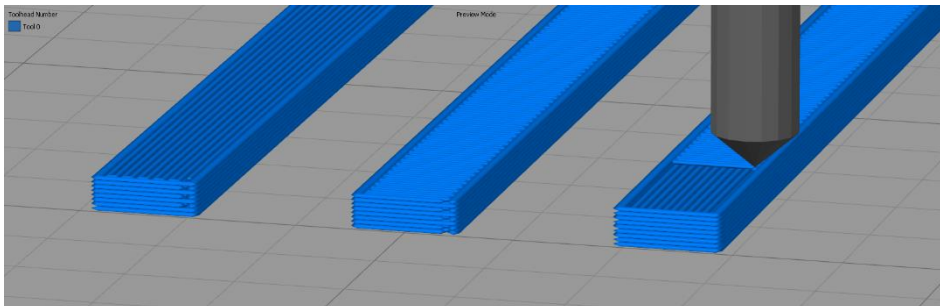


Figure 5-10 Printing simulation of three infill patterns on Simplify3D preview mode: longitudinal pattern, transversal pattern, alternating layer pattern from left to right.

5.4.4 Step 4. Printing settings: temperature, speed and layer height

Although 3D printing filaments are strictly manufactured using a unified extrusion approach, different brands of 3D printers or printing settings can alter the final printing results. In order to seek out the best printing settings that apply to our printer, a battery of prism specimens (50 mm long, 1.2 mm width and 2 mm height) is tested by considering printing speed, printing temperature and layer height as variables which could affect the volume resistivity. The rest of the settings are the same as in the previous experiment; Table 5-1 shows all process variables and their levels. All these variable values result in 36 combinations. Each combination is printed three times for a total of 108 specimens. The printed specimen is a prism with a length of 50

mm, a height of 2 mm and a width of 1.2 mm (Figure 5-11). The specimens' width and the extrusion width of 0.6 mm result in two longitudinal moves of the head to deposit the material for each layer. An ANOVA is performed to verify the effects of the above parameters on the specimens' resistivity. The best basic printing settings will be chosen based on the results of the ANOVA, which are shown in section 5.5.4.

Table 5-1 Process variables and their levels for the ANOVA.

	Level 1	Level 2	Level 3	Level 4	Level 5	Level 6
Printing temperature (°C)	200	210	220	-	-	-
Printing speed (mm/s)	7.5	10	12.5	15	20	30
Layer height (mm)	0.1	0.2	-	-	-	-

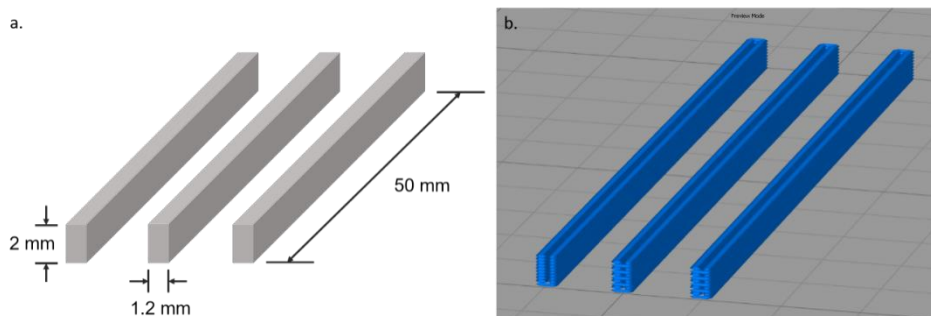


Figure 5-11 Specimen dimensions (a), preview of the specimens in Simplify3D (b).

5.4.5 Step 5. Cross-sectional shape of conductive paths

Once the printing settings are selected, the cross-section geometry of the conductive paths are studied, since it can have a considerable influence on cross-contamination. Firstly, three patterns of cross-section layouts are designed and compared via experimental conductive trace boards (Figure 5-12). All the sections are supposed to have areas similar to the ones calculated in the previous experiments on the proper working of the VIN, GND and two data lines. Hence, the GND line is wider and the two data lines are smaller. As flexibility is going to be a key parameter for future work beyond this project, it is set to 1 mm. The width is then calculated accordingly. The first type is a normal rectangular pattern, with each trace being insulated by 0.6-

mm-thick flexible thermoplastic polyurethane (FTPU) material, which is the thinnest of nozzle extrusion width (Figure 5-12.a). The second type is designed in a diamond pattern, with each trace also being insulated by FTPU material but the width is double the width of the first test (Figure 5-12.b) to reduce the potential contact area between traces. Finally, the third type has an air gap with a total isolation distance of 1.8 mm between each trace, so as to increase the flexibility of the prototype at the same time (Figure 5-12.c).

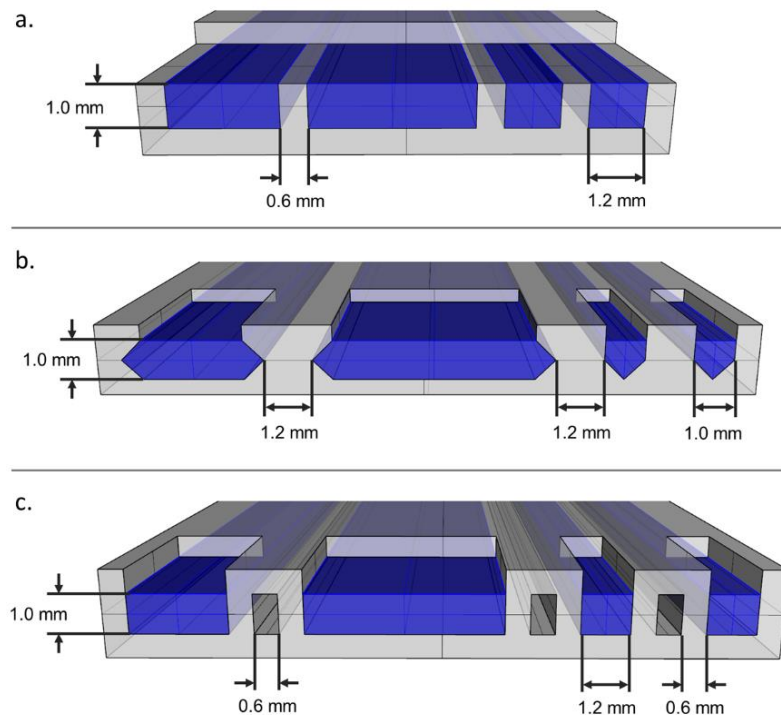


Figure 5-12 Cross-section pattern models: a) Rectangular pattern; b) Diamond pattern; c) Air gap pattern.

Specimens are printed in accordance with these three layout designs and the resistance between each line on the same side is measured to verify whether there is any short circuit. The printing settings used for this step are the best ones obtained in Step 3 (infill) and Step 4 (temperature, speed and layer height) along with the other previously fixed settings. In addition to this, an ANOVA is performed to verify whether the cross-section area is related to the resistivity by

printing specimens with a length of 50 mm but with different cross-section areas in a rectangular pattern. For this study, the maximum cross-section studied is 0.024 cm², which corresponds to the area of the specimen used for studying the temperature, speed and layer height. Hence, sections of 0.006 cm², 0.012 cm², 0.018 cm², and 0.024 cm² are tested following the same fabrication process. The results are also shown in section 5.5.5.

5.5 Results of experiments

5.5.1 Determination of Maximum allowable resistance

Results from the power line and ground line test (explained in Step 1, section 5.4.1) are shown in Table 5-2, where “Y” refers to the correct data flow and “N” refers to abnormal error such as invalid data flow or data interruption. As for the data lines, the resistance value manages to reach 5000 ohms, due to the fact that the data lines operate in an open drain.

Table 5-2 Result of resistances for combined VIN and GND.

VIN (ohm)	0	25	50	75	100	125	GND (ohm)
200	N	N	N	N	N	N	N
175	Y	Y	N	N	N	N	N
150	Y	Y	Y	N	N	N	N
125	Y	Y	Y	Y	N	N	N
100	Y	Y	Y	Y	Y	N	N
75	Y	Y	Y	Y	Y	Y	N
50	Y	Y	Y	Y	Y	N	N
25	Y	Y	Y	Y	Y	N	N
0	Y	Y	Y	Y	Y	N	N

5.5.2 Selection of conductive thermoplastic composites

Table 5-3 summarises the results of the filament selection process. Black Magic 3D shows the lowest resistivity at 0.43 ohm · cm, while the filament from Palmiga Innovation has a mean resistivity of 319.20

ohm · cm. The filament from XF Nano has a low resistivity value officially (1.25 ohm · cm), although after repeated tests it is impossible to print a viable specimen since it is too soft to extrude from the Bowden driver. Summing everything up, the Black Magic 3D is the chosen conductive filament for the subsequent steps since it presented the lowest resistivity, its cost is reasonable, and at the time of the study, it is available from suppliers without restrictions (Table 5-3).

Table 5-3 Results from the comparison of commercially available materials.

<i>Material</i>	<i>Core polymer</i>	<i>Resistance (ohm)</i>	<i>Actual Resistivity (ohm·cm)</i>	<i>Official Resistivity (ohm·cm)</i>	<i>Price (100g)</i>
		85.00	340.00		
<i>PI-ETPU 95-250 Carbon Black (Palmiga Innovation, Höganas, Sweden)</i>	<i>Carbon Black</i>	75.80	303.20	< 800	\$12.29
		78.60	314.40		
<i>XF Nano (XFNANO, Nanjing, China)</i>	<i>Graphene</i>	<i>Unable</i>	<i>Unable</i>	< 1.25	\$150.44
		88.90	0.43		
<i>Black Magic 3D (Graphene 3D Lab, NY, U.S.A)</i>	<i>Graphene</i>	89.70	0.43	0.6	\$100.00
		91.30	0.44		

Developing a printable conductive filament is not a simple task, as an appropriate balance needs to be struck between the manufacture of conductive material that allows for a semi-molten state during printing and the appropriate conductivity of the printed electrode [135]. When undertaking this study, we only consider those materials that are commercially available to the public in online shops as candidates. Apart from the above-mentioned printing materials that we chose, Electrifi is another conductive filament with a resistivity of only 0.014 ohm · cm that we could have used in this study. Because those resistivity values are very low, it would have helped increase the length of the conductive paths - i.e. the separation between hardware boards - without affecting normal working of the sensor. However, its availability is limited as we did not find any shops that sold it.

5.5.3 Selection of internal infill pattern

Results from the test explained in Step 3 (section 5.4.3) indicate that the longitudinal infill provides the lowest resistance: mean values for the longitudinal pattern (90°), the transversal pattern (0°) and the

alternating pattern (0-90°) are 27.17, 48.87, and 35.93 ohms, respectively. Therefore, according to these results, deposited paths shall run parallel to the current.

5.5.4 Determination of temperature, speed and layer height

Table 5-4 shows the specimens' resistivity values for all combinations of printing temperatures, printing speeds and layer heights as explained in Step 4 (section 5.4.4). The normality of the values and the homogeneity of the variances are checked before running the ANOVA. Data is normally distributed (p-value = 0.192), while Bartlett's test and the F-test demonstrated that each combination of the groups of the three printing parameters proved homogenous in terms of variances (Temperature p-value = 0.656, Speed p-value = 0.058, Layer height p-value = 0.887 with a significance level of $\alpha = 0.05$).

Table 5-4 Result of printing parameter test using Black Magic 3D.

<i>Temp.</i> (°C)	<i>Speed</i> (mm/s)	<i>Layer height</i> (mm)	<i>Resistivity</i> (ohm-cm)	<i>Temp.</i> (°C)	<i>Speed</i> (mm/s)	<i>Layer height</i> (mm)	<i>Resistivity</i> (ohm-cm)
220	30	0.2	0.44352	210	12.5	0.2	0.45696
220	30	0.2	0.43008	210	12.5	0.2	0.44832
220	30	0.2	0.432	210	12.5	0.2	0.46032
220	30	0.1	0.43344	210	12.5	0.1	0.45024
220	30	0.1	0.41616	210	12.5	0.1	0.46896
220	30	0.1	0.41664	210	12.5	0.1	0.49344
220	20	0.2	0.42672	210	10	0.2	0.45168
220	20	0.2	0.43056	210	10	0.2	0.43008
220	20	0.2	0.43824	210	10	0.2	0.44256
220	20	0.1	0.45072	210	10	0.1	0.50832
220	20	0.1	0.42576	210	10	0.1	0.492
220	20	0.1	0.44496	210	10	0.1	0.48672
220	15	0.2	0.48	210	7.5	0.2	0.4968
220	15	0.2	0.48192	210	7.5	0.2	0.46752
220	15	0.2	0.47184	210	7.5	0.2	0.46368
220	15	0.1	0.45984	210	7.5	0.1	0.5064
220	15	0.1	0.44832	210	7.5	0.1	0.49056
220	15	0.1	0.49344	210	7.5	0.1	0.49296
220	12.5	0.2	0.47136	200	30	0.2	0.43056
220	12.5	0.2	0.45024	200	30	0.2	0.41664
220	12.5	0.2	0.48816	200	30	0.2	0.42288
220	12.5	0.1	0.44448	200	30	0.1	0.46224
220	12.5	0.1	0.43968	200	30	0.1	0.45696
220	12.5	0.1	0.44016	200	30	0.1	0.45504

<i>Temp.</i> (°C)	<i>Speed</i> (mm/s)	<i>Layer height</i> (mm)	<i>Resistivity</i> (ohm·cm)	<i>Temp.</i> (°C)	<i>Speed</i> (mm/s)	<i>Layer height</i> (mm)	<i>Resistivity</i> (ohm·cm)
220	10	0.2	0.45552	200	20	0.2	0.4176
220	10	0.2	0.47472	200	20	0.2	0.42192
220	10	0.2	0.444	200	20	0.2	0.43392
220	10	0.1	0.43392	200	20	0.1	0.44928
220	10	0.1	0.42768	200	20	0.1	0.45408
220	10	0.1	0.44688	200	20	0.1	0.45312
220	7.5	0.2	0.5184	200	15	0.2	0.4728
220	7.5	0.2	0.52704	200	15	0.2	0.46512
220	7.5	0.2	0.49488	200	15	0.2	0.46896
220	7.5	0.1	0.52752	200	15	0.1	0.4872
220	7.5	0.1	0.49824	200	15	0.1	0.4584
220	7.5	0.1	0.52272	200	15	0.1	0.48144
210	30	0.2	0.43344	200	12.5	0.2	0.46944
210	30	0.2	0.43584	200	12.5	0.2	0.44208
210	30	0.2	0.42768	200	12.5	0.2	0.4488
210	30	0.1	0.42096	200	12.5	0.1	0.46272
210	30	0.1	0.42768	200	12.5	0.1	0.46848
210	30	0.1	0.44832	200	12.5	0.1	0.48432
210	20	0.2	0.40896	200	10	0.2	0.49632
210	20	0.2	0.42624	200	10	0.2	0.48528
210	20	0.2	0.42864	200	10	0.2	0.48576
210	20	0.1	0.46176	200	10	0.1	0.49104
210	20	0.1	0.44256	200	10	0.1	0.48
210	20	0.1	0.4368	200	10	0.1	0.49872
210	15	0.2	0.4584	200	7.5	0.2	0.51168
210	15	0.2	0.52848	200	7.5	0.2	0.50496
210	15	0.2	0.46416	200	7.5	0.2	0.50304
210	15	0.1	0.52224	200	7.5	0.1	0.50592
210	15	0.1	0.4992	200	7.5	0.1	0.50928
210	15	0.1	0.47664	200	7.5	0.1	0.49872

The ANOVA shows a significant three-way interaction among the three parameters; the full interaction plot is presented in Figure 5-13. In analysing this plot, several conclusions can be drawn about the best parameters for printing the prototype. First, the ‘Speed’ column clearly indicates that this parameter is significant, showing the lowest resistance values at higher speeds (20 and 30 mm/s). Second, the ‘Layer height’ column shows that at these two speeds, the layer height of 0.2 mm has lower resistance than printing with 0.1 mm. Finally, moving to the ‘Temp.’ column, at between 20 and 30 mm/s, the selection of the temperature values is not so critical since at both speeds the trend lines are almost flat. Nonetheless, considering that the flexible filament for subsequent dual printing shows better

printing performance at 220 °C and that the official recommended printing temperature for the Black Magic conductive filament is also 220°C, the temperature is defined on this degree.

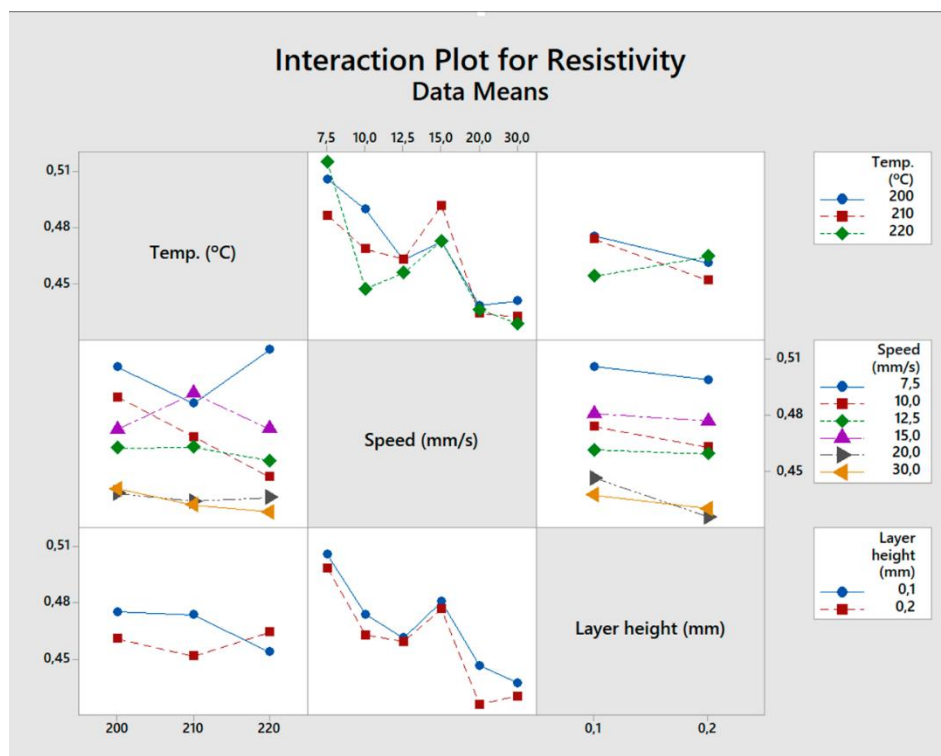


Figure 5-13 Full interaction plot from the ANOVA.

The printing speed is finally set to 20 mm/s, as to a higher speed may have resulted in nozzle clogs for flexible filament. Based on these results, the values of 220 °C, 20 mm/s, 0.2 mm are selected at this stage for the filaments.

Simplify3D provides numerous options for adjusting printing quality. We chose printing speed, printing temperature and layer height, because those three parameters are likely to be considered three of the fundamental aspects that affect results. Specifically, printing speed affect tensile stress and flexural strength [136]; printing temperature is critical because an under-melted filament might clog the nozzle while an over-melted filament can lead to conductivity loss, since the inherent properties of the filament will

have changed [137]. The layer height is also chosen because it might affect the infill stacking density and layer adhesion [138]. These printing parameters generally determine whether or not printing could be carried out, which is not related to a specific printing task.

5.5.5 Selection of conductive paths cross-section

The three types of cross-sections designed in Step 5 are printed in different specimens as shown in Figure 5-14. Inter-resistance levels between each adjacent line are measured once for each side to verify insulation among traces. The image in Figure 5-15, taken with a Leica DC300 digital microscope camera, shows a specimen featuring the air gap strategy.

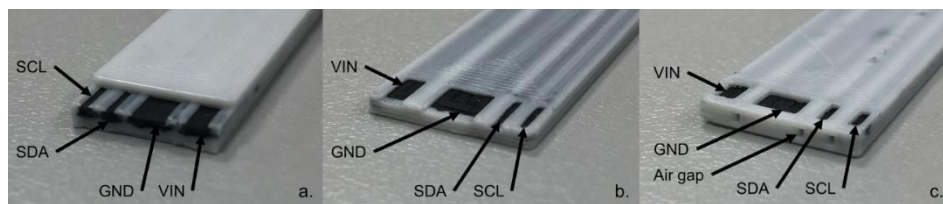


Figure 5-14 Specimens with different cross-section patterns: a) rectangular, b) diamond and c) air gap.

Table 5-5 demonstrates that only the air gap pattern fully insulates all the lines.

Table 5-5 Resistance among traces as result of the cross-section pattern test.

<i>Cross-section pattern</i>	<i>VIN – GND (ohm)</i>	<i>GND – SDA (ohm)</i>	<i>SDA – SCL (ohm)</i>
<i>Rectangular</i>	<i>insulated</i>	<i>2680</i>	<i>540</i>
	<i>insulated</i>	<i>3860</i>	<i>640</i>
<i>Diamond</i>	<i>insulated</i>	<i>750</i>	<i>220</i>
	<i>insulated</i>	<i>1140</i>	<i>880</i>
<i>Air gap</i>	<i>insulated</i>	<i>insulated</i>	<i>insulated</i>
	<i>insulated</i>	<i>insulated</i>	<i>insulated</i>

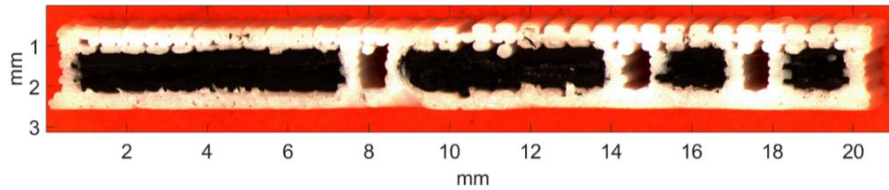


Figure 5-15 Microscope image of the 3D-printed sample featuring the air gap strategy.

Table 5-6 shows the resistivity results of the specimens with different rectangular cross-section sizes as explained in Step 5. The ANOVA demonstrates that the area is not statistically significant in terms of resistivity when the cross-section area ranges from 0.006 cm^2 to 0.024 cm^2 (p-value = 0.164).

Table 5-6 Resistivity by cross-section area.

Cross-section		Area (cm^2)	Resistivity (ohm-cm)
Width (mm)	Height (mm)		
0.6	1	0.006	0.6348
			0.6144
			0.5868
0.6	2	0.012	0.5592
			0.5496
			0.5712
1.2	1	0.012	0.636
			0.5736
			0.5952
1.2	2	0.024	0.5712
			0.5712
			0.5952
1.8	1	0.018	0.594
			0.6012
			0.6372
2.4	1	0.024	0.5664
			0.5952
			0.6

It is worth mentioning that although specimens within the same test are printed from the same material spool, it is noticed that different batches of the conductive filament may lead to resistivity differences. In the previous tests, the resistivity results from the printing parameter test have a mean resistivity of $0.463 \text{ ohm} \cdot \text{cm}$, while the results from the cross-section area test have a mean resistivity of $0.592 \text{ ohm} \cdot \text{cm}$ since we used different Black Magic 3D batches. This supports the strategy of using a safety coefficient when designing the conductive paths of the final prototype.

5.6 Prototype design

The final prototype is modelled in Rhinoceros (Robert McNeel & Associates, Seattle, WA, United States) and the general view of the prototype from the top is shown in Figure 5-16. It has the following features regarding the conductive paths:

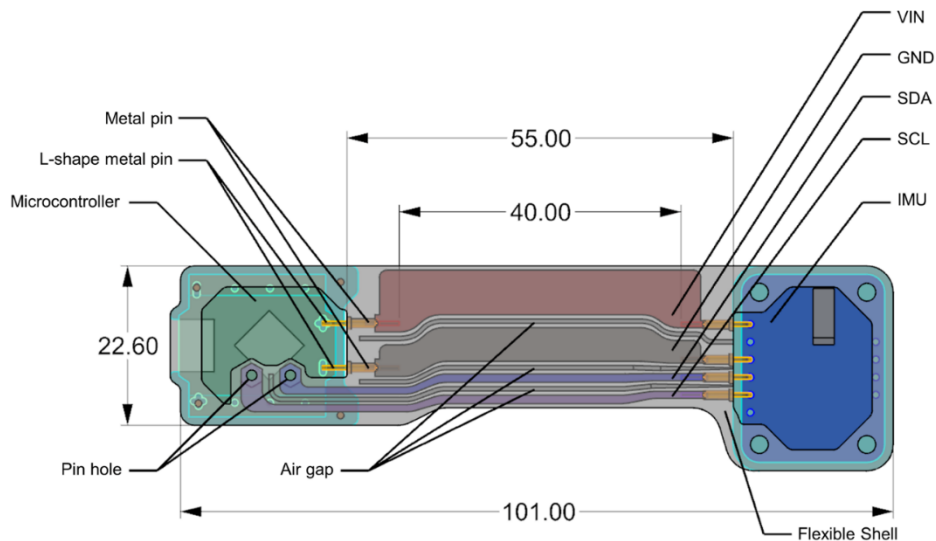


Figure 5-16 Top view of prototype layout. All dimensions in mm.

- All path heights are set to 1 mm to obtain a prototype that is flexible in a bending movement.
- The length and cross-sections consider a safety coefficient of 1.67, i.e. they are calculated with a resistivity of $1 \text{ ohm} \cdot \text{cm}$ (according to the official volume resistivity, $0.6 \text{ ohm} \cdot \text{cm}$), in

order to take a certain allowance for uncontrollable conductivity loss into consideration.

- Each conductive path has different width based on the results obtained from previous steps. The final cross-section width for each trace in accordance with the limitation are 6.34 mm for the VIN line, 4.8 mm for the GND line, and 1.2 mm for the SDA and SCL lines.

5.6.1 Pin connections

Moreover, two strategies are taken into consideration for connecting the conductive paths and the electronics (Figure 4-16 and Figure 5-18). Firstly, a 1.5-mm-diameter vertical hole is drilled through the conductive material and flexible shell at the end of the SDA and SCL lines on the Beetle side (Figure 4-16). In parallel, a planar metal pin of approximately 0.1 mm in thickness is soldered to the PCB, and then the trace board is assembled on the PCB and the hole is aligned correctly with the planar metal pin. Finally, a small portion of tin (3 mm) is soldered into the hole to fully join everything.

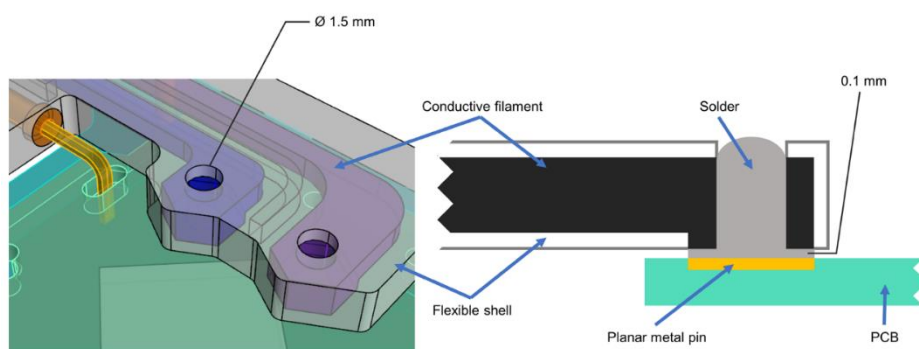


Figure 5-17 Pin connection: metal pin soldering with 3D printed hole.

A second type of male-female pin is applied to all four pins on the IMU side, as well to the rest pins (VIN and GND) on the Beetle side (Figure 5-18). The horizontal hole in the conductive path is first 3D printed and then expanded using a 0.5-mm-diameter drilling tool. The metal pin and the hole are both covered with silver ink, and then the pin is immediately inserted into the hole and left overnight to dry. An L-shaped metal pin is soldered to the through-hole pin of the PCB.

Finally, the L-shaped metal pin is physically inserted into the male-female pin.

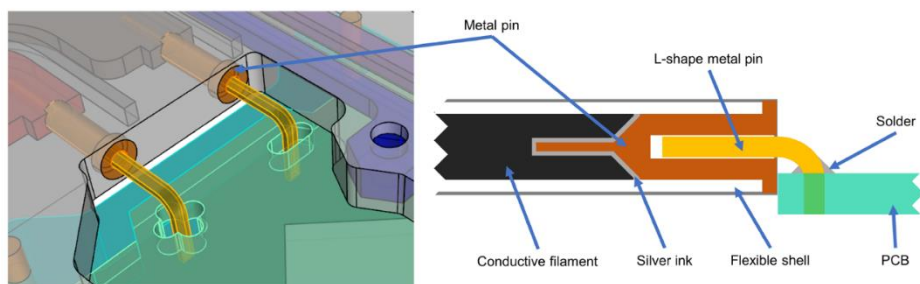


Figure 5-18 Pin connection: male-female metal pin model.

5.7 Prototype manufacturing

5.7.1 Relevant techniques and improvements

Although the most important printing settings are discussed above, some of the other important configurations highly depend on the specific project demand, object design, or extruder route planning. For instance, the tuning of the values on Outline Overlap and Infill Extrusion Width will change the number of the tracks and the size of interspace. In Figure 5-19, multiple interspace appear along the outline of each component because the resolution of the infill tracks is too low (Outline Overlap of 0%, Infill Extrusion Width of 100%), namely means the unit infill extrusion width is too wide. Such interspace may significantly increase the volume resistivity, but also the unbalanced infill may weaken the inner structural strength.

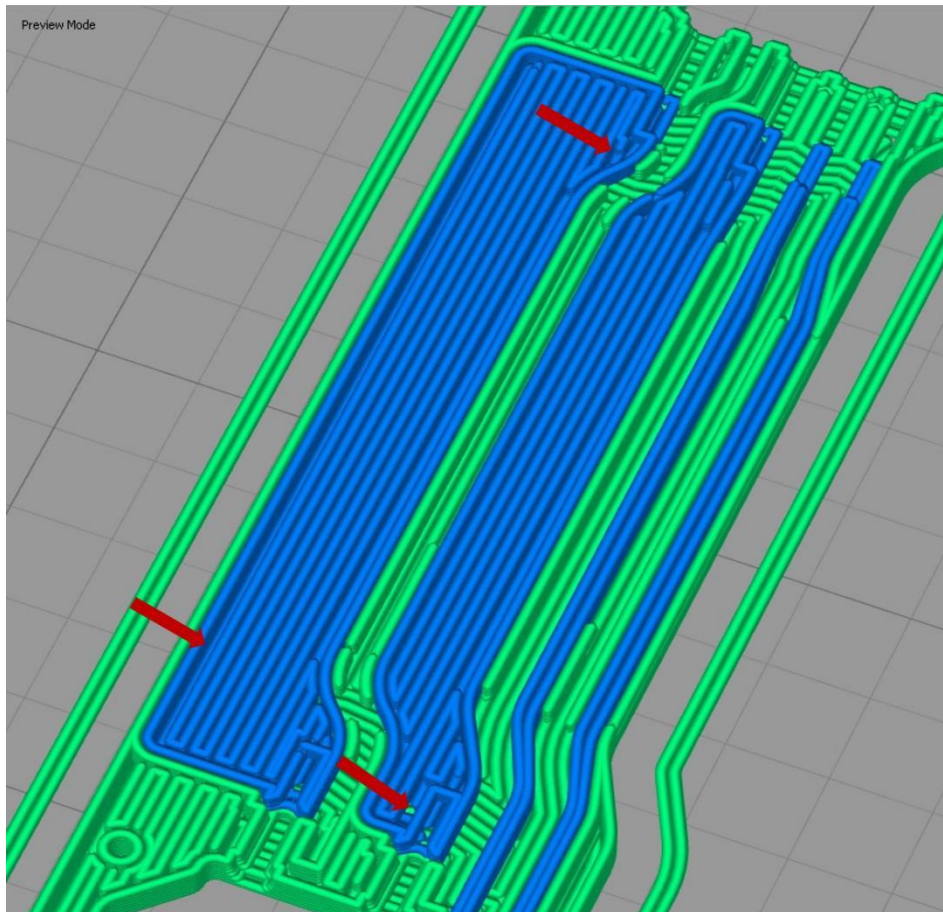


Figure 5-19 Under-filled components. Arrows indicate the interspaces that may occur.

In Figure 5-20, a higher resolution of infill in the preview mode seems to improve the interspatial issue (Outline Overlap of 80%, Infill Extrusion Width of 40%). Yet, an over tight fill or over big outline overlap may cause severe overflow in the real printing process because excessive times of infill travel, which in turn, will lead to unpredictable short circuits. Therefore, a balanced set of Outline Overlap and Infill Extrusion Width values shall base on the situation of each own task. The final set that we have decided are Outline Overlap of 30%, and Infill Extrusion Width of 60%.

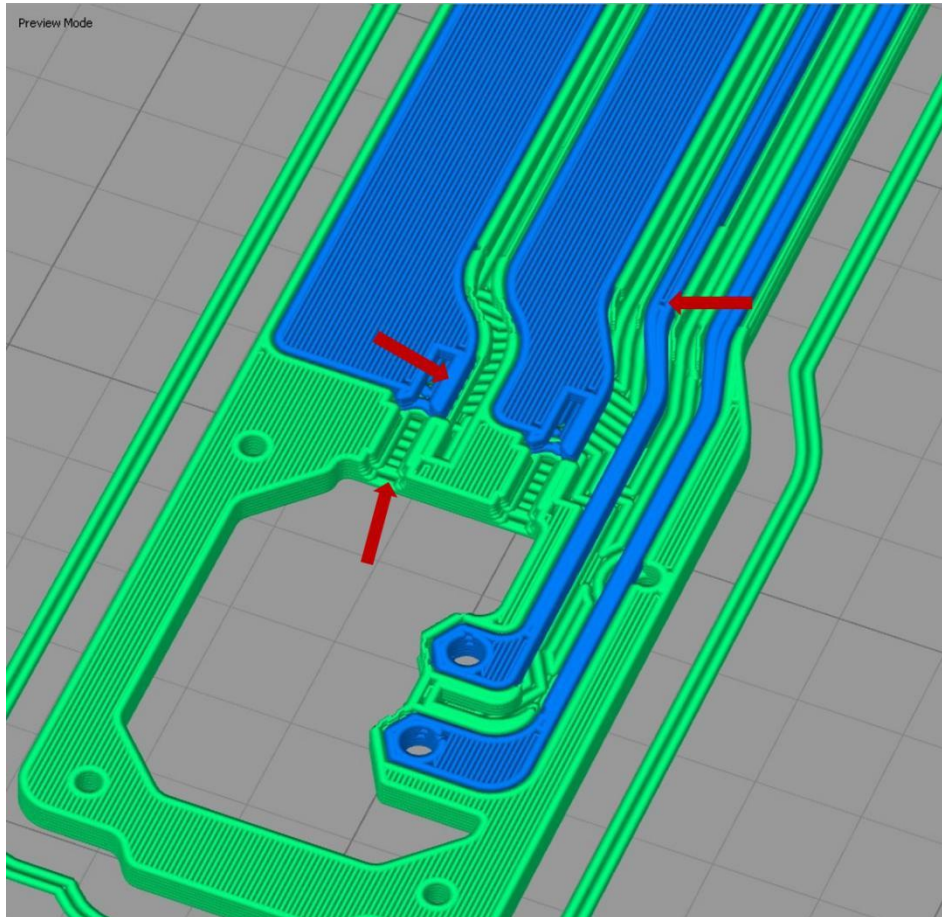


Figure 5-20 Over-filled components. Arrows indicate the overflows that may occur.

In another case, proper use of prime pillar may also greatly improve the printing result. Basically, prime pillar is helpful when multiple filaments are extruded through one nozzle. Because the prime pillar will be the primary thing printed when changing material, which will ensure that the working nozzle is primed and ready to print. However, it is found that to enable prime pillar in a dual print is effective as well.

- First, as its fundamental use, the deposition of the current prime pillar layer first will avoid under-extrusion when the extruder returns back from the resting position.

- Secondly, the prime pillar will minimize the stringing or clogging since it prevents from carrying the small portions of the material to the printing object.
- Thirdly, having the same purpose as the resting position, prime pillar will change the movement route to an external area, instead of starting at the next tool changed layer directly.

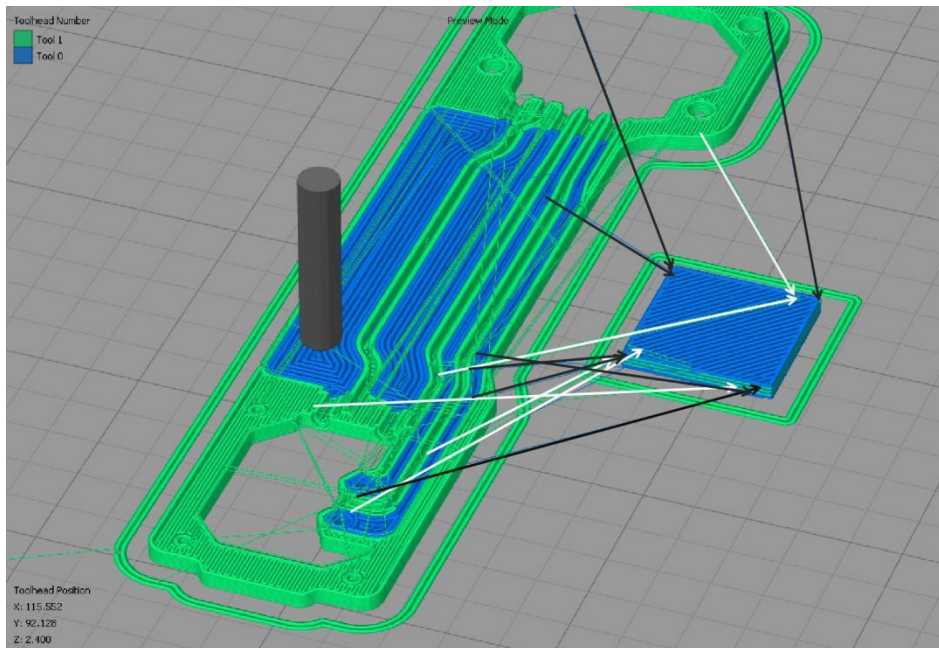


Figure 5-21 Prime pillar placed at east side.

Nevertheless, the position of the prime pillar will affect how the stringing crossed the region between the prime pillar and printing object. In Figure 5-21, the prime pillar is placed on the east of the object. The white arrows refer to the movement track of the nozzle extruding non-conductive flexible material, and the black arrows refer to the movement track of the nozzle extruding conductive material. Both of them have multiply crosses over the conductive traces, which lead to worse cross-contamination on the printed object. Though in Figure 5-22, while the prime pillar is placed on the southwest of the object, all the arrows cross the outer shell which is not affected to the conductivity of the trace.

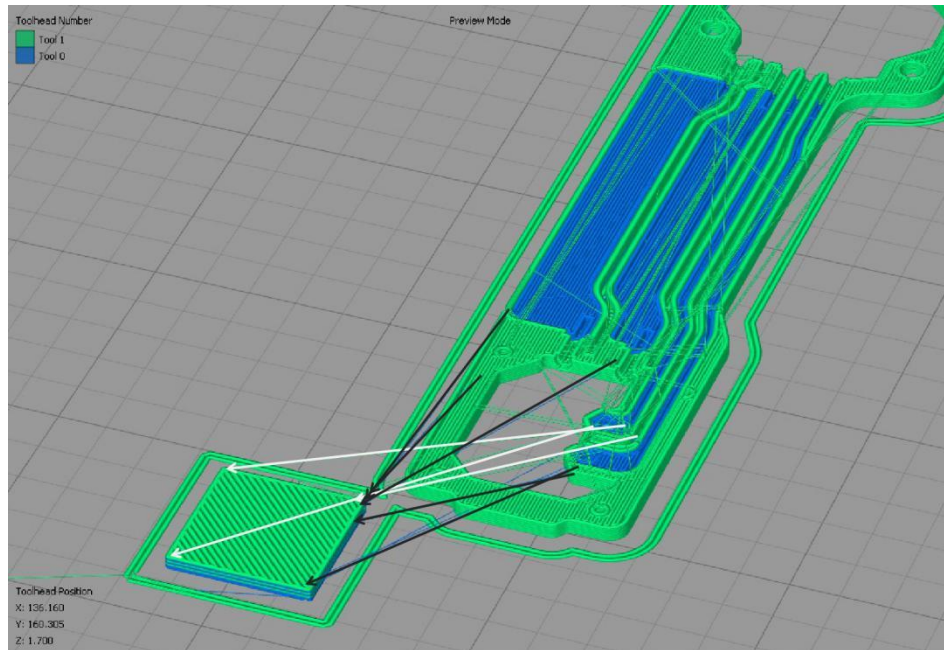


Figure 5-22 Prime pillar placed at southwest side.

Combined with some existing techniques in literature and the author's experiences, several strategies to relieve the contamination are implemented in Simplify 3D:

- The nozzle diameter and the extrusion width keep the same value (0.6 mm)
- The “Extrusion Multiplier” is set to for both nozzles at 1.
- Both materials are using “Retraction” for reducing stringing on FTPU and conductive filament part. Configuring retraction settings of the left nozzle and right nozzle separately can effectively improve the incoincidence of the stringing results due to the different physical features of dual materials.
- The rigid conductive filament can retract at the speed of 80 mm/s. However, the flexible filament must retract with a lower speed of 30 mm/s.
- “Top Solid Layer”, “Bottom Solid Layer”, “Outline/Perimeter Shells” are all set up to 1, in order to reduce the affect that abundant layers change component's size.

-
- “Skirt/Brim” is activated to prevent unexpected extrusion at the beginning.
 - “Prime Pillar” avoids heavy cross contamination every time when switching the nozzle/material.
 - “Ooze Control Behavior” and “Movement Behavior” are enabled.

Summing up everything, all the settings in Simplify3D that have been determined for printing this prototype are organized in Table 5-7.

Table 5-7 Summary of modified printing settings in Simplify3D.

<i>Tab</i>	<i>Settings</i>	<i>Right nozzle (Black Magic)</i>	<i>Left nozzle (FPLA)</i>	<i>Bed</i>
Extruder	<i>Nozzle Diameter</i>	0.6 mm	0.6 mm	
	<i>Extrusion Multiplier</i>	1.0	1.0	
	<i>Extrusion Width</i>	0.6 mm	0.6 mm	
	<i>Retraction Distance</i>	10.0 mm	10.0 mm	
	<i>Extra Restart Distance</i>	0 mm	0 mm	
	<i>Retraction Vertical Lift</i>	2.1 mm	0.6 mm	
	<i>Retraction Speed</i>	80 mm/s	30 mm/s	
	<i>Coasting Distance</i>	0.6 mm	0.6 mm	
	<i>Wipe Distance</i>	2.0 mm	0.6 mm	
Layer	<i>Primary Extruder</i>	Left		
	<i>Primary Layer Height</i>	0.2 mm		
	<i>Top Solid Layers</i>	1		
	<i>Bottom Solid Layers</i>	1		
	<i>Outline/Perimeter Shells</i>	1		
	<i>Outline Direction</i>	Inside-Out		
	<i>First Layer Height</i>	100%		
	<i>First Layer Width</i>	100%		
	<i>First Layer Speed</i>	80%		
Additions	<i>Skirt Extruder</i>	Left		
	<i>Skirt Layers</i>	1		
	<i>Skirt Offset from Part</i>	2.0 mm		
	<i>Skirt Outlines</i>	2		
	<i>Prime Pillar Extruder</i>	All Extruders		
	<i>Pillar Width</i>	15.0 mm		
	<i>Pillar Location</i>	South-West		
	<i>Speed Multiplier</i>	100%		
	<i>Internal Fill Pattern</i>	Rectilinear		
	<i>External Fill Pattern</i>	Concentric		
	<i>Interior Fill Percentage</i>	100%		
	<i>Outline Overlap</i>	30%		
	<i>Infill Extrusion Width</i>	60%		
	<i>Minimum Infill Length</i>	0.0 mm		
<i>Combine Infill Every</i>	1			
Temperature	<i>Per-Layer Temperature Setpoints</i>	160 °C	220 °C	50 °C
Scripts	<i>Starting Script</i>	See on Appendix G		
	<i>Tool Change Script</i>	See on Appendix H		
	<i>Ending Script</i>	See on Appendix I		
Speeds	<i>Default Printing Speed</i>	20.0 mm/s		
	<i>Outline Underspeed</i>	100%		
	<i>Solid Infill Underspeed</i>	100%		
	<i>X/Y Axis Movement Speed</i>	200.0 mm/s		
	<i>Z Axis Movement Speed</i>	40.0 mm/s		
Advanced	<i>External Thin Wall Type</i>	Allow single extrusion walls		
	<i>Internal Thin Wall Type</i>	Allow single extrusion fill		
	<i>Allowed perimeter overlap</i>	50%		
	<i>Only retract when crossing open spaces</i>	enabled		
	<i>Force retraction between layers</i>	disabled		
	<i>Minimum travel for retraction</i>	2.0 mm		
	<i>Perform retraction during wipe movement</i>	enabled		
	<i>Only wipe extruder for outer-most perimeters</i>	disabled		
	<i>Avoid crossing outline for travel movements</i>	enabled		
<i>Maximum allowed detour factor</i>	90			

5.7.2 Manufacturing

The manufacturing process is undertaken individually by a single person. The whole printing progress takes approximately 2 hours, due to the extra nozzle temperature switching time and low printing speed. To start with, the filaments are placed in an oven at 50 °C overnight to remove moisture (Figure 5-23). The bed (a mirror) is then set to 50 °C and some hair spray apply to the bed before the printing starts to enhance adhesion. Next, the operator continues managing and monitoring the main printing procedure as described above, after which the specimen is processed and mounted with a metal pin and PCBs by hand as shown in Figure 5-24. Subsequently, the IMU sensor and the Beetle are assembled (Figure 5-25).



Figure 5-23 Conductive filament in the oven to remove moisture.

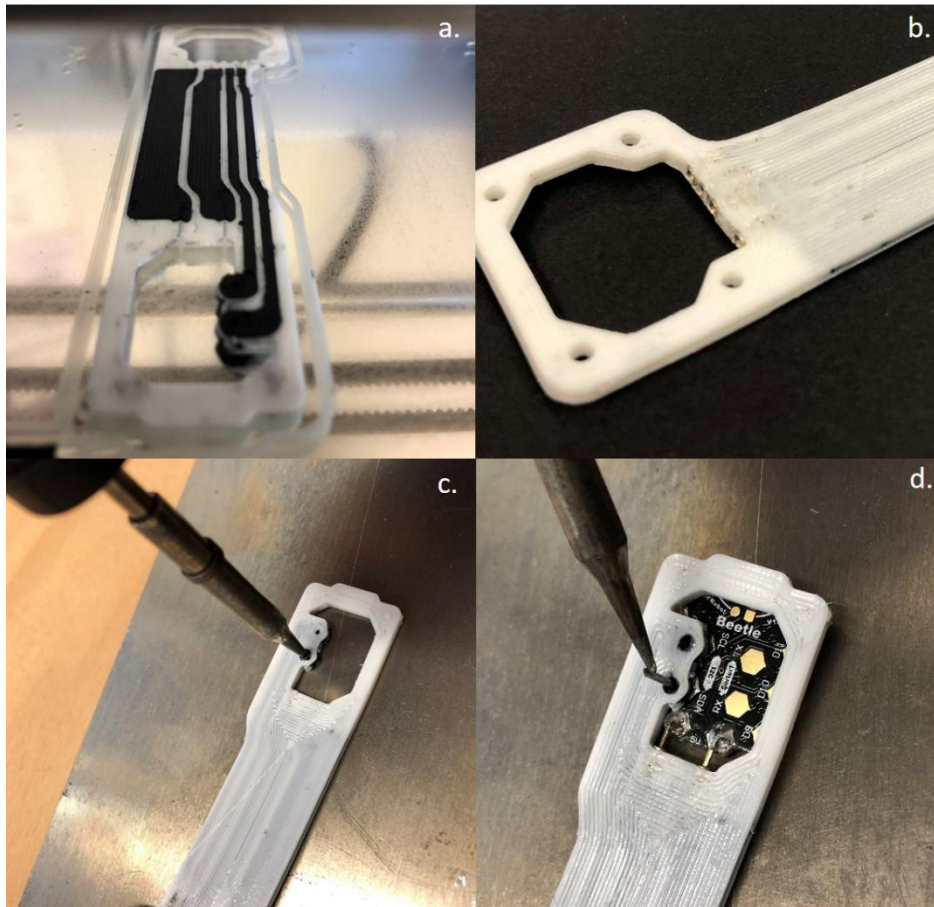


Figure 5-24 Assembly process: a specimen a) half printed; b) metal pin mounted; c) expanding the hole; d) soldering 3 mm tin into the hole.

After printing the prototype, the next step is to connect the boards. With respect to the connections between the PCBs and the conductive path, a robust and plug and play connections is needed wherever possible. From former experiences it is found that the best way is by expanding the hole by using drilling machine and later applying silver ink to maximise contact between the conductive material and the metal pin. However, a properly balanced amount of ink is required: a poor connection may occur if too little ink is used, while too much ink may cause overflowing and reach the adjacent pin hole, which leads to a short circuit. All these tasks are carried out manually, and so in this aspect, further development is still necessary, although we believe

that this strategy may be extrapolated to other types of PCBs without any problem.



Figure 5-25 Prototype: dual printed conductive trace board.

5.8 Prototype testing

5.8.1 Working verification

When the manufacture of the prototype is completed, several brief verifications are conducted. The resistance of each line is examined: the VIN line has 72.5 ohms, the GND line has 98.9 ohms, the SDA line has 375 ohms and the SCL line has 457 ohms. Then, the prototype is connected to a computer via a USB to run the software. The real time data flow can be observed in the serial monitor window (Figure 5-26), and the data signal is also observed using a digital oscilloscope (TDS 220, Tektronix, United States). Figure 5-27 shows that the signals worked properly.

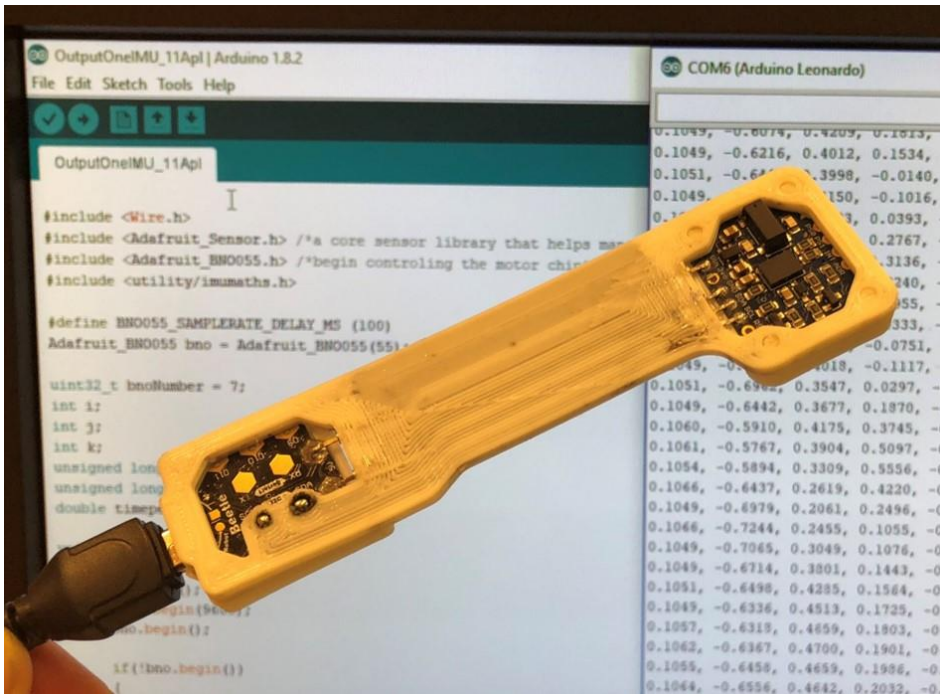


Figure 5-26 Data transmission through the prototype in real time.

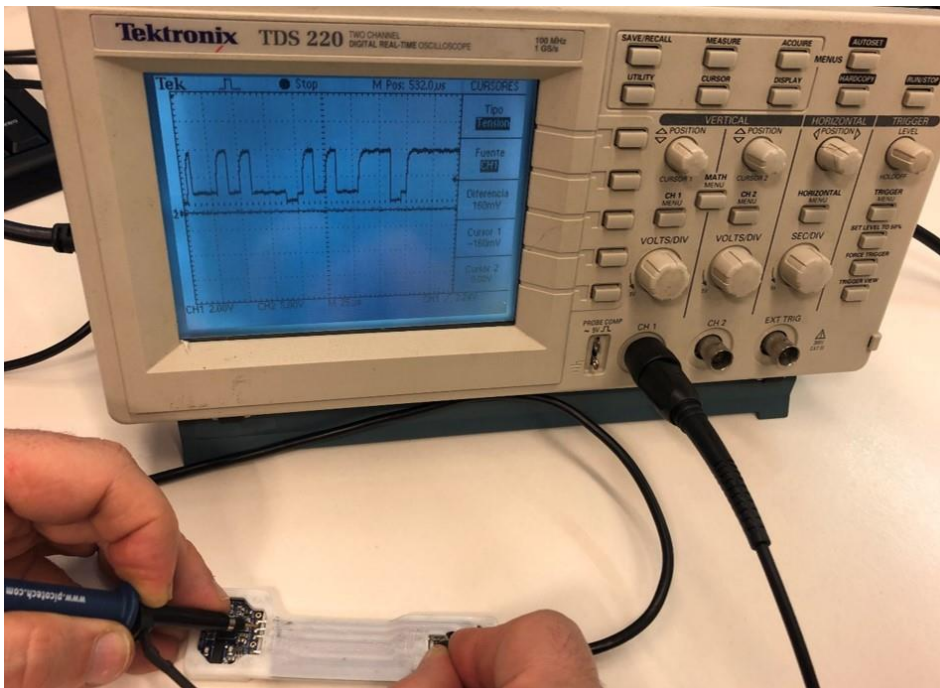


Figure 5-27 Signals on the digital oscilloscope screen.

5.8.2 Bending test

In this case, the actual resistance value set is very closed to the theoretical upper limit, which means the prototype has to maintain this value constantly no matter on any occasion. Although the maximum allowable resistance of the prototype has been found out and confirmed that the connection worked well, the deformation by external forces whether affects the resistivity still remains a doubt. Considering extension/flexion are the biggest and the most frequent deformation of a hand movement in the real application, an experimental test is performed to verify the effect of bending deformation on resistivity.

A 109-millimeter-long flexible board with three conductive specimens (BlackMagic3D) embedded inside is carried out for this test (specification details is showed in Figure 5-28). The inner conductive specimens are 100 mm long, with 1.2 mm width and 2 mm height. The processing methods and 3D printing configurations are exactly following the previous tests. A total of three trays are printed.

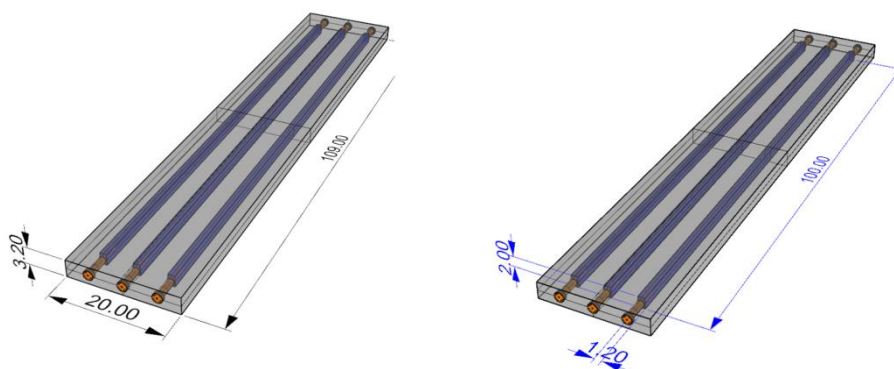


Figure 5-28 Specification of bending test board. Left: board size. Right: trace size.

The flexible board is tested in a universal test machine, Instron 4467 (Instron, Norwood, MA, United States) in turn. A three-point bending test is carried out: the specimen is supported in two points while and metal actuator pushed the specimen in a third point placed in the middle of the specimen.

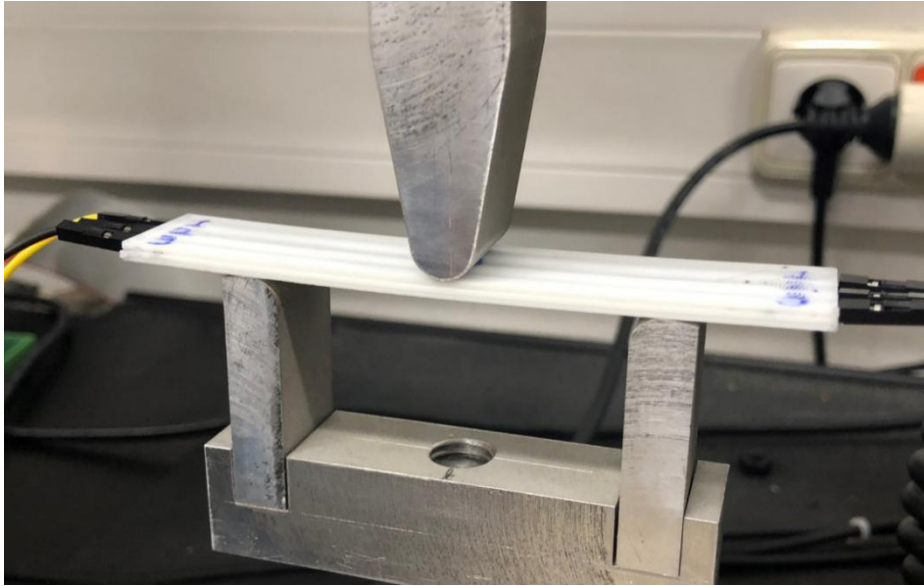


Figure 5-29 The specimen placed in flat with the metal actuator in the middle.

At the beginning of the experiment, the specimen rests in flat horizontally, and the resistance of each tray measured. Next, the actuator is moved down 2.5 mm and resistance values recorded. The process continues until getting 30 mm of displacement in the middle point (Figure 5-30). The bent angle on 30 mm displacement will arrive at 85 degrees, which is at a reasonable threshold that covers the save extension/flexion range of the human hand. After that, the metal head is moved back to the initial position to release the load. The tray is slowly returning back to the straight status but with slight radian. The last group of instant resistance and rebound displacement are instantly recorded.

After calculating the resistivity with the specimen's size, a total of thirteen groups of resistivity values and one group of rebound resistivity are noted in Table 5-8. Figure 5-31 shows the rebound status of the tray after the test.

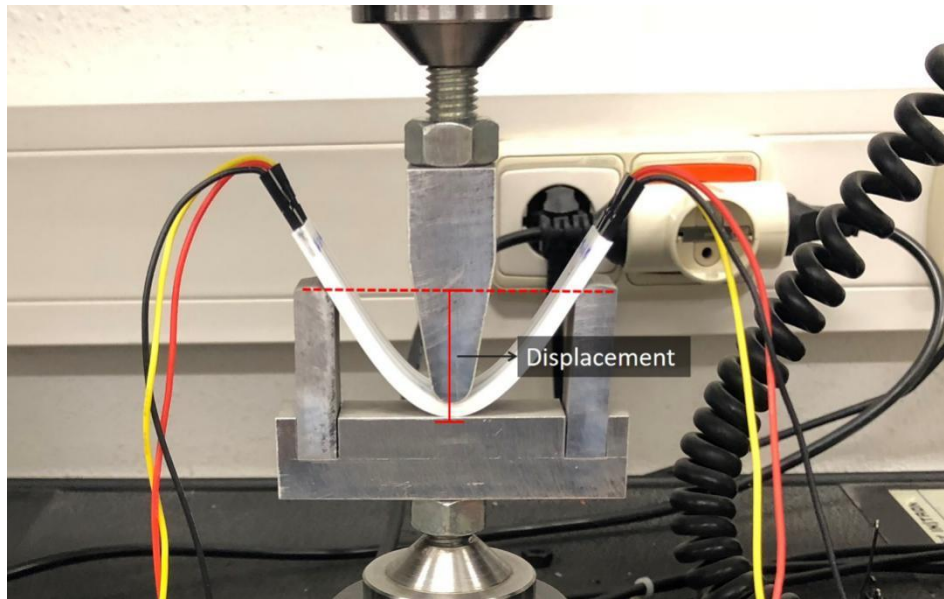


Figure 5-30 Measuring the instant resistance value in a bending test.

Table 5-8 Resistivity and the p-value at different deformation levels.

<i>Displacement (mm)</i>	<i>Resistivity</i>		
	<i>Specimen 1 (ohm cm)</i>	<i>Specimen 2 (ohm cm)</i>	<i>Specimen 3 (ohm cm)</i>
0	1.12	1.03	0.86
2.5	1.12	1.03	0.87
5	1.12	1.04	0.87
7.5	1.13	1.04	0.88
10	1.13	1.08	0.92
12.5	1.16	1.09	0.94
15	1.18	1.1	0.97
17.5	1.2	1.11	0.98
20	1.22	1.15	1.01
22.5	1.24	1.17	1.02
25	1.25	1.18	1.04
27.5	1.26	1.19	1.04
30	1.27	1.19	1.06
4.07*	1.14	1.05	0.89

* Rebound displacement when after releasing the metal head.

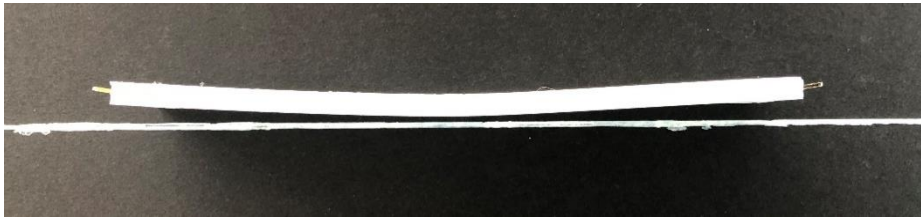


Figure 5-31 Samples after bending test with rebound deformation.

In Figure 5-32, a line chart demonstrates that the curve is nearly flat until the deformation distance to 10 mm, but also the curves do not show any significant sharp jumps. The specimen 3 has lower resistivity may due to the printing layout and different printing order compares to the other specimens. Nonetheless, the resistivity still remains in a reasonable range. Moreover, the rebound group reveals that the resistivity decreased to a similar level of the equal displacement, but a bit higher (mean of 1.01 ohm · cm at 5 mm level compare to mean of 1.03 ohm · cm at 4.07 mm level). Therefore, it is reasonable to consider that the bending movement will not significantly affect the specimen's resistivity. However, from 10 mm to 30 mm, the resistivity still increases 0.13 ohm · cm in average.

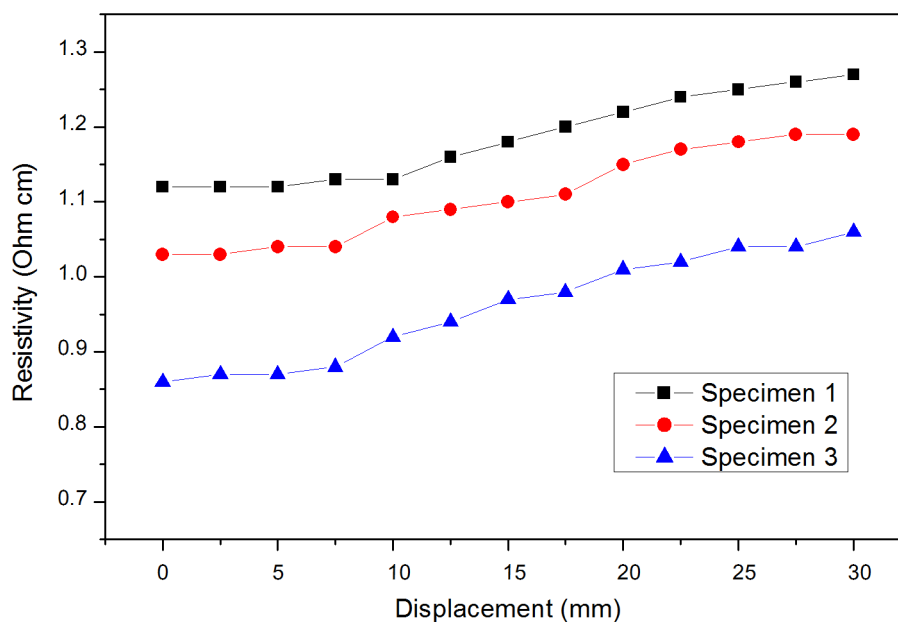


Figure 5-32 Resistivity changes at different deformation levels.

5.9 Conclusions

This part of study has presented a methodology for 3D printing embedded circuits using commercial graphene-based filament and FTPU filament to connect a MEMS sensor with a microcontroller. Several contributions can be highlighted about this project. During the prototyping process it is demonstrated that switching nozzle temperatures (between semi-melting temperature of 160 °C to a printing temperature of 220 °C) within the same layer is an effective and practical way of reducing the cross-contamination effect and printing a compact circuit with pinpoint accuracy, while utilising an air gap strategy to insulate the conductive trace is reliable for the purpose of preventing any short circuit. Moreover, in order to minimise resistivity, the infill pattern needs to be aligned to the electric current, while printing speed plays a significant role, a range of 20-30 mm/s is found the best for minimising the resistivity. Lastly, the rest printing settings, such as retraction, outline overlap and infill extrusion width, and prime pillar, are critical to the dual printing quality as well. Those configurations are more rely on the features of the printing object. The final prototype successfully connects the IMU sensor to the microcontroller and transmitted the data flow in real time while maintaining the physical elasticity to a certain degree.

Chapter 6:

Developing wrist motion capture glove

6.1 Introduction

Combining thermoplastic polymers with textiles means the possibility of personalized products and new process designs. It is also an inevitable topic of 3D printing technology in the field of wearable devices. In addition to aesthetic elements such as buttons, accessories or patterns, functional studies such as partial reinforcement, joint protection, and electronic integration are hot trends in the integration of 3D printing and textile.

Several studies have been done on the topic of 3D printing on textiles. Korger et al [139] emphasise that the adhesion of the polymer to the fabric is related to the topography of the textile surface and the textile surface energy. Grimmelsmann et al [140] consider that an appropriate distance (z-distance) between the print nozzle and the bed is the decisive factor for achieving good adhesion. Martens et al [141] focus on the interfacial adhesion after different washing cycles.

Spahiu et al [142] consider that the z-distance and the temperature of the bed and nozzle are important factors affecting the adhesion on the textile substrate. Spahiu et al [143] also study the relationship between printing speed, printing temperature, polymer flow, bed temperature and adhesion.

The purpose of this chapter is to illustrate the initial attempts regarding 3D print prototyping on textile materials. This includes studies about the adhesion of flexible materials on textiles, the degree of fabric deformation and the impact of the rebound resistance of the prototype. For these studies, the electronic components and the printing of circuit traces follow the methodology and experience of Chapters 4 and 5.

6.2 Selection of the textile

Regards that the purpose of this research is to develop a wearable measurement device suitable for hand, the fact of accurately reflecting the bending angle of the wrist is one of the basic requirements for the device.

For this selection process, common low elastic loose fabrics are not in the selection range, such as cotton, linen, woollens, and other warp knitted fabrics, etc. However, choosing a comfortable and soft textile that does not interfere with the user's work operation needs to be considered. Regarding the interaction of 3D printers and textiles, some studies publish several conclusions about 3D printing on textiles. Döpke et al [144], state that polymers do not have sufficient adhesion when performing 3D printing on thin textiles. Similarly, Korger et al. [139] print soft PLA and a thermoplastic elastomer (TPE) on different fabrics. As the fabrics are printed with materials of similar Shore hardness, they find that the adhesion forces are more dependent on the textile substrate than on the printing material: better adhesion can be obtained if the textiles are thicker and hairy. Another study [145] find that the adhesion properties are related to the porosity of the fabric and the layer height used while printing (Table 6-1). Finally, due to the fabric needs to withstand the extrusion fusion deposition of high-temperature nozzles on its surface, it is important to be thermostable.

Table 6-1 Maximum adhesion forces in N by type of fabric, layer height and printing material [7].

<i>Fabric</i>	<i>PLA</i>		<i>Filaflex</i>		<i>Average</i>
	<i>0.1 mm</i>	<i>0.2 mm</i>	<i>0.1 mm</i>	<i>0.2 mm</i>	
Viscose	22.5	9	40	57	32
Corduroy	55	90	60	120	81
Lycra Net (Small)	45	45	75	95	65
Lycra Net (Big)	75	80	120	110	96
Woven with elastane	22.5	50	70	20	40
Neoprene	40	114	200	160	128
Average	43	64	94	93	

Based on the above, it is found that the requirements for target textile are highly consistent with those used for sports protective gear and gloves. So considering the factors of thickness, elasticity, thermos ability and comfort and adhesion properties, Neoprene with a thickness of 2 mm is considered to be an ideal fabric for this wearable prototype.

**Figure 6-1 Sandwich structure of Neoprene.**

Neoprene is a polymer made from chloroprene as a monomer and emulsion polymerization with a sandwich structure, as shown in Figure 6-1. This textile has good resistance to climate, ozone aging, etc., and excellent on tensile strength, elongation, elasticity. Also, with properties of dustproof, anti-static, anti-scratch, it can be repeatedly

washed, but it is slightly airtight, and the usage temperature is from -35 to 130 °C.

6.3 Glove design

Because the prototype is limited for measuring the movement of the wrist, the design of fingerless gloves is adopted. The basic outline of fingerless gloves is obtained by drawing the designed cutting line with a marker pen on the hand wearing the nitrile examination glove, as shown in Figure 6-2. Next, the examination glove is cut along the cutting line with scissors, also the examination glove along the right edge of the palm to obtain the initial unfolded shape of the fingerless glove. Finally, two extensions fabric on the back of the hand are added.



Figure 6-2 Nitrile Examination Glove for drawing the fingerless glove shape on real hand.

Figure 6-3 shows a flat unfolded view of the glove. This glove design is based on the premise that it should as simple as possible. The extension of the fabric is used to wrap the prototype while a Velcro tape is used to fix it. The effect of wearing the glove is shown in Figure 6-4.

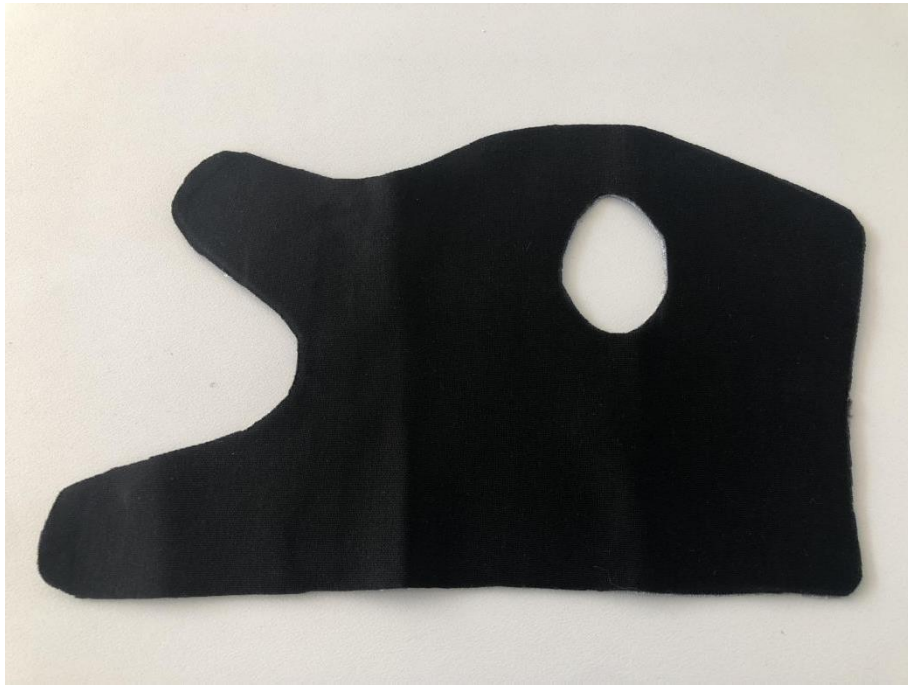


Figure 6-3 Flat unfolded view of the glove.



Figure 6-4 Fingerless glove without trace board.

6.4 Printing on textile

6.4.1 Preparation

Based on the shape of the prototype showed in the previous chapter, two different printing orientations of the prototype can be adopted:

- 1) The prototype is positioned upside-down, so only the covers of the Arduino Controller and the IMU are printed on the fabric and the rest of the prototype assembled afterwards. Figure 6-5 shows the placement orientation on the z-axis.



Figure 6-5 Z-axis orientation of covers contacted with the textile.

- 2) The entire prototype is directly printed on the fabric, this includes the conductive paths along with the isolation material, while the cover of the Arduino Controller and the IMU is mounted afterwards. Figure 6-6 shows the placement orientation on the z-axis.



Figure 6-6 Z-axis orientation of trace board contacted with the textile.

With the experiences of dual printing and prototype assembly learned from previous chapters, the strategy #2 is difficult, that is, print both material of the prototype directly on the textile. Therefore, strategy #1 is followed: the two covers are going to be created on the fabric while the trace board is fabricated in advance and assembled later. According to the specifications of the 3D model, the positions of the two covers on the bed are set and marked, in order to accurately print the prototype covers on the textile. Then, the positions of the

covers and gloves outline are underlined with tailor chalk on the textile. Next, it is necessary to apply double-sided adhesive tape to the borders of the printing bed and, finally, to cover the bed with the textile, applying pressure to the fabric to complete a good bonding to the tape. The final status is shown in Figure 6-7.

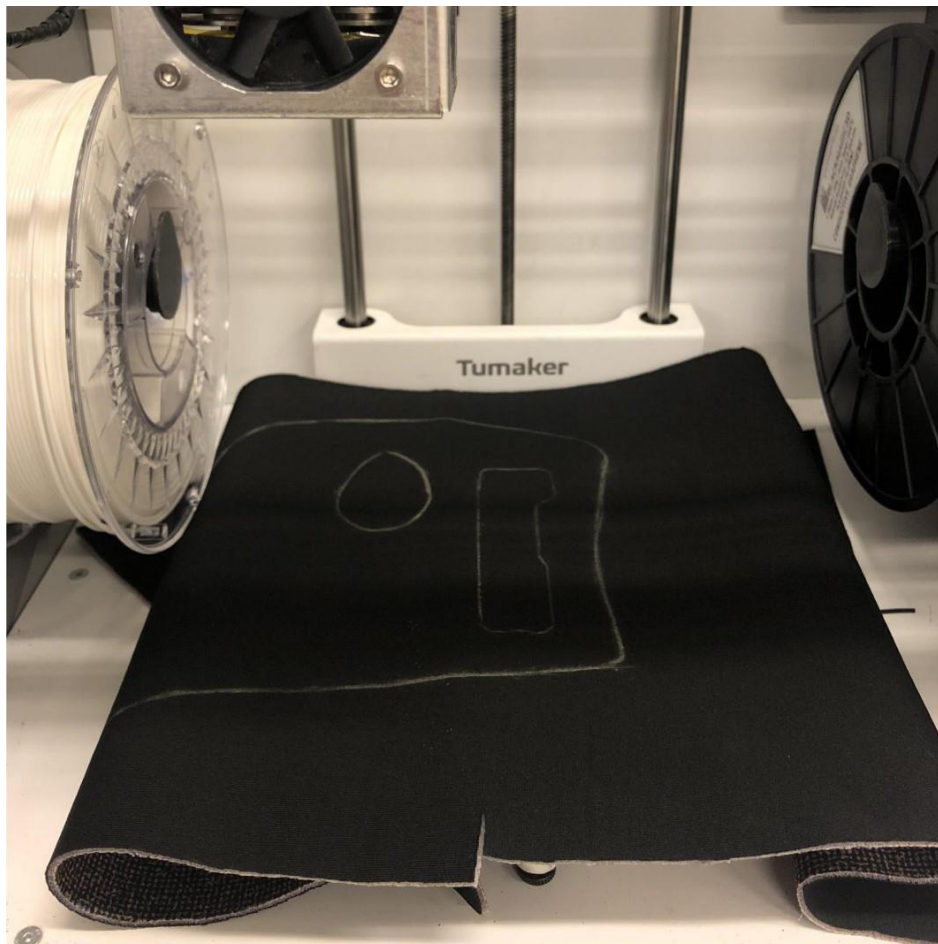


Figure 6-7 Textile clung to the bed before printing the base. The printing area is calibrated to the outline of the base.

6.4.2 Effects of bottom layers

Unlike smooth beds made of glass, printing on textiles has many uncertainties and the most critical one is the bottom layer printing. This is the basis for the later printing of subsequent layers to get high-quality objects. Many studies have shown that the principle to 3D

print on the textile is to substantially melt the polymer into the fabric, thereby forming a physical adhesion called "form-locking connection" [139,140]. This effect can be clearly seen under the microscope as Figure 6-8 shows.

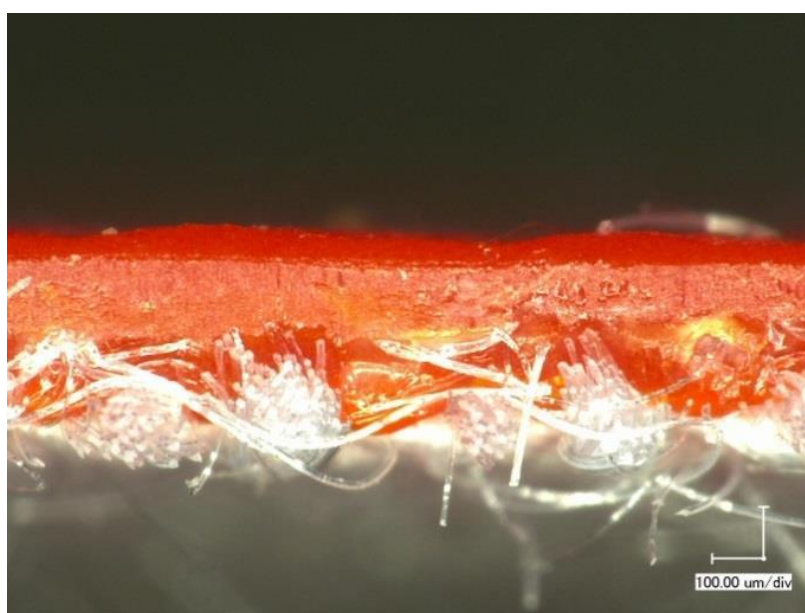


Figure 6-8 Cross-section of red PLA printed on the white polyester woven [143].

In order to ensure that the object is firmly printed on the fabric, it is necessary to print those bottom layer with the extruder compressing the fabric. The z-distance shall be less than the sum of the double-sided tape thickness and the textile thickness (2.4 mm). On the other hand, the z-distance also has a minimum value. Exceeding this threshold value will cause excessive extruding resistance, thus the nozzle will not be able to extrude the filament correctly. This minimum value is related to the density and arrangement of the textile surface [142]. In this study, the value of the z-distance is set to 1.4 mm.

Another factor that affects the bottom layer printing is the type of infill mode. It is obvious that although the textile is fixed with double-sided tape, the pressure of the nozzle and the travel path during printing still greatly affect the stability of the textile on the XY plane due to its high elasticity, since the nozzle tends to push/pull the fabric. For instance, in Figure 6-9, when the infill has a concentric fill shape,

the travel path will gently apply a continuously changing direction of thrust, which results in swirling folds.

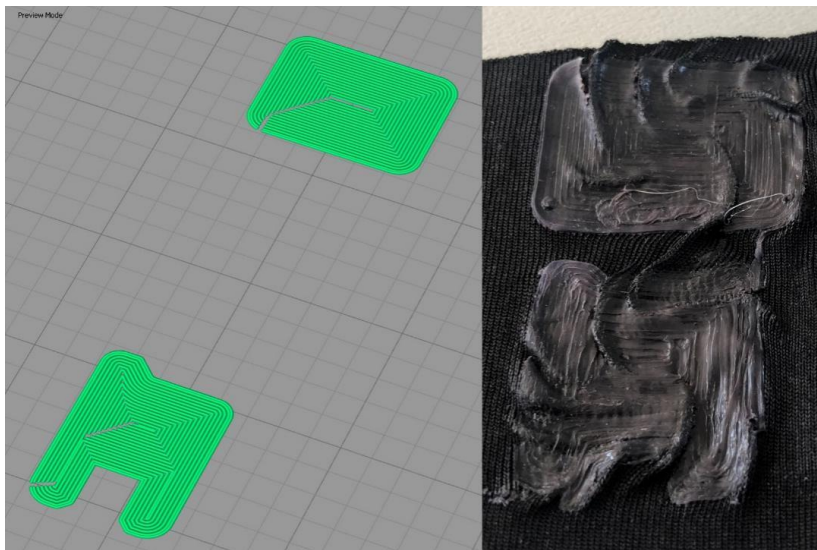


Figure 6-9 Ground layer printed with concentric fill shape.

But, in Figure 6-10, when the nozzle moves in a bevel mode, the thrust of the travel path has a small impact on the textile because it quickly turns backward when reaching the edge. This achieves a smooth print of the ground layer without folds.

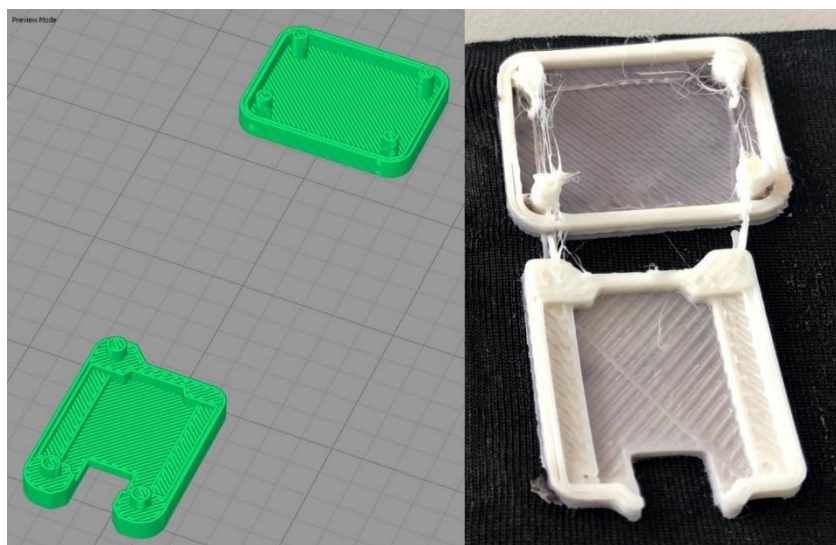


Figure 6-10 Ground layer printed with bevel mode.

In addition to the abovementioned points, the height of the bottom layer also determines the printing quality of the object. Because of the printing pressure exerted by the nozzle on the textile, the first few layers will not absolutely be well printed. As shown in Figure 6-11, the specimen on the far left shows the case where only a single bottom layer is printed, which is printed very unevenly due to the unstable fabric. As the thickness of the bottom layer gradually increases, the infill texture becomes regular until the rightmost specimen shows a clear layer stack.



Figure 6-11 The stability changes under different ground layer thickness. From left to right, the thicker ground layer provides more stable contact interface.

According to the physical characteristics of Neoprene, the total thickness of the bottom layers should be 1 mm to get accurate geometries above that height.

6.5 Prototype printing and verification

The print settings of the entire prototype follows Table 5-7 in Chapter 5. After printing the cover, the textile is removed from the bed, and cut down the gloves along the cutting line, and applied the Velcro tape at the bonding point. Figure 6-12 shows the printed covers on the glove, and trace board prototype mounted. The completed glove is shown in Figure 6-13.



Figure 6-12 Flat unfolded view of the glove with printed covers.



Figure 6-13 Complete glove with trace board prototype.

For verification purposes of the suitability of the textile, a simple experiment is performed to measure the deviation between the actual wrist bending angle and the prototype bending angle. The volunteer is asked to put on the glove and make two poses as shown in Figure 6-14.

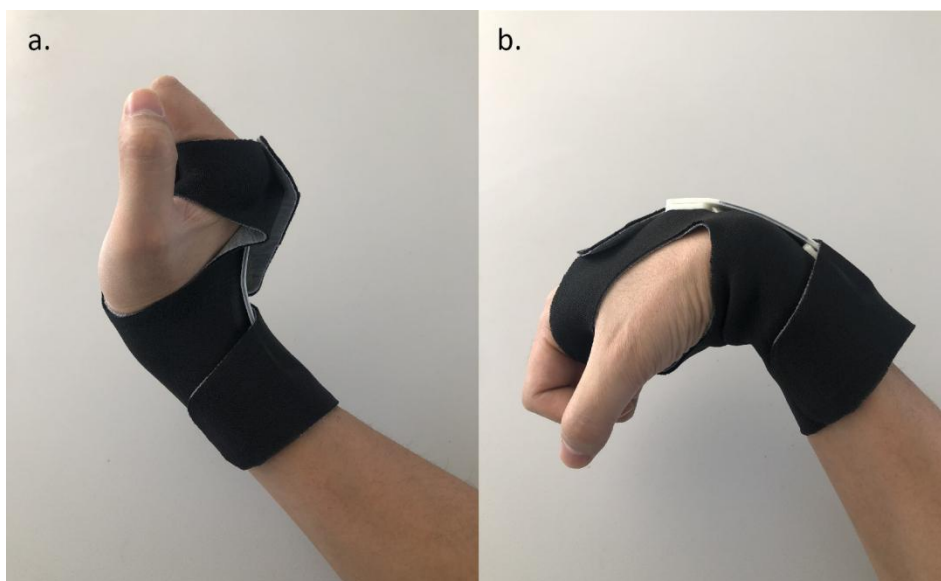


Figure 6-14 Glove bending test with: a) Wrist in extension; b) Wrist in flexion.

Firstly, the volunteer extends the wrist as much as possible and keep the pose. A second volunteer use a goniometer to record the angle between the back surface of the hand and the upper surface of the forearm (actual angle). In the meantime, the angle between the IMU sensor's plane and the Beetle chip's plane is recorded (Chip angle). Secondly, the volunteer flexes the wrist as much as possible and hold the pose. Following the same way, another two angles are obtained. The experimental results are shown in Table 6-2.

Table 6-2 Results of the Bending angles.

<i>Angles (deg)</i>	<i>Extension</i>	<i>Flexion</i>
<i>Chip angle</i>	<i>128°</i>	<i>-141°</i>
<i>Actual angle</i>	<i>around 113°</i>	<i>around -114°</i>

6.6 Discussion

Several points remain worthy of further discussion. Regarding printing speed, although the experiments of Spahiu et al [143] show that printing speed and polymer flow have no significant effect on adhesion, according to actual experience, excessive nozzle movement speed will significantly reduce the print quality of the bottom layer and cause folding problems on the textile. This becomes more apparent in the extruder path planning when printing complex objects. On the other hand, it is necessary printing the bottom layers with a certain pressure. However, when printing a precise part, the partial depression effect will affect its print quality, or even may not form the pre-set shape such as stacking or bridging. One method to solve this problem is to artificially add an interruption operation after finishing printing the ground layer, and restore the z-distance to the sum of the thickness of the double-sided tape and the natural thickness of the textile, so as to release the pressure and return to the normal printing process. This work will be further implemented in the future line.

Moreover, several drawbacks that are not good for measuring hand will be discussed. Since the internal traces of the prototype are printed with rigid Black Magic 3D, the rebound resistance is greater than the flexible filament under the same size. This will cause the base

to push the textile when the wrist is extending. The thrust is generated to make the textile folded, as shown in Figure 6-15.a While the wrist is flexing, the base will generate a vertical tension to pull up the textile, which causes a certain gap between the textile on the end parts of the prototype and the skin surface, as shown in Figure 6-15.b Because of this rebound tendency, both situations make the measured bending angle flatter than the actual wrist angle (the chip angles in Table 6-2 are closer to 180 degrees compare to actual angles). Considering that the essential cause of this effect is that the rebound force is not sufficiently constrained, it can be improved in a combination of three possible ways in the future work:

1. Counteract the effect of the rebound force by externally applying downward pressure. This can be achieved in future iterative designs of gloves by adding two adjustable bands to fasten the gloves at both ends of the prototype.
2. Increase the contact area between the polymer and the textile, use the elasticity of the textile to offset the rebound force of trace board. That means, instead of partly making the base contacted with the textile, the trace board will be printed directly on the textile (Strategy#2).

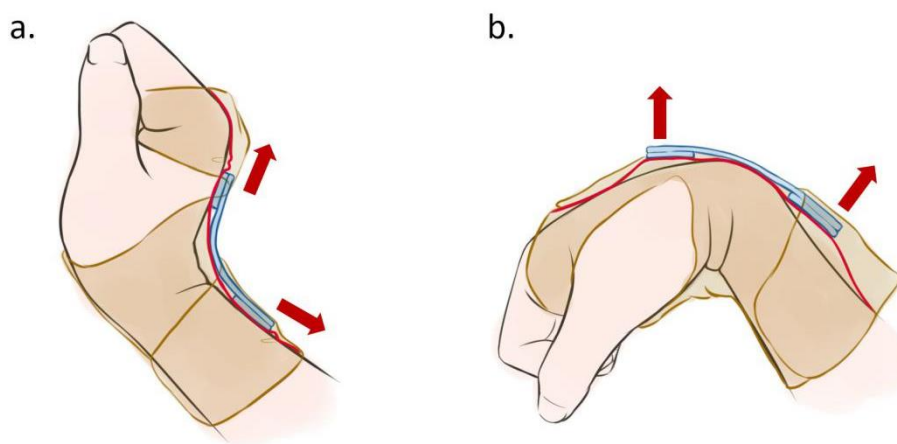


Figure 6-15 Rebound resistance impact to the chip angle: a) trace board push the textile to generate folds; b) trace board pull the textile to generate gaps. Red line shows the inner layer of the textile.

Additionally, this study on the prototype only focuses on the wrist part. Taking into account the narrower finger parts, the trace length will be shorter. The rebound resistance will have a greater impact on the measured results. As for the application of ergonomic measurement on the wrist region, this wearable prototype is able to complete the identification and monitoring repetitive wrist extension and flexion movements. However, it has certain errors in the identification and monitoring of the wrist extreme range of motion. There is still a certain gap to the standard of accurate measuring instruments, and the prototype needs to be further optimized and improved.

6.7 Conclusions

This chapter conducts a preliminary study of 3D printing on textiles. Many studies believe that the formation of a form-locking connection is an essential element for achieving strong adhesion. This can be implemented by adjusting the z-distance and the temperature of the nozzle and bed. The viscosity of the melted flexible polymer is high than the rigid PLA and ABS, which can infiltrate into the fabric fibers easier under the same conditions. In order to prevent the printing task from being suspended by folding error, ground layer infill is selected to bevel mode. In this study, the ground layer thickness is set to 1 mm and the z-distance is 1.4 mm. For the nozzle and bed temperatures, those presented in Chapter 5 are used. A simple experiment has demonstrated that the rebound resistance of the trace board prototype has a certain impact on the measurement of the actual wrist joint angle, which needs to be improved in many aspects.

Chapter 7:

Conclusions and future research lines

This part summarises the contributions made by this thesis and proposals for further research in the future are put forward.

7.1 Conclusions

This thesis project has provided a comprehensive methodology that is suitable for assessing MSDs risk exposure to the hand region in the actual production environment of workers. Through the integration of IMU technology and AM technology, economical and practical rapid functional wearables are implemented in an initial stage.

Specifically, this research project has produced a series of contributions to three topics: 1) evaluation for assessing ergonomic measurement methods concerning MSDs exposure levels, 2) research on hand motion capture methods based on IMU, and 3) study of

wearable smart devices based on Additive Manufacturing technology. The main contributions are presented in the following paragraphs.

1. With respect to the ergonomic measurement method:
 - MSDs are regarded as a major occupational healthcare problem in the automotive manufacturing industry. However, the importance of the hand region is understated in terms of MSDs exposure risks and their consequences in most of the epidemiology studies. The design of measurement devices for hands is a challenge due to the range of movement, the skeletal complexity and limited space in the fingers and the palm.
 - Seven prevailing ergonomic assessments were evaluated based on a customised questionnaire developed *ad hoc* and with the help of expert interviews. The results indicated that self-reports and expert observations (ART Tools, RULA/REBA) do not meet the requirement for an objective and accurate analysis, productivity guarantee, and even real-time monitoring. Moreover, some types of the direct measurements are hard to apply for tracking finger movements in the real workplace, due to the factors of sight occlusions (OES), data drift (ACC), unreasonable size (EM, OES, BA), and short duration (ACC), etc. Because of the advantages of low-cost, wearable scale, accuracy, and high popularity, IMU was found to be the most suitable measurement technology for this study although it can be affected by surrounding metal infrastructures.

2. With respect to the ergonomic measurement method:
 - A low-cost IMU-based motion capturing prototype was implemented. To be more specific, a set of quaternion-based algorithms for processing and expressing real-time rotation of multiple nodes, a data acquisition program and the packet sending program in Arduino were implemented. The results can be stored in a MicroSD card or plotted into a dynamic 3D model. The specific joint angle of the index finger and thumb was measured by using a custom gesture

standard, and the results indicated that the mean difference between the values measured physically by participants with a goniometer and those obtained virtually with the IMU system is 2.44° . The cost of the prototype was estimated at 225 EUR in total including seven IMU sensors for two fingers. The prototype has the same accuracy level but is cheaper than the commercial products (e.g. Xsens MVN costs around 12,000 EUR, and Vicon costs 55,000 EUR).

3. With respect to the wearable smart devices based on Additive Manufacturing technology:

- The volume resistivity of several brands of conductive filaments was studied considering different print settings. According to the resistivity results and actual operating performance, a Black Magic 3D Conductive Graphene PLA filament was most suitable for electrically creating conductive paths to connect the different electronics of the wearable. A set of experiments proved that the 'Printing temperature' is not critical to the resistivity of Black Magic 3D at the range of safety printing temperature, while 'Printing speed' significantly influences the resistivity, namely the lowest resistance value is obtained for higher speeds. Regarding the layer height, it was found that 0.2 mm has a relatively low resistance.
- A methodology that significantly reduces the cross-contamination in dual-material low-cost extrusion printing was developed. Several conductive paths were created to connect an IMU and an Arduino board. At the design level, an air gap to separate adjacent conductive paths was adopted as an interval to avoid most of the short circuit. At the print setting level, a set of reference printing parameters is provided and explained in detail. At the manufacturing level, a procedure for greatly reducing the stringing issue on the object's surface by shifting to the

resting point and exchanging the nozzle temperature alternately when switching the nozzles is utilised.

- In contrast to prototypes found in the literature, where electrically conductive paths were used with passive actuators (LED lights) or sensors (Force/strain gauges), a functional prototype that connects an active sensor (IMU) and an Arduino-based microcontroller was developed.

7.2 Future work

As a continuation of the work proposed in this thesis project, several possible future research lines are presented:

1. Concerning the ergonomic measurement methods assessment:
 - In the present investigation, the questionnaire designed and the interviews were carried out and analysed with the help of three ergonomic experts. This study can be further extended to a larger group of professionals or students to have more consensus on the selection of the ergonomic method.
 - The questionnaire summarises seven common ergonomic measurement methods. The selection of these methods is based on a comprehensive consideration from multiple reviewing studies covering the three major categories of ergonomic measurement methods, including "self-reporting", "observation evaluation", and "direct measurement", and the methods are frequently mentioned or used. Nevertheless, other measurement methods exist and they can also be evaluated by those experts to strengthen the selection of the IMU as the best solution for the current wearables.
 - This study focused on MSDs risk assessment of the hand. Similarly, according to a comparative study of the prevalence of MSDs, the approach of AM with functional materials (electrically) developed in this project can be extended, when developing wearables, to other high-risk body regions, such as the lower back or neck.
2. Relative to the hand motion capture methods:

-
- Due to some constraints during the prototype verification phase, the goniometer used in the control group was not sufficient to fully represent other types of measurement equipment. Therefore, it is necessary to involve measurement technology such as OES to completely guarantee the reliability of the control experiment results in future work.
 - Expanding the number of sensors to achieve the 16 nodes of the entire hand (including the wrist), building a more complex hardware framework and ensuring the orderly transmission of data can be other future lines of research. This will provide all aspects of the movement details of each finger, thereby extending the motion capture technology to the hand, which is the smallest and most delicate body part.
3. Regarding the fabrication of wearable smart devices:
- Since the volume resistivity of the material is the decisive factor for the aspect ratio of the trace, the design size of the trace board represents a considerable constraint. Although it has been proved through research that the existing conductive filament can be used as a conductor to replace the function of traditional copper wires to a certain extent, it still cannot fully meet the high-density and long-distance trace layout. The manufacturing 3D-Graphene monolith with high mechanical and electrical performance has become an urgent issue considering their potential applications in electronics fields [98]. Therefore, continuing to find and develop conductive 3D printing materials with lower volume resistivity is one of the main necessities to continue developing this approach. Several new materials like Electrifi can be used for future tests.
 - The current method of installing metal pins is a manual operation, which still results in considerable error in contact resistivity. Automating the drilling operations to improve accuracy will also be one of the future tasks.
 - Considering that the function of this device is to repeatedly and accurately measure the range and frequency of human

joint movement in actual production, it is equally important to evaluate the feasibility and durability of the AM strategy, as well as how metal interference can affect the measurements in the real workplace.

For dual-material printed circuit traces, the scalability of the device is also one of the topics that is worthy of attention. Apart from being able to successfully connect IMU sensors, the connection of other input/output devices is also worth applying to the printing test, such as the connection of the MicroSD card module to the micro-controller. Although technically possible, the main limitation here is to find a material with low resistivity values.

Appendix A: Code library: Adafruit_BNO055.cpp

This appendix shows the internal code of BNO055 library that have not been presented in the first study of Chapter 4. The underlined code is the part has been modified for this study.

```
1 *****
2   This is a library for the BNO055 orientation sensor
3
4   Designed specifically to work with the Adafruit BNO055 Breakout.
5
6   Pick one up today in the adafruit shop!
7   -----> http://www.adafruit.com/products
8
9   These sensors use I2C to communicate, 2 pins are required to
10  interface.
11
12  Adafruit invests time and resources providing this open source code,
13  please support Adafruit and open-source hardware by purchasing
14  products
15  from Adafruit!
16
17  Written by KTOWN for Adafruit Industries.
18
19  MIT license, all text above must be included in any redistribution
20
21  *****
22  *****/
23
24  #if ARDUINO >= 100
25  #include "Arduino.h"
26  #else
27  #include "WProgram.h"
28  #endif
29
30  #include <math.h>
31  #include <limits.h>
32
```

```
33 #include "Adafruit_BNO055.h"
34
35 /*****
36 *****/
37 CONSTRUCTOR
38
39 *****/
40 *****/
41
42 /*****
43 *****/
44 /*!
45 @brief Instantiates a new Adafruit_BNO055 class
46 */
47 /*****
48 *****/
49 Adafruit_BNO055::Adafruit_BNO055(int32_t sensorID, uint8_t
50 address)
51 {
52   _sensorID = sensorID;
53   _address = address;
54 }
55
56 /*****
57 *****/
58 PUBLIC FUNCTIONS
59
60 *****/
61 *****/
62
63 /*****
64 *****/
65 /*!
66 @brief Sets up the HW
67 */
68 /*****
69 *****/
70 bool Adafruit_BNO055::begin(adafruit_bno055_opmode_t mode)
71 {
72   /* Enable I2C */
73   Wire.begin();
74
75   // BNO055 clock stretches for 500us or more!
```

```
76 #ifndef ESP8266
77   Wire.setClockStretchLimit(1000); // Allow for 1000us of clock
78   stretching
79 #endif
80
81   /* Make sure we have the right device */
82   uint8_t id = read8(BNO055_CHIP_ID_ADDR);
83   if(id != BNO055_ID)
84   {
85     delay(1000); // hold on for boot
86     id = read8(BNO055_CHIP_ID_ADDR);
87     if(id != BNO055_ID) {
88       return false; // still not? ok bail
89     }
90   }
91
92   /* Switch to config mode (just in case since this is the default) */
93   setMode(OPERATION_MODE_CONFIG);
94
95   /* Reset */
96   write8(BNO055_SYS_TRIGGER_ADDR, 0x20);
97   while (read8(BNO055_CHIP_ID_ADDR) != BNO055_ID)
98   {
99     delay(10);
100  }
101  delay(50);
102
103  /* Set to normal power mode */
104  write8(BNO055_PWR_MODE_ADDR, POWER_MODE_NORMAL);
105  delay(10);
106
107  write8(BNO055_PAGE_ID_ADDR, 0);
108
109  /* Set the output units */
110  /*
111  uint8_t unitsel = (0 << 7) | // Orientation = Android
112                  (0 << 4) | // Temperature = Celsius
113                  (0 << 2) | // Euler = Degrees
114                  (1 << 1) | // Gyro = Rads
115                  (0 << 0); // Accelerometer = m/s^2
116  write8(BNO055_UNIT_SEL_ADDR, unitsel);
117  */
118
```

```

119  /* Configure axis mapping (see section 3.4) */
120  /*
121  write8(BNO055_AXIS_MAP_CONFIG_ADDR,
122  REMAP_CONFIG_P2); // P0-P7, Default is P1
123  delay(10);
124  write8(BNO055_AXIS_MAP_SIGN_ADDR, REMAP_SIGN_P2); //
125  P0-P7, Default is P1
126  delay(10);
127  */
128
129  write8(BNO055_SYS_TRIGGER_ADDR, 0x0);
130  delay(10);
131  /* Set the requested operating mode (see section 3.3) */
132  setMode(mode);
133  delay(20);
134
135  return true;
136  }
137
138  *****
139  *****
140  /*!
141  @brief Remaps axis and sign
142  */
143  *****
144  *****
145  byte Adafruit_BNO055::setAxisP(void)
146  {
147  setMode(OPERATION_MODE_CONFIG);
148  delay(30);
149  write8(BNO055_AXIS_MAP_CONFIG_ADDR, 0x21);
150  write8(BNO055_AXIS_MAP_SIGN_ADDR, 0x02);
151  delay(30);
152  byte axis = read8(BNO055_AXIS_MAP_CONFIG_ADDR);
153
154  setMode(OPERATION_MODE_NDOF);
155  delay(30);
156  return axis;
157  }
158
159
160

```

```
161 /*****
162 *****/
163 /*!
164  @brief Puts the chip in the specified operating mode
165  */
166 /*****
167 *****/
168 void Adafruit_BNO055::setMode(adafruit_bno055_opmode_t mode)
169 {
170     _mode = mode;
171     write8(BNO055_OPR_MODE_ADDR, _mode);
172     delay(30);
173 }
174
175 /*****
176 *****/
177 /*!
178  @brief Use the external 32.768KHz crystal
179  */
180 /*****
181 *****/
182 void Adafruit_BNO055::setExtCrystalUse(boolean usextal)
183 {
184     adafruit_bno055_opmode_t modeback = _mode;
185
186     /* Switch to config mode (just in case since this is the default) */
187     setMode(OPERATION_MODE_CONFIG);
188     delay(25);
189     write8(BNO055_PAGE_ID_ADDR, 0);
190     if (usextal) {
191         write8(BNO055_SYS_TRIGGER_ADDR, 0x80);
192     } else {
193         write8(BNO055_SYS_TRIGGER_ADDR, 0x00);
194     }
195     delay(10);
196     /* Set the requested operating mode (see section 3.3) */
197     setMode(modeback);
198     delay(20);
199 }
200
201
202 /*****
203 *****/
```

```
204  /*!  
205     @brief Gets the latest system status info  
206  */  
207  /*****  
208  *****/  
209  void Adafruit_BNO055::getSystemStatus(uint8_t *system_status,  
210  uint8_t *self_test_result, uint8_t *system_error)  
211  {  
212     write8(BNO055_PAGE_ID_ADDR, 0);  
213  
214     /* System Status (see section 4.3.58)  
215     -----  
216     0 = Idle  
217     1 = System Error  
218     2 = Initializing Peripherals  
219     3 = System Initialization  
220     4 = Executing Self-Test  
221     5 = Sensor fusion algorithm running  
222     6 = System running without fusion algorithms */  
223  
224     if (system_status != 0)  
225         *system_status = read8(BNO055_SYS_STAT_ADDR);  
226  
227     /* Self Test Results (see section )  
228     -----  
229     1 = test passed, 0 = test failed  
230  
231     Bit 0 = Accelerometer self test  
232     Bit 1 = Magnetometer self test  
233     Bit 2 = Gyroscope self test  
234     Bit 3 = MCU self test  
235  
236     0x0F = all good! */  
237  
238     if (self_test_result != 0)  
239         *self_test_result = read8(BNO055_SELFTEST_RESULT_ADDR);  
240  
241     /* System Error (see section 4.3.59)  
242     -----  
243     0 = No error  
244     1 = Peripheral initialization error  
245     2 = System initialization error  
246     3 = Self test result failed
```

```
247     4 = Register map value out of range
248     5 = Register map address out of range
249     6 = Register map write error
250     7 = BNO low power mode not available for selected operation
251 mode
252     8 = Accelerometer power mode not available
253     9 = Fusion algorithm configuration error
254     A = Sensor configuration error */
255
256 if (system_error != 0)
257     *system_error = read8(BNO055_SYS_ERR_ADDR);
258
259 delay(200);
260 }
261
262 /*****
263 *****/
264 /*!
265  @brief Gets the chip revision numbers
266  */
267 /*****
268 *****/
269 void Adafruit_BNO055::getRevInfo(adafruit_bno055_rev_info_t* info)
270 {
271     uint8_t a, b;
272
273     memset(info, 0, sizeof(adafruit_bno055_rev_info_t));
274
275     /* Check the accelerometer revision */
276     info->accel_rev = read8(BNO055_ACCEL_REV_ID_ADDR);
277
278     /* Check the magnetometer revision */
279     info->mag_rev = read8(BNO055_MAG_REV_ID_ADDR);
280
281     /* Check the gyroscope revision */
282     info->gyro_rev = read8(BNO055_GYRO_REV_ID_ADDR);
283
284     /* Check the SW revision */
285     info->bl_rev = read8(BNO055_BL_REV_ID_ADDR);
286
287     a = read8(BNO055_SW_REV_ID_LSB_ADDR);
288     b = read8(BNO055_SW_REV_ID_MSB_ADDR);
289     info->sw_rev = (((uint16_t)b) << 8) | ((uint16_t)a);
```

```
290 }
291
292 /*****
293 *****/
294 /*!
295  @brief Gets current calibration state. Each value should be a
296  uint8_t
297  pointer and it will be set to 0 if not calibrated and 3 if
298  fully calibrated.
299  */
300 /*****
301 *****/
302 void Adafruit_BNO055::getCalibration(uint8_t* sys, uint8_t* gyro,
303 uint8_t* accel, uint8_t* mag) {
304     uint8_t calData = read8(BNO055_CALIB_STAT_ADDR);
305     if (sys != NULL) {
306         *sys = (calData >> 6) & 0x03;
307     }
308     if (gyro != NULL) {
309         *gyro = (calData >> 4) & 0x03;
310     }
311     if (accel != NULL) {
312         *accel = (calData >> 2) & 0x03;
313     }
314     if (mag != NULL) {
315         *mag = calData & 0x03;
316     }
317 }
318
319 /*****
320 *****/
321 /*!
322  @brief Gets the temperature in degrees celsius
323  */
324 /*****
325 *****/
326 int8_t Adafruit_BNO055::getTemp(void)
327 {
328     int8_t temp = (int8_t)(read8(BNO055_TEMP_ADDR));
329     return temp;
330 }
331
```



```
332 /*****
333 *****/
334 /*!
335  @brief Gets a vector reading from the specified source
336  */
337 /*****
338 *****/
339 imu::Vector<3> Adafruit_BNO055::getVector(adafruit_vector_type_t
340 vector_type)
341 {
342     imu::Vector<3> xyz;
343     uint8_t buffer[6];
344     memset (buffer, 0, 6);
345
346     int16_t x, y, z;
347     x = y = z = 0;
348
349     /* Read vector data (6 bytes) */
350     readLen((adafruit_bno055_reg_t)vector_type, buffer, 6);
351
352     x = ((int16_t)buffer[0]) | (((int16_t)buffer[1]) << 8);
353     y = ((int16_t)buffer[2]) | (((int16_t)buffer[3]) << 8);
354     z = ((int16_t)buffer[4]) | (((int16_t)buffer[5]) << 8);
355
356     /* Convert the value to an appropriate range (section 3.6.4) */
357     /* and assign the value to the Vector type */
358     switch(vector_type)
359     {
360     case VECTOR_MAGNETOMETER:
361         /* 1uT = 16 LSB */
362         xyz[0] = ((double)x)/16.0;
363         xyz[1] = ((double)y)/16.0;
364         xyz[2] = ((double)z)/16.0;
365         break;
366     case VECTOR_GYROSCOPE:
367         /* 1dps = 16 LSB */
368         xyz[0] = ((double)x)/16.0;
369         xyz[1] = ((double)y)/16.0;
370         xyz[2] = ((double)z)/16.0;
371         break;
372     case VECTOR_EULER:
373         /* 1 degree = 16 LSB */
374         xyz[0] = ((double)x)/16.0;
```

```
375     xyz[1] = ((double)y)/16.0;
376     xyz[2] = ((double)z)/16.0;
377     break;
378     case VECTOR_ACCELEROMETER:
379     case VECTOR_LINEARACCEL:
380     case VECTOR_GRAVITY:
381         /* 1m/s^2 = 100 LSB */
382         xyz[0] = ((double)x)/100.0;
383         xyz[1] = ((double)y)/100.0;
384         xyz[2] = ((double)z)/100.0;
385         break;
386     }
387
388     return xyz;
389 }
390
391 /*****
392 *****/
393 /*!
394 @brief Gets a quaternion reading from the specified source
395 */
396 /*****
397 *****/
398 imu::Quaternion Adafruit_BNO055::getQuat(void)
399 {
400     uint8_t buffer[8];
401     memset (buffer, 0, 8);
402
403     int16_t x, y, z, w;
404     x = y = z = w = 0;
405
406     /* Read quat data (8 bytes) */
407     readLen(BNO055_QUATERNION_DATA_W_LSB_ADDR, buffer,
408     8);
409     w = (((uint16_t)buffer[1]) << 8) | ((uint16_t)buffer[0]);
410     x = (((uint16_t)buffer[3]) << 8) | ((uint16_t)buffer[2]);
411     y = (((uint16_t)buffer[5]) << 8) | ((uint16_t)buffer[4]);
412     z = (((uint16_t)buffer[7]) << 8) | ((uint16_t)buffer[6]);
413
414     /* Assign to Quaternion */
415     /* See http://ae-
416     bst.resource.bosch.com/media/products/dokumente/bno055/BST\_BNO
417     055\_DS000\_12~1.pdf
```

```
418     3.6.5.5 Orientation (Quaternion) */
419     const double scale = (1.0 / (1<<14));
420     imu::Quaternion quat(scale * w, scale * x, scale * y, scale * z);
421     return quat;
422 }
423
424 /*****
425 *****/
426 /*!
427  @brief Provides the sensor_t data for this sensor
428 */
429 /*****
430 *****/
431 void Adafruit_BNO055::getSensor(sensor_t *sensor)
432 {
433     /* Clear the sensor_t object */
434     memset(sensor, 0, sizeof(sensor_t));
435
436     /* Insert the sensor name in the fixed length char array */
437     strncpy (sensor->name, "BNO055", sizeof(sensor->name) - 1);
438     sensor->name[sizeof(sensor->name)- 1] = 0;
439     sensor->version    = 1;
440     sensor->sensor_id  = _sensorID;
441     sensor->type       = SENSOR_TYPE_ORIENTATION;
442     sensor->min_delay  = 0;
443     sensor->max_value  = 0.0F;
444     sensor->min_value  = 0.0F;
445     sensor->resolution = 0.01F;
446 }
447
448 /*****
449 *****/
450 /*!
451  @brief Reads the sensor and returns the data as a sensors_event_t
452 */
453 /*****
454 *****/
455 bool Adafruit_BNO055::getEvent(sensors_event_t *event)
456 {
457     /* Clear the event */
458     memset(event, 0, sizeof(sensors_event_t));
459
460     event->version = sizeof(sensors_event_t);
```

```
461     event->sensor_id = _sensorID;
462     event->type      = SENSOR_TYPE_ORIENTATION;
463     event->timestamp = millis();
464
465     /* Get a Euler angle sample for orientation */
466     imu::Vector<3> euler =
467     getVector(Adafruit_BNO055::VECTOR_EULER);
468     event->orientation.x = euler.x();
469     event->orientation.y = euler.y();
470     event->orientation.z = euler.z();
471
472     return true;
473 }
474
475 /*****
476 *****/
477 /*!
478 @brief Reads the sensor's offset registers into a byte array
479 */
480 /*****
481 *****/
482 bool Adafruit_BNO055::getSensorOffsets(uint8_t* calibData)
483 {
484     if (isFullyCalibrated())
485     {
486         adafruit_bno055_opmode_t lastMode = _mode;
487         setMode(OPERATION_MODE_CONFIG);
488
489         readLen(ACCEL_OFFSET_X_LSB_ADDR, calibData,
490 NUM_BNO055_OFFSET_REGISTERS);
491
492         setMode(lastMode);
493         return true;
494     }
495     return false;
496 }
497
498 /*****
499 *****/
500 /*!
501 @brief Reads the sensor's offset registers into an offset struct
502 */
```

```
503 /*****
504 *****/
505 bool Adafruit_BNO055::getSensorOffsets(adafruit_bno055_offsets_t
506 &offsets_type)
507 {
508     if (isFullyCalibrated())
509     {
510         adafruit_bno055_opmode_t lastMode = _mode;
511         setMode(OPERATION_MODE_CONFIG);
512         delay(25);
513
514         offsets_type.accel_offset_x =
515 (read8(ACCEL_OFFSET_X_MSB_ADDR) << 8) |
516 (read8(ACCEL_OFFSET_X_LSB_ADDR));
517         offsets_type.accel_offset_y =
518 (read8(ACCEL_OFFSET_Y_MSB_ADDR) << 8) |
519 (read8(ACCEL_OFFSET_Y_LSB_ADDR));
520         offsets_type.accel_offset_z =
521 (read8(ACCEL_OFFSET_Z_MSB_ADDR) << 8) |
522 (read8(ACCEL_OFFSET_Z_LSB_ADDR));
523
524         offsets_type.gyro_offset_x =
525 (read8(GYRO_OFFSET_X_MSB_ADDR) << 8) |
526 (read8(GYRO_OFFSET_X_LSB_ADDR));
527         offsets_type.gyro_offset_y =
528 (read8(GYRO_OFFSET_Y_MSB_ADDR) << 8) |
529 (read8(GYRO_OFFSET_Y_LSB_ADDR));
530         offsets_type.gyro_offset_z =
531 (read8(GYRO_OFFSET_Z_MSB_ADDR) << 8) |
532 (read8(GYRO_OFFSET_Z_LSB_ADDR));
533
534         offsets_type.mag_offset_x =
535 (read8(MAG_OFFSET_X_MSB_ADDR) << 8) |
536 (read8(MAG_OFFSET_X_LSB_ADDR));
537         offsets_type.mag_offset_y =
538 (read8(MAG_OFFSET_Y_MSB_ADDR) << 8) |
539 (read8(MAG_OFFSET_Y_LSB_ADDR));
540         offsets_type.mag_offset_z =
541 (read8(MAG_OFFSET_Z_MSB_ADDR) << 8) |
542 (read8(MAG_OFFSET_Z_LSB_ADDR));
543
```

```
544     offsets_type.accel_radius =
545 (read8(ACCEL_RADIUS_MSB_ADDR) << 8) |
546 (read8(ACCEL_RADIUS_LSB_ADDR));
547     offsets_type.mag_radius = (read8(MAG_RADIUS_MSB_ADDR)
548 << 8) | (read8(MAG_RADIUS_LSB_ADDR));
549
550     setMode(lastMode);
551     return true;
552 }
553 return false;
554 }
555
556
557 /*****
558 *****/
559 /*!
560 @brief Writes an array of calibration values to the sensor's offset
561 registers
562 */
563 /*****
564 *****/
565 void Adafruit_BNO055::setSensorOffsets(const uint8_t* calibData)
566 {
567     adafruit_bno055_opmode_t lastMode = _mode;
568     setMode(OPERATION_MODE_CONFIG);
569     delay(25);
570
571     /* A writeLen() would make this much cleaner */
572     write8(ACCEL_OFFSET_X_LSB_ADDR, calibData[0]);
573     write8(ACCEL_OFFSET_X_MSB_ADDR, calibData[1]);
574     write8(ACCEL_OFFSET_Y_LSB_ADDR, calibData[2]);
575     write8(ACCEL_OFFSET_Y_MSB_ADDR, calibData[3]);
576     write8(ACCEL_OFFSET_Z_LSB_ADDR, calibData[4]);
577     write8(ACCEL_OFFSET_Z_MSB_ADDR, calibData[5]);
578
579     write8(GYRO_OFFSET_X_LSB_ADDR, calibData[6]);
580     write8(GYRO_OFFSET_X_MSB_ADDR, calibData[7]);
581     write8(GYRO_OFFSET_Y_LSB_ADDR, calibData[8]);
582     write8(GYRO_OFFSET_Y_MSB_ADDR, calibData[9]);
583     write8(GYRO_OFFSET_Z_LSB_ADDR, calibData[10]);
584     write8(GYRO_OFFSET_Z_MSB_ADDR, calibData[11]);
585
586     write8(MAG_OFFSET_X_LSB_ADDR, calibData[12]);
```

```
587     write8(MAG_OFFSET_X_MSB_ADDR, calibData[13]);
588     write8(MAG_OFFSET_Y_LSB_ADDR, calibData[14]);
589     write8(MAG_OFFSET_Y_MSB_ADDR, calibData[15]);
590     write8(MAG_OFFSET_Z_LSB_ADDR, calibData[16]);
591     write8(MAG_OFFSET_Z_MSB_ADDR, calibData[17]);
592
593     write8(ACCEL_RADIUS_LSB_ADDR, calibData[18]);
594     write8(ACCEL_RADIUS_MSB_ADDR, calibData[19]);
595
596     write8(MAG_RADIUS_LSB_ADDR, calibData[20]);
597     write8(MAG_RADIUS_MSB_ADDR, calibData[21]);
598
599     setMode(lastMode);
600 }
601
602 /*****
603 *****/
604 /*!
605 @brief Writes to the sensor's offset registers from an offset struct
606 */
607 /*****
608 *****/
609 void Adafruit_BNO055::setSensorOffsets(const
610 adafruit_bno055_offsets_t &offsets_type)
611 {
612     adafruit_bno055_opmode_t lastMode = _mode;
613     setMode(OPERATION_MODE_CONFIG);
614     delay(25);
615
616     write8(ACCEL_OFFSET_X_LSB_ADDR,
617 (offsets_type.accel_offset_x) & 0xFF);
618     write8(ACCEL_OFFSET_X_MSB_ADDR,
619 (offsets_type.accel_offset_x >> 8) & 0xFF);
620     write8(ACCEL_OFFSET_Y_LSB_ADDR,
621 (offsets_type.accel_offset_y) & 0xFF);
622     write8(ACCEL_OFFSET_Y_MSB_ADDR,
623 (offsets_type.accel_offset_y >> 8) & 0xFF);
624     write8(ACCEL_OFFSET_Z_LSB_ADDR,
625 (offsets_type.accel_offset_z) & 0xFF);
626     write8(ACCEL_OFFSET_Z_MSB_ADDR,
627 (offsets_type.accel_offset_z >> 8) & 0xFF);
628
```

```
629     write8(GYRO_OFFSET_X_LSB_ADDR,
630 (offsets_type.gyro_offset_x) & 0xFF);
631     write8(GYRO_OFFSET_X_MSB_ADDR,
632 (offsets_type.gyro_offset_x >> 8) & 0xFF);
633     write8(GYRO_OFFSET_Y_LSB_ADDR,
634 (offsets_type.gyro_offset_y) & 0xFF);
635     write8(GYRO_OFFSET_Y_MSB_ADDR,
636 (offsets_type.gyro_offset_y >> 8) & 0xFF);
637     write8(GYRO_OFFSET_Z_LSB_ADDR, (offsets_type.gyro_offset_z)
638 & 0xFF);
639     write8(GYRO_OFFSET_Z_MSB_ADDR,
640 (offsets_type.gyro_offset_z >> 8) & 0xFF);
641
642     write8(MAG_OFFSET_X_LSB_ADDR, (offsets_type.mag_offset_x)
643 & 0xFF);
644     write8(MAG_OFFSET_X_MSB_ADDR,
645 (offsets_type.mag_offset_x >> 8) & 0xFF);
646     write8(MAG_OFFSET_Y_LSB_ADDR, (offsets_type.mag_offset_y)
647 & 0xFF);
648     write8(MAG_OFFSET_Y_MSB_ADDR,
649 (offsets_type.mag_offset_y >> 8) & 0xFF);
650     write8(MAG_OFFSET_Z_LSB_ADDR, (offsets_type.mag_offset_z)
651 & 0xFF);
652     write8(MAG_OFFSET_Z_MSB_ADDR,
653 (offsets_type.mag_offset_z >> 8) & 0xFF);
654
655     write8(ACCEL_RADIUS_LSB_ADDR, (offsets_type.accel_radius)
656 & 0xFF);
657     write8(ACCEL_RADIUS_MSB_ADDR,
658 (offsets_type.accel_radius >> 8) & 0xFF);
659
660     write8(MAG_RADIUS_LSB_ADDR, (offsets_type.mag_radius) &
661 0xFF);
662     write8(MAG_RADIUS_MSB_ADDR, (offsets_type.mag_radius >>
663 8) & 0xFF);
664
665     setMode(lastMode);
666 }
667
668 bool Adafruit_BNO055::isFullyCalibrated(void)
669 {
670     uint8_t system, gyro, accel, mag;
671     getCalibration(&system, &gyro, &accel, &mag);
```



```
672     if (system < 3 || gyro < 3 || accel < 3 || mag < 3)
673         return false;
674     return true;
675 }
676
677
678 /*****
679 *****/
680 PRIVATE FUNCTIONS
681
682 /*****
683 *****/
684
685 /*****
686 *****/
687 /*!
688  @brief Writes an 8 bit value over I2C
689 */
690 /*****
691 *****/
692 bool Adafruit_BNO055::write8(adafruit_bno055_reg_t reg, byte
693 value)
694 {
695     Wire.beginTransaction(_address);
696     #if ARDUINO >= 100
697         Wire.write((uint8_t)reg);
698         Wire.write((uint8_t)value);
699     #else
700         Wire.send(reg);
701         Wire.send(value);
702     #endif
703     Wire.endTransmission();
704
705     /* ToDo: Check for error! */
706     return true;
707 }
708
709 /*****
710 *****/
711 /*!
712  @brief Reads an 8 bit value over I2C
713 */
```

```
714 /*****
715 *****/
716 byte Adafruit_BNO055::read8(adafruit_bno055_reg_t reg )
717 {
718     byte value = 0;
719
720     Wire.beginTransmission(_address);
721     #if ARDUINO >= 100
722         Wire.write((uint8_t)reg);
723     #else
724         Wire.send(reg);
725     #endif
726     Wire.endTransmission();
727     Wire.requestFrom(_address, (byte)1);
728     #if ARDUINO >= 100
729         value = Wire.read();
730     #else
731         value = Wire.receive();
732     #endif
733
734     return value;
735 }
736
737 /*****
738 *****/
739 /*!
740  @brief Reads the specified number of bytes over I2C
741  */
742 /*****
743 *****/
744 bool Adafruit_BNO055::readLen(adafruit_bno055_reg_t reg, byte *
745 buffer, uint8_t len)
746 {
747     Wire.beginTransmission(_address);
748     #if ARDUINO >= 100
749         Wire.write((uint8_t)reg);
750     #else
751         Wire.send(reg);
752     #endif
753     Wire.endTransmission();
754     Wire.requestFrom(_address, (byte)len);
755
756     for (uint8_t i = 0; i < len; i++)
```

```
757     {
758     #if ARDUINO >= 100
759         buffer[i] = Wire.read();
760     #else
761         buffer[i] = Wire.receive();
762     #endif
763     }
764
765     /* ToDo: Check for errors! */
766     return true;
767 }
```


Appendix B: Code in Arduino IDE

This appendix shows the main code of Arduino IDE that have not been presented in the study of Chapter 4. Both real-time and SD card storage functions are included.

```
1  #include <Wire.h>
2  #include <Adafruit_Sensor.h> /*a core sensor library that helps
3  manage sensor readings.*/
4  #include <Adafruit_BNO055.h> /*begin controlling the motor chip*/
5  #include <utility/imumaths.h>
6  #include <SD.h>
7
8  #define BNO055_SAMPLERATE_DELAY_MS (100)
9  #define TCAADDR 0x70
10
11  File dataFile;
12  File countFile;
13
14  int trigger = 1;
15  uint32_t bnoNumber = 7;
16  int h = 0;
17  int i;
18  int j;
19  int k;
20  unsigned long tic;
21  unsigned long tac;
22  double timeperiod;
23  byte CntBuffer;
24  int Count = 0;
25  char FileName[13] = {};
26
27  Adafruit_BNO055 bno[ 7 ];
28  imu::Quaternion quat[ 7 ];
29
30  void tcaselect(uint8_t i) {
31      if (i > 7) return;
32      Wire.beginTransaction(TCAADDR);
```

```
33         Wire.write(1 << i);
34         Wire.endTransmission()
35     }
36
37 void setup(void)
38 {
39     Wire.begin()
40     Serial.begin(9600);
41     pinMode(10, OUTPUT);
42
43     if (!SD.begin(10))
44     {
45         Serial.println("initialization failed!");
46         return;
47     }
48     if(!SD.exists("Cnt.txt"))
49     {
50         countFile = SD.open("Cnt.txt",FILE_WRITE);
51         Count = 0;
52         countFile.print(Count);
53         countFile.close();
54     }
55     for (k = 0; k < bnoNumber; k++)
56     {
57         bno[k] = Adafruit_BNO055(k);
58     }
59     for (i = 0; i < bnoNumber; i++)
60     {
61         tcselect(i);
62         if(!bno[i].begin())
63         {
64             /* There was a problem detecting the BNO055 at
65             0x28 ... check your connections */
66             Serial.print("Oops, no BNO055 ");
67             Serial.print(i);
68             Serial.print(" detected ... Check your wiring or
69             I2C ADDR!");
70         }
71         else
72         {
73             bno[i].setAxisP();
74         }
75     }
```

```
76     delay(10);
77 }
78
79
80
81 void loop()
82 {
83     tic = micros();
84
85     if (Serial.available() && trigger == 1)
86     {
87         //Serial.parseInt();
88         countFile = SD.open("Cnt.txt");
89         if(countFile)
90         {
91             while (countFile.available())
92             {
93                 CntBuffer = countFile.read();
94                 if((h<4))
95                 {
96                     Count = Count*10 + (CntBuffer - '0');
97                     h++;
98                 }
99             }
100             countFile.close();
101         }
102
103         countFile = SD.open("Cnt.txt", O_TRUNC | O_WRITE);
104         if(countFile)
105         {
106             if(SD.exists("Cnt.txt") && Count >= 9999)
107             {
108                 Count = 0;
109                 sprintf(FileName, "D%04d.txt",Count);
110                 countFile.print(Count);
111             } else {
112                 Count++;
113                 sprintf(FileName, "D%04d.txt",Count);
114                 countFile.print(Count);
115             }
116             countFile.close();
117         }
118         Serial.println(FileName);
```

```
119   trigger = 0;
120   }
121
122   uint8_t system, gyro, accel, mag;
123
124   for (j = 0; j < bnoNumber; j++){
125     tcselect(j);
126     quat[ j ] = bno[ j ].getQuat();
127     system = gyro = accel = mag = 0;
128     bno[ j ].getCalibration(&system, &gyro, &accel, &mag);
129
130
131
132     Serial.print(timeperiod/1000000,4);
133     Serial.print(" ");
134     Serial.print(quat[ j ].w(), 4);
135     Serial.print(" ");
136     Serial.print(quat[ j ].x(), 4);
137     Serial.print(" ");
138     Serial.print(quat[ j ].y(), 4);
139     Serial.print(" ");
140     Serial.print(quat[ j ].z(), 4);
141
142     Serial.print(" ");
143     Serial.print(system, DEC);
144     Serial.print(" ");
145     Serial.print(gyro, DEC);
146     Serial.print(" ");
147     Serial.print(accel, DEC);
148     Serial.print(" ");
149     Serial.print(mag, DEC);
150     Serial.print(" ");
151     Serial.println(j);
152
153     dataFile = SD.open(FileName, FILE_WRITE);
154
155     if (dataFile) {
156       dataFile.print(timeperiod/1000000,4);
157       dataFile.print(" ");
158       dataFile.print(quat[ j ].w(), 4);
159       dataFile.print(" ");
160       dataFile.print(quat[ j ].x(), 4);
161       dataFile.print(" ");
```



```
162     dataFile.print(quat[ j ].y(), 4);
163     dataFile.print(", ");
164     dataFile.print(quat[ j ].z(), 4);
165
166     dataFile.print(", ");
167     dataFile.print(system, DEC);
168     dataFile.print(", ");
169     dataFile.print(gyro, DEC);
170     dataFile.print(", ");
171     dataFile.print(accel, DEC);
172     dataFile.print(", ");
173     dataFile.print(mag, DEC);
174     dataFile.print(", ");
175     dataFile.println(j);
176
177     dataFile.close();
178 }
179
180 }
181
182 delay(BNO055_SAMPLERATE_DELAY_MS);
183
184 tac = micros();
185 timeperiod = tac - tic;
186 }
```


Appendix C: Main Code in Matlab

This appendix shows the main code of Matlab that have not been presented in the study of Chapter 4. Both real-time and SD card storage functions are included.

```
1 % IMU data post-process and modeling:
2 %     A function to calculate and draw a real time cylinder-based
3 %     finger model using quaternion.
4 %
5 %
6 % Inputs:  sensor data - packaged from Arduino IDE.
7 %     i.g. "0.4422, 0.5445, 0.1777, -0.7150, 0.4009, 3, 3, 3, 3, 6"
8 %     The entire package includes ID from 0 to 6
9 %
10 %     SegmentLength - phalanx lengths measured in reality.
11 %
12 %     CompensationAngle - a compensation angle between
13 screen normal line and magnetic north
14 %
15 %
16 % Author:  Chuan Cao
17 % Date:    18 October 2019
18 % Contact: ccao@tecnun.es
19 % Univercity of Navarra-tecnun
20
21 clear
22 clc; close all;
23 %mcc -m Output2User06Feb.m DistalQuatMultiTransform.m
24 VectorAngle.m cylinder2P.m EndingDialog.m%
25
26 disp('Initializing...Please wait a moment');
27
28 %input preset#1%
29 s=serial('COM3');
30 set (s, 'BaudRate', 9600);
31 s.InputBufferSize = 1024;
32 s.OutputBufferSize = 1024;
```

```

33 fopen (s);
34
35 %input preset#2%
36 [files,Pathes,FileIndex] = uigetfile({'*.txt'; '*.*'},'Import data files');
37 fileTemp1 = 'tempOutput1.txt';
38 fileTemp2 = 'tempOutput2.txt';
39
40 [fid, error1] = fopen(files,'r');
41 [fidtemp1, error21]= fopen(fileTemp1,'w');
42 [fidtemp2, error22]= fopen(fileTemp2,'w');
43
44 formatSpec1 = '%s\t %s\t %3.2f\t %3.2f\t %3.2f\t\r\n';
45 formatSpec2 =
46 '%s\t %3.2f\t %3.2f\t %3.2f\t %3.2f\t %3.2f\t %3.2f\t\r\n';
47 AngleName = {'MCP_T2I', 'TMCP', 'TIP', 'IMCP', 'IPIP', 'IDIP', []};
48 FingerName = {'TMCP', 'TIP', 'TEP', 'IMCP', 'IPIP', 'IDIP',
49 'IEP'};      % TEP = Thumb endpoint; IEP = index endpoint %
50
51 if fid == -1
52     errormsg1 = [error1,' called <', files, '>'];
53     disp(errormsg1);
54     return;
55 elseif fidtemp1 == -1
56     errormsg21 = [error21,' called <', fileTemp1, '>'];
57     disp(errormsg21);
58     return;
59 elseif fidtemp2 == -1
60     errormsg22 = [error22,' called <', fileTemp2, '>'];
61     disp(errormsg22);
62     return;
63 end
64
65 SampleRate = 0.5;                                % Minimum
66 time period is 0.41 s %
67 i = 1;
68 SensorNumber = 7;
69 Timeperiod = 0;
70 Timepoint = 0;
71 Time = cell(7,1);
72 DataStore = zeros(7,10);
73 DataOutput = cell(7,7);
74 SegmentLength = [6.5, 4, 3, 8.5, 5, 3, 2.5];
75 Ra = 1;

```

```
76 n = 20;
77 OP = [0 0 0 0];
78 StandingPoint = [0 0 1 0];
79
80 answer = inputdlg('Enter compensation angle value (in degrees,
81 clockwise)','Compensation Angle');
82 CompensationAngle = str2double(answer{1});
83
84 global Offsetquat;
85
86 %offset compensation%
87 OffsetRad=deg2rad(CompensationAngle);
88 normVic = [0 0 0 1]/norm([0 0 0 1]);
89 wo=cos(OffsetRad/2);
90 xo=normVic(2)*sin(OffsetRad/2);
91 yo=normVic(3)*sin(OffsetRad/2);
92 zo=normVic(4)*sin(OffsetRad/2);
93
94 Offsetquat=[wo xo yo zo];
95
96 fprintf(fidtemp2,'%s\t %s\t %s\t %s\t %s\t %s\t %s\t %s\t\r\n','Time',
97 'MCP_T2I', 'TMCP', 'TIP', 'IMCP', 'IPIP', 'IDIP');
98
99 while ~feof(fid)
100
101     %receive data#%
102     for ii = 1:SensorNumber
103
104         %from txt file%
105         str = fgetl(fid);
106
107         %from serial port%
108         str=fscanf(s,'%s');
109
110         strStore = strsplit(str, ',');
111         IMUStore = str2double(strStore);
112
113         %store data for calculation%
114         DataStore(ii,:) = IMUStore;
115     end
116
117     %(Optional) display storing status%
```

```

118     disp(' timePrd      w      x      y      z      Sys      G      A
119 M      ID');
120     disp(DataStore);
121
122     %(Optional) display system status%
123     % disp(' Sys G A M');
124     % disp(DataStore(:,5:8));
125
126     % -----
127
128     %Time line counting%
129     Timeperiod = DataStore(1,1);
130     Timepoint = Timepoint + Timeperiod;
131     Time(:) = {datestr(Timepoint/86400, 'HH:MM:SS.FFF')};
132
133     %% -----CALCULATION SECTION-----
134     ----%
135
136     %convert rotation angle in quaternion to Euler form intuitively for
137     displaying%
138     PalmeulZYX = quat2eul(DataStore(4,2:5));
139     yawPalm = radtodeg(PalmeulZYX(1));
140     rollPalm = radtodeg(PalmeulZYX(2));
141     pitchPalm = radtodeg(PalmeulZYX(3));
142
143     %get the global coordinate of each endpoints%
144     LocalThumbSeg = OP;
145     for thumb = 1:3
146         [ThumbSeg, LocalThumbSeg] =
147         DistalQuatMultiTransform(DataStore(thumb,2:5), LocalThumbSeg,
148         SegmentLength(thumb));
149         DataStore(thumb,2:5) = ThumbSeg;
150     end
151
152     LocalFingerSeg = OP;
153     for finger = 1:4
154         [FingerSeg, LocalFingerSeg] =
155         DistalQuatMultiTransform(DataStore(finger+thumb,2:5),
156         LocalFingerSeg, SegmentLength(finger+thumb));
157         DataStore(finger+thumb,2:5) = FingerSeg;
158     end
159
160     %get each angle between two segments%

```

```

161     AngleTMCP2IMCP = VectorAngle(OP, DataStore(1,2:5), OP,
162 DataStore(4,2:5));
163     AngleTMCP = VectorAngle(OP, DataStore(1,2:5), DataStore(1,2:5),
164 DataStore(2,2:5));
165     AngleTIP = VectorAngle(DataStore(1,2:5), DataStore(2,2:5),
166 DataStore(2,2:5), DataStore(3,2:5));
167
168     AngleIMCP = VectorAngle(OP, DataStore(4,2:5), DataStore(4,2:5),
169 DataStore(5,2:5));
170     AngleIPIP = VectorAngle(DataStore(4,2:5), DataStore(5,2:5),
171 DataStore(5,2:5), DataStore(6,2:5));
172     AngleIDIP = VectorAngle(DataStore(5,2:5), DataStore(6,2:5),
173 DataStore(6,2:5), DataStore(7,2:5));
174
175     AngleValue = {AngleTMCP2IMCP; AngleTMCP; AngleTIP;
176 AngleIMCP; AngleIPIP; AngleIDIP; []};
177
178     %% -----OUTPUT SECTION-----%
179
180     %package results & print to txt file%
181     X = num2cell(DataStore(:,3));
182     Y = num2cell(DataStore(:,4));
183     Z = num2cell(DataStore(:,5));
184
185     DataOutput(:) = {Time{:}, FingerName{:}, X{:}, Y{:}, Z{:},
186 AngleName{:}, AngleValue{:}};
187     [nrows,ncols] = size(DataOutput);
188
189     fprintf(fidtemp1,'%s\t %s\t %s\t %s\t %s\t\r\n','Time','Joints','X','Y
190 ','Z');
191     for row = 1:nrows
192         fprintf(fidtemp1,formatSpec1,DataOutput{row,(1:5)});
193     end
194
195     fprintf(fidtemp2, formatSpec2, DataOutput{1,1}, DataOutput{:},7);
196
197     %% -----DISPLAY SECTION-----%
198
199     [X01,Y01,Z01]=cylinder2P(Ra,5,OP(2:4),DataStore(1,3:5));
200     [X02,Y02,Z02]=cylinder2P(Ra,5,DataStore(1,3:5),DataStore(2,3:5));
201     [X03,Y03,Z03]=cylinder2P(Ra,5,DataStore(2,3:5),DataStore(3,3:5));
202
203     [X11,Y11,Z11]=cylinder2P(Ra,n,OP(2:4),DataStore(4,3:5));

```

```
204 [X12,Y12,Z12]=cylinder2P(Ra,n,DataStore(4,3:5),DataStore(5,3:5));
205 [X13,Y13,Z13]=cylinder2P(Ra,n,DataStore(5,3:5),DataStore(6,3:5));
206 [X14,Y14,Z14]=cylinder2P(Ra,n,DataStore(6,3:5),DataStore(7,3:5));
207
208 %display segment in perspective view & top view%
209 subplot(1,2,1);
210
211 surf(X11,Y11,Z11);
212 hold on;
213 surf(X12,Y12,Z12);
214 hold on;
215 surf(X13,Y13,Z13);
216 hold on;
217 surf(X14,Y14,Z14);
218 hold on;
219 surf(X01,Y01,Z01);
220 hold on;
221 surf(X02,Y02,Z02);
222 hold on;
223 surf(X03,Y03,Z03);
224
225 title('3D Rotation of Thumb&Index fingers');
226 grid on;
227
228 axis equal;
229 axis([-20 20 -20 20 -20 20]);
230 hold off;
231
232 % -----
233
234 subplot(1,2,2);
235
236 surf(X11,Y11,Z11);
237 hold on;
238 surf(X12,Y12,Z12);
239 hold on;
240 surf(X13,Y13,Z13);
241 hold on;
242 surf(X14,Y14,Z14);
243 hold on;
244 surf(X01,Y01,Z01);
245 hold on;
246 surf(X02,Y02,Z02);
```



```
247     hold on;
248     surf(X03,Y03,Z03);
249
250     title('Top view Rotation of Thumb&Index fingers');
251     xlabel({'PalmPitch (X)';pitchPalm}),ylabel({'PalmRoll
252 (Y)';rollPalm});
253     grid on;
254     az = 0;
255     el = 90;
256     view(az,el);
257     axis equal;
258     axis([-20 20 -20 20 -20 20]);
259
260     %axis tight;
261     hold off;
262     drawnow limitrate;
263
264     i=i+1;
265
266     % pause(0.1);
267     end
268
269     % disp('Sample rate: 0.5s');
270     %% -----SAVE FILES & END ALL-----
271     -%
272     fileSaved1 = uiputfile('*.txt','Save coordinate record file name');
273     [fidSaved1, error3]= fopen(fileSaved1,'w');
274     copyfile(fileTemp1, fileSaved1);
275
276     fileSaved2 = uiputfile('*.txt','Save angle record file name');
277     [fidSaved2, error4]= fopen(fileSaved2,'w');
278     copyfile(fileTemp2, fileSaved2);
279
280     EndingDialog;
281
282     fclose('all');
283
284     delete(fileTemp1);
285     delete(fileTemp2);
286
```


Appendix D: Customized function code “DistalQuatMultiTransform()” in Matlab

This appendix shows the Customized function code of Matlab that have not been presented in the study of Chapter 4.

```
1 function [DistalendGlobal, DistalendLocal] =
2 DistalQuatMultiTransform(rotateq, localconjunctpoint,
3 segmentlength)
4
5
6 global Offsetquat;
7
8 %establish endpoints & gain rotated distal points at local
9 system %
10 Distalendrotated = quatmultiply(rotateq, quatmultiply([0 0
11 segmentlength 0],quatconj(rotateq)));
12
13 %translate segment to the joint & output the distalend%
14 DistalendLocal = localconjunctpoint+Distalendrotated;
15
16 %gain global endpoints %
17 DistalendGlobal = quatmultiply(Offsetquat,
18 quatmultiply(DistalendLocal,quatconj(Offsetquat)));
19
20 end
```


Appendix E: Customized function code “VectorAngle()” in Matlab

This appendix shows the Customized function code of Matlab that have not been presented in the study of Chapter 4.

```
1 function [SegsAngle] = VectorAngle(PointA1, PointA2, PointB1,  
2 PointB2)  
3  
4 VectorA = PointA2(2:4)-PointA1(2:4);  
5 VectorB = PointB2(2:4)-PointB1(2:4);  
6  
7 normA = VectorA/norm(VectorA);  
8 normB = VectorB/norm(VectorB);  
9  
10 dV = dot(normA, normB);  
11  
12 SegsAngle = acosd(dV);  
13  
14 end
```


Appendix F: Customized function code “cylinder2P()” in Matlab

This appendix shows the Customized function code of Matlab that have not been presented in the study of Chapter 4. This function is referred from Luigi Barone in the online Matlab community.

```
1 function [X, Y, Z] = cylinder2P(R, N,r1,r2)
2
3 % The parametric surface will consist of a series of N-sided
4 % polygons with successive radii given by the array R.
5 % Z increases in equal sized steps from 0 to 1.
6
7 % Set up an array of angles for the polygon.
8 theta = linspace(0,2*pi,N);
9
10 m = length(R);          % Number of radius values
11                        % supplied.
12
13 if m == 1              % Only one radius value supplied.
14     R = [R; R];        % Add a duplicate radius to make
15     m = 2;             % a cylinder.
16 end
17
18
19 X = zeros(m, N);      % Preallocate memory.
20 Y = zeros(m, N);
21 Z = zeros(m, N);
22
23 v=(r2-r1)/sqrt((r2-r1)*(r2-r1)); %Normalized vector;
24 %cylinder axis described by: r(t)=r1+v*t for 0<t<1
25 R2=rand(1,3);        %linear independent vector (of v)
26 x2=v-R2/(R2*v');    %orthogonal vector to v
27 x2=x2/sqrt(x2*x2'); %orthonormal vector to v
28 x3=cross(v,x2);     %vector orthonormal to v and x2
```

```
29     x3=x3/sqrt(x3*x3');
30
31     r1x=r1(1);r1y=r1(2);r1z=r1(3);
32     r2x=r2(1);r2y=r2(2);r2z=r2(3);
33     vx=v(1);vy=v(2);vz=v(3);
34     x2x=x2(1);x2y=x2(2);x2z=x2(3);
35     x3x=x3(1);x3y=x3(2);x3z=x3(3);
36
37     time=linspace(0,1,m);
38     for j = 1 : m
39         t=time(j);
40         X(j, :) = r1x+(r2x-r1x)*t+R(j)*cos(theta)*x2x+R(j)*sin(theta)*x3x;
41         Y(j, :) = r1y+(r2y-r1y)*t+R(j)*cos(theta)*x2y+R(j)*sin(theta)*x3y;
42         Z(j, :) = r1z+(r2z-r1z)*t+R(j)*cos(theta)*x2z+R(j)*sin(theta)*x3z;
43     end
```


Appendix G: RepRap G-Code Cheat Sheet (excerpted)

This appendix shows the code of RepRap in Simplify3D that have not been explained in detail in the fabrication process of Chapter 5.

Comm.	Parameters	Description	Example
G0	Axis [X/Y/Z] Position	Rapid Movement	G0 X50
G1	Axis [X/Y/Z/E] Position Feed [F]	Controlled Movement	G1 F150 X10
G21		Set units to mm	G21
G28	<Axis [X/Y/Z]>	Home	G28 X Y
G90	none	Absolute Positioning	G90
G91	none	Relative Positioning	G91
G92	Axis [X/Y/Z/E] Value	Set Position to value	G92 X5 Y10
M82	none	set extruder to absolute mode	M82
M84	none	Steppers off	M84
M104	Temperature[S]	Set extruder temperature (not waiting)	M104 S100
M107	none	Turn Fan off	M107
M109	Temperature[S]	Set extruder Temperature (waits till reached)	M109 S123
M140	Degrees[S]	Set heated bed temperature to S (not waiting)	M140 S55
M400	none	Finish all moves	M400
T	No.	Select extruder no. (starts with 0)	T1

Appendix H: Starting Script in Simplify3D

This appendix shows the main GCode of Starting Script that have not been presented in the study of Chapter 5.

```
1 G21 ;Metric values
2 G90 ;Absolut positioning
3 M82 ;set extruder to absolute mode
4 G28 ;home position all axis
5 G0 Z10 F3600 ;Go start position
6 M109 S[extruder0_temperature] T0 ;Set up extruder temperature
7 M109 S[extruder1_temperature] T1 ;Set up extruder temperature
8 G92 E0 ;Zero extruder position
9 T1
10 G1 E35 F200 ;Extrude 35mm of filament
11 G92 E0 ;Zero extruder position
12 M400 ;Finish all moves
```


Appendix I: Tool Change Script in Simplify3D

This appendix shows the main GCode of Tool Change Script that have not been entirely presented in the study of Chapter 5.

```
1 G90 ;Absolut positioning
2 G1 X150 F5000 ;Move head to the resting position
3 G1 Y180 F5000 ;Move head to the resting position
4 G1 Z0 F1200 ;Encounter to the bed
5
6 T[old_tool]
7 M109 S160 T[old_tool] ;Set up the previous nozzle to resting
8 temperature
9 T[new_tool]
10 M109 S220 T[new_tool] ;Set up the new nozzle to working
11 temperature
12
13 G91 ;Relative positioning
14 G1 Z3 F1200 ;Lift head to a safety height
15 G90 ;Absolut positioning
16
17 M400 ;Finish all move
```


Appendix J: Ending Script in Simplify3D

This appendix shows the main GCode of Ending Script that have not been presented in the study of Chapter 5.

```
1  M400                                ;Finish all moves
2  M104 S0      T0                      ;Extruder heater off
3  M104 S0      T1                      ;Extruder heater off
4  M140 S0      ;Heat bed heater off
5  G91      ;Relative positioning
6  G1 Z+10 E-10 F600                    ;Retract 10mm of filament
7  G1 Z+20 X-20 Y-20 F6000              ;Move axis
8  G90      ;Absolut positioning
9  G0 X0 Y210 F6000                    ;Go to X Y repose position
10 G0 Z185                               ;Down Z axis
11 M107                                  ;
12 M84                                  ;Steppers off
```


Appendix K: Publications

This appendix includes the front page of the articles that have already been published by the author of this thesis.

Conferences:

Cao, C., Cazón-Martín, A., Rodríguez-Ferradas, M.I., and Paz, Morer-Camo., 2019, “Development of a Low-Cost Wearable Prevention System for Musculoskeletal Disorders Using Inertial Measurement Unit Systems,” JCM 2018, (June)

Book Chapter

Cao, C., Rodríguez-Ferradas, M.I., Cazón-Martín, A. y Morer-Camo, Paz “Development of a low-cost wearable system with Arduino for musculoskeletal disorders prevention” from the book “Lecture Notes in Mechanical Engineering. Advances on Mechanics Design and Manufacturing II” Francisco Cavas-Martínez, Benoit Eynard, Francisco J. Fernández Cañavate, Daniel G. Fernández-Pacheco, Paz Morer, Vincenzo Nigrelli. SPRINGER 2019. ISBN: 978-3-030-12345-1.

Peer-reviewed journal

Cao, C., Cazón-Martín, A., Rodríguez-Ferradas, M.I., and Paz, Morer-Camo., Luis Matey-Muñoz., Unai Etxaniz-Sein, Hector Morcillo-Fuentes and Daniel Aguinaga-Azpiazu., 2019, “Methodology for the additive manufacture of embedded conductive paths connecting microelectromechanical sensors using conductive and flexible filaments with extrusion devices,” Rapid Prototyping Journal., 26/2(2020), pp. 349–359.



Development of a Low-Cost Wearable Prevention System for Musculoskeletal Disorders Using Inertial Measurement Unit Systems

C. Cao^(✉), M. I. Rodríguez-Ferradas, A. Cazón-Martin,
and Paz Morer

Department of Mechanical Engineering, University of Navarra-TECNUN,
San Sebastián, Spain
cca0@tecnun.es

Abstract. The increasing relevance of occupational injuries and illness related to lean manufacturing strategies in automotive assembly lines brings an increasing interest in this industry by the research and development of new tools and methods for the evaluation and prevention of work-related musculoskeletal disorders (WMSDs). However, few studies have focused on assessing the exposures to the hand region whereas disorder in this region remain at the primary tier of the prevalence ranking. Herein, this paper presents a low-cost, wearable inertial measurement unit (IMU) to measure workplace demands. This technology was selected after analysing an assessment scale composed of seven of the common ergonomic assessment tools and methods. After a brief verification through a laboratory goniometry experiment, eleven joint angles of a volunteer's hand were measured. The results indicated that the mean difference between the values measured by participants and the values obtained directly from the wearable is 2.44°, which has the same accuracy level of the commercial products. The proposed device is scalable enough to be iterated by further improvements, including conductive fabric 3D printing technology.

Keywords: Work-related musculoskeletal disorders · Automotive assembly lines · Measurements assessment · Inertial measurement units · Arduino

1 Introduction

Work-related musculoskeletal disorders (WMSDs), such as Carpal Tunnel Syndrome, Radial Tunnel Syndrome or Tendonitis, are some of the most common injuries in the manufacturing sector that generates pain in the musculoskeletal system [1]. WMSDs led to 3,138,000 lost workdays in the United Kingdom in the period 2015–16 [2] and a total cost of lost productivity of €240 billion or up to 2% of gross domestic product (GDP) in 2015 in the European Union [3]. Repetitive movement, excessive force, enduring awkward postures as well as psychological factors are the main exposures that cause WMSDs [4]. Many studies try to prevent these situations by measuring and




[Advances on Mechanics, Design Engineering and Manufacturing II](#) pp 41-51 | [Cite as](#)

Development of a Low-Cost Wearable Prevention System for Musculoskeletal Disorders Using Inertial Measurement Unit Systems

Authors

Authors and affiliations

C. Cao , M. I. Rodríguez-Ferradas, A. Cazón-Martín, Paz Morer

Conference paper

First Online: 28 April 2019

456

Downloads

Part of the [Lecture Notes in Mechanical Engineering](#) book series (LNME)

Abstract

The increasing relevance of occupational injuries and illness related to lean manufacturing strategies in automotive assembly lines brings an increasing interest in this industry by the research and development of new tools and methods for the evaluation and prevention of work-related musculoskeletal disorders (WMSDs). However, few studies have focused on assessing the exposures to the hand region whereas disorder in this region remain at the primary tier of the prevalence ranking. Herein, this paper presents a low-cost, wearable inertial measurement unit (IMU) to measure workplace demands. This technology was selected after analysing an assessment scale composed of seven of the common ergonomic assessment tools and methods. After a brief verification through a laboratory goniometry experiment, eleven joint angles of a volunteer's hand were measured. The results indicated that the mean difference between the values measured by participants and the values obtained directly from the wearable is 2.44° , which has the same accuracy level of the commercial products. The proposed device is scalable enough to be iterated by further improvements, including conductive fabric 3D printing technology.

Methodology for the additive manufacture of embedded conductive paths connecting microelectromechanical sensors using conductive and flexible filaments with extrusion devices

Chuan Cao, Aitor Cazón-Martín, María Isabel Rodríguez-Ferradas and Paz Morer-Camo
Department of Mechanical Engineering, University of Navarra, Donostia, Spain

Luis Matey-Muñoz

Department of Mechanical Engineering, University of Navarra, Donostia, Spain, and Department of Manufacturing Division,
University of Navarra, Donostia, Spain, and

Unai Etxaniz-Sein, Hector Morcillo-Fuentes and Daniel Aguinaga-Azpiazu
Research and Development Centre, IKOR Technology Centre S.L. (ITC), Donostia, Spain

Abstract

Purpose – The purpose of this study is to explore a methodology for connecting microelectromechanical system sensors – i.e. inertial measurement unit (IMU) – to an Arduino-based microcontroller, using graphene-based conductive filament and flexible thermoplastic polyurethane (FTPU) filament and low-cost dual material extrusion technology.

Design/methodology/approach – A series of electrical tests were carried out to determine the maximum resistance the conductive paths may take to connect printed circuit boards (PCB). To select the most suitable printing material, three types of conductive filaments were examined. Then an experiment was carried out to find the best printing parameters in terms of printing speed, printing temperature and layer height to minimise resistivity. The size of the conductive path was also analysed. A final prototype was designed and printed according to optimised printing settings and maximum allowable resistances for each line and considering different geometries and printing strategies to reduce cross-contamination among paths.

Findings – For the Black Magic 3D conductive filament, the printing speed and layer height played a significant role regarding resistivity, while the printing temperature was not very important. The infill pattern of the conductive paths had to be aligned with the expected current path, while using air gaps between two adjacent paths resulted in the best approach to reducing cross-contamination. Moreover, the cross-section size of the conductive path did not affect the volume resistivity. When combined with FTPU filament constraints, the prototype yielded suitable electrical performance and printing quality when printed at a temperature of 220°C, speed of 20 mm/s and layer height of 0.2 mm.

Originality/value – This paper explores a systematic methodology for the additive manufacturing of commercial conductive material using low-cost extrusion technology to connect complex electronics when data transmission is a key feature.

Keywords Additive manufacturing, Arduino, Extrusion, Conductive material, Dual material print, Inertial measurement unit

Paper type Research paper

1. Introduction

Additive manufacturing (AM), commonly known as 3D printing, is a booming technology that enables a computerised 3D solid model to be directly transformed into a final complex shape by adding materials. This technology achieves considerable efficiency in raw material use, while traditional manufacturing approaches rarely achieve such a cost-effective

level of consumption (Huang *et al.*, 2013; Ngo *et al.*, 2018). Among AM devices, material extrusion is one of the fastest, lowest-cost, most easy-to-use and widely available techniques on the market (Raasch *et al.*, 2015). The working principle for this technique is to selectively deposit a semi-solid thermoplastic material through a nozzle or orifice. The thermoplastic material is first heated and then extruded through the nozzle in single paths to form each layer of the task object. Extrusion devices support a variety of thermoplastic materials for printing, such as Acrylonitrile Butadiene Styrene (ABS), PolyLactic Acid (PLA), Thermoplastic PolyUrethane

The current issue and full text archive of this journal is available on Emerald Insight at: <https://www.emerald.com/insight/1355-2546.htm>



Rapid Prototyping Journal
26(2) (2020) 349–359
© Emerald Publishing Limited [ISSN 1355-2546]
[DOI 10.1108/RPJ-03-2019-0058]

Received 6 March 2019
Revised 17 July 2019
Accepted 3 September 2019

List of nomenclature

Acronyms and definitions

3DSSPP	Three-Dimensional Static Strength Prediction Program
ABS	Acrylonitrile Butadiene Styrene
ADR	Address Pin
ACC	Accelerometry
AM	Additive Manufacturing
ANOVA	Analysis of Variance
AREF	Analogue REFerence
ART	Assessment of Repetitive Tasks
BA	Biomechanical Assessment
BLS	Bureau of Labour Statistics
CB	Carbon Black
CF	Carbon Fibers
CMC	Carpometacarpal
CMDQ	Cornell Musculoskeletal Discomforts Questionnaire
CNT	Carbon Nanotubes
CSRs	Conductive Silicon Rubbers
CTD	Cumulative Trauma Disorder
CTS	Carpal Tunnel Syndrome
DC	Direct Current
DIP	Distal Interphalangeal
DMLS	Direct Metal Laser Sintering
DoF	Degree of Freedom
DSLR	Digital Single-Lens Reflex
EEPROM	Electrically-Erasable Programmable Read-Only Memory
EG	Electro Goniometer
EMG	Electromyography
FAT	File Allocation Table
FDM	Fused Deposition Modelling
FFF	Fused Filament Fabrication
FLM	Fused Layer Modelling
FTPU	Flexible Thermoplastic Polyurethane

GDP	Gross Domestic Product
GHQ	General Health Questionnaire
Gr	Graphene
HSE	Health and Safety Executive
I2C	Inter-Integrated Circuit
ICF	Information-Weighted Consensus Filter
IDE	Integrated Development Environment
IMU	Inertial Measurement Units
IP	Interphalangeal
LED	Light-Emitting Diodes
LMC-GPR	Linear Mean Composite Gaussian Process Regression
MCP	Metacarpophalangeal
MEMS	Microelectromechanical Systems
MISO	Master Input,Slave Output
MOSI	Master Output,Slave Input
MSDs	Musculoskeletal Disorders
NIOSH	National Institute of Occupational Safety and Health
NMQ	Nordic Musculoskeletal Questionnaires
OES	Optoelectronic Systems
OWAS	OVAKO Working Posture Analysing System
PATH	Posture, Activity, Tools and Handling
PCB	Printed Circuit Board
PIP	Proximal Interphalangeal
PLA	Polylactic Acid
PWM	Pulse Width Modulation
REBA	Rapid Entire Body Assessment
RFID	Radio Frequency Identification
RMSD	Root Mean Square Distance
ROM	Range of Motion
RSI	Repetitive Strain Injury
RULA	Rapid Upper Limb Assessment
RWL	Recommended Of Weight Limits
SCL	Serial Clock
SD	Secure Digital
SDA	Serial Data
SLA	Stereolithography
SLERP	Spherical Linear Interpolation

SLM	Selective Laser Melting
SLS	Selective Laser Sintering
SNQ	Standardized Nordic Questionnaire
SPGPs	Sparse Pseudo-input Gaussian Processes
SPI	Serial Peripheral Interface Bus
SRAM	Static Random Access Memory
SS	Slave Selected
TPE	Thermoplastic Elastomer
TPU	Thermoplastic Polyurethane
TWI	Two-Wire Interface
WMSDs	Work-related Musculoskeletal Disorders
WSP	Workload Screening Procedure

List of symbols

Ψ	Yaw angle
Θ	Pitch angle
Φ	Roll angle
\mathbf{E}	Euler Angle
E_1, E_2	First and second rotation in Euler angle
\mathbf{R}	Rotation matrix
α	Yaw angle in Rotation matrix
β	Pitch angle in Rotation matrix
γ	Roll angle in Rotation matrix
\mathbf{Q}	Quaternion
$\mathbf{x}, \mathbf{y}, \mathbf{z}$	Vector part of quaternion
w	Scalar part of quaternion
\mathbf{u}	Unit vector along Axis of Rotation
σ	Rotation angle in Axis-angle system
q	Unit quaternion
q^{-1}	Reciprocal of quaternion
q^*	Conjugation of quaternion
p	Spatial coordinates
p'	Spatial coordinates after rotation

Bibliography

- [1] American Federation of Labor and Congress of Industrial Organizations (AFL-CIO), *The Toll of Neglect DEATH ON THE JOB A NATIONAL AND STATE-BY-STATE PROFILE OF WORKER SAFETY AND HEALTH IN THE UNITED STATES*, (2018) 1–212.
- [2] S. Simoneau, M. St-vincent, D. Chicoine, *Work related musculoskeletal disorders (WMSDs) - a better understanding for more effective prevention*, 1996.
- [3] R. Scott, R. Scott, *Physical and Biological Hazards in the Workplace*, in: *Basic Concepts Ind. Hyg.*, 2018: pp. 233–328. doi:10.1201/9781315138077-15.
- [4] T. Koukoulaki, *The impact of lean production on musculoskeletal and psychosocial risks: An examination of sociotechnical trends over 20 years*, *Appl. Ergon.* 45 (2014) 198–212. doi:10.1016/j.apergo.2013.07.018.
- [5] M. Motamedzade, M.A. Faghih, R. Golmohammadi, J. Faradmali, H. Mohammadi, *Effects of physical and personal risk factors on sick leave due to musculoskeletal disorders*, *Int. J. Occup. Saf. Ergon.* 19 (2013) 513–521. doi:10.1080/10803548.2013.11077012.
- [6] P. Buckley, *Work-related Musculoskeletal Disorder Statistics*, Great Britain, 2016.

- [7] S. Bevan, Economic impact of musculoskeletal disorders (MSDs) on work in Europe, *Best Pract. Res. Clin. Rheumatol.* 29 (2015) 356–373. doi:10.1016/j.berh.2015.08.002.
- [8] V. D.J., W. A.D., C. A.J., Chronic musculoskeletal pain and arthritis: Impact, attitudes and perceptions, *Ir. Med. J.* 101 (2008).
- [9] Commission asks workers and employers what action should be taken to combat musculoskeletal disorders, *Eur. Comm.* (2004) http://europa.eu/rapid/press-release_IP-04-1358_en.
- [10] V. Nestorova, I. Mircheva, WORK-RELATED MUSCULOSKELETAL DISORDERS (WMSDS): RISK FACTORS , DIAGNOSIS AND PREVENTION, *Scr. Sci. Salut. Publicae.* 4 (2018) 15–21.
- [11] C. Varianou-Mikellidou, G. Boustras, C. Dimopoulos, J.L. Wybo, F.W. Guldenmund, O. Nicolaidou, I. Anyfantis, Occupational health and safety management in the context of an ageing workforce, *Saf. Sci.* 116 (2019) 231–244. doi:10.1016/j.ssci.2019.03.009.
- [12] K. Fredriksson, C. Bildt, G. Hägg, Å. Kilbom, The impact on musculoskeletal disorders of changing physical and psychosocial work environment conditions in the automobile industry, *Int. J. Ind. Ergon.* 28 (2001) 31–45. doi:10.1016/S0169-8141(01)00011-7.
- [13] B. Widanarko, S. Legg, J. Devereux, M. Stevenson, The combined effect of physical, psychosocial/organisational and/or environmental risk factors on the presence of work-related musculoskeletal symptoms and its consequences, *Appl. Ergon.* 45 (2014) 1610–1621. doi:10.1016/j.apergo.2014.05.018.
- [14] M. Zare, J. Bodin, E. Cercier, R. Brunet, Y. Roquelaure, Evaluation of ergonomic approach and musculoskeletal disorders in two different organizations in a truck assembly plant, *Int. J. Ind. Ergon.* 50 (2015) 34–42. doi:10.1016/j.ergon.2015.09.009.
- [15] Z.-X. Wang, R.-L. Qin, Y.-Z. Li, X.-Y. Zhang, N. Jia, Q.-L. Zhang, G. Li, J. Zhao, H.-H. Li, H.-Q. Jiang, [The epidemiological study of work-related musculoskeletal disorders and related factors among automobile assembly workers], *Zhonghua Lao Dong Wei*

- Sheng Zhi Ye Bing Za Zhi. 29 (2011) 572–578.
- [16] P. L., W. D.H., Work-related musculoskeletal disorders: The epidemiologic evidence and the debate, *J. Electromyogr. Kinesiol.* 14 (2004) 13–23. doi:10.1016/j.jelekin.2003.09.015.
- [17] K. Landau, H. Rademacher, H. Meschke, G. Winter, K. Schaub, M. Grasmueck, I. Moelbert, M. Sommer, J. Schulze, Musculoskeletal disorders in assembly jobs in the automotive industry with special reference to age management aspects, *Int. J. Ind. Ergon.* 38 (2008) 561–576. doi:10.1016/j.ergon.2008.01.006.
- [18] H.S. Lee, J.Y. Kim, Prevalence of Work-related Musculoskeletal Disorders in Auto-mission Assembly Plant Workers, 34 (2015) 293–302.
- [19] T. Hussain, Musculoskeletal symptoms among truck assembly workers, *Occup. Med. (Chic. Ill).* 54 (2004) 506–512. doi:10.1093/occmed/kqh087.
- [20] K.S.H.& M.Y.A. A.R. Anita, A. Yazdani, Association between Awkward Posture and Musculoskeletal Symptom among Automobile Assembly Line Workers in Malaysia, 10 (2014) 22–28.
- [21] N.M. Nur, S.Z. Dawal, M. Dahari, The Prevalence of Work Related Musculoskeletal Disorders Among Workers Performing Industrial Repetitive Tasks in the Automotive Manufacturing Companies, *Int. Conf. Ind. Eng. Oper. Manag. Bali, Indones.* (2014) 1–8.
- [22] F.A. Aziz, Z. Ghazalli, N.M.Z. Mohamed, A. Isfar, Investigation on musculoskeletal discomfort and ergonomics risk factors among production team members at an automotive component assembly plant, *IOP Conf. Ser. Mater. Sci. Eng.* 257 (2017). doi:10.1088/1757-899X/257/1/012040.
- [23] C. Nordander, K. Ohlsson, I. Åkesson, I. Arvidsson, I. Balogh, G.Å. Hansson, U. Strömberg, R. Rittner, S. Skerfving, Exposure-response relationships in work-related musculoskeletal disorders in elbows and hands - A synthesis of group-level data on exposure and response obtained using uniform methods of data collection, *Appl. Ergon.* 44 (2013) 241–253. doi:10.1016/j.apergo.2012.07.009.

- [24] K.T. Palmer, Regional musculoskeletal conditions: pain in the forearm, wrist and hand., *Best Pract. Res. Clin. Rheumatol.* 17 (2003) 113–135.
- [25] R.M. Van Rijn, B.M. Huisstede, B.W. Koes, A. Burdorf, Associations between work-related factors and specific disorders of the shoulder - A systematic review of the literature, *Scand. J. Work. Environ. Heal.* 36 (2010) 189–201. doi:10.5271/sjweh.2895.
- [26] P.J. Keir, J.M. Bach, M. Hudes, D.M. Rempel, Guidelines for Wrist Posture Based on Carpal Tunnel Pressure Thresholds, *Hum. Factors J. Hum. Factors Ergon. Soc.* 49 (2007) 88–99. doi:10.1518/001872007779598127.
- [27] B.A. Silverstein, L.J. Fine, T.J. Armstrong, Hand wrist cumulative trauma disorders in industry., *Br. J. Ind. Med.* 43 (1986) 779–784. doi:10.1136/oem.43.11.779.
- [28] A.J. Van Der Beek, M.H.W. Frings-Dresen, Assessment of mechanical exposure in ergonomic epidemiology, *Occup. Environ. Med.* 55 (1998) 291–299. doi:10.1136/oem.55.5.291.
- [29] Jø. Winkel, S.E. Mathiassen, Assessment of physical work load in epidemiologic studies: Concepts, issues and operational considerations, *Ergonomics.* 37 (1994) 979–988. doi:10.1080/00140139408963711.
- [30] P. Spielholz, B. Silverstein, M. Morgan, H. Checkoway, J. Kaufman, Comparison of self-report, video observation and direct measurement methods for upper extremity musculoskeletal disorder physical risk factors., *Ergonomics.* 44 (2001) 588–613. doi:10.1080/00140130118050.
- [31] A. Burdorf, J. Laan, Comparison of methods for the assessment of postural load on the back, *Scand. J. Work. Environ. Heal.* 17 (1991) 425–429. doi:10.5271/sjweh.1679.
- [32] C. Wiktorin, L. Karlqvist, J. Winkel, Validity of self-reported exposures to work postures and manual materials handling, *Scand. J. Work. Environ. Heal.* 19 (1993) 208–214. doi:10.5271/sjweh.1481.
- [33] E. Viikari-Juntura, S. Rauas, R. Martikainen, E. Kuosma, H. Riihimäki, E.P. Takala, K. Saarenmaa, Validity of self-reported

- physical work load in epidemiologic studies on musculoskeletal disorders, *Scand. J. Work. Environ. Heal.* 22 (1996) 251–259. doi:10.5271/sjweh.139.
- [34] I. Balogh, P. Ørbæk, K. Ohlsson, C. Nordander, J. Unge, J. Winkel, G.Å. Hansson, Self-assessed and directly measured occupational physical activities - Influence of musculoskeletal complaints, age and gender, *Appl. Ergon.* 35 (2004) 49–56. doi:10.1016/j.apergo.2003.06.001.
- [35] D.P. Pope, A.J. Silman, N.M. Cherry, C. Pritchard, G.J. Macfarlane, Validity of a self-completed questionnaire measuring the physical demands of work, *Scand. J. Work. Environ. Heal.* 24 (1998) 376–385. doi:10.5271/sjweh.358.
- [36] A. Burdorf, A.J. Van der Beek, In musculoskeletal epidemiology are we asking the unanswerable in questionnaires on physical load?, *Scand. J. Work. Environ. Heal.* 25 (1999) 81–83. doi:10.5271/sjweh.409.
- [37] G. Li, P. Buckle, Current techniques for assessing physical exposure to work-related musculoskeletal risks, with emphasis on posture-based methods, *Ergonomics.* 42 (1999) 674–695. doi:10.1080/001401399185388.
- [38] I. Kuorinka, B. Jonsson, A. Kilbom, H. Vinterberg, F. Biering-Sørensen, G. Andersson, K. Jørgensen, Standardised Nordic questionnaires for the analysis of musculoskeletal symptoms, *Appl. Ergon.* 18 (1987) 233–237. doi:10.1016/0003-6870(87)90010-X.
- [39] G.C. David, Ergonomic methods for assessing exposure to risk factors for work-related musculoskeletal disorders, *Occup. Med. (Chic. Ill).* 55 (2005) 190–199. doi:10.1093/occmed/kqi082.
- [40] Rapid Upper Limb Assessment (RULA) Worksheet Tool – A Step by Step Guide, Morgan Maxwell. (2018).
- [41] O. Karhu, P. Kansu, I. Kuorinka, Correcting working postures in industry: A practical method for analysis, *Appl. Ergon.* 8 (1977) 199–201. doi:10.1016/0003-6870(77)90164-8.
- [42] W.M. Keyserling, M. Brouwer, B.A. Silverstein, A checklist for evaluating ergonomic risk factors resulting from awkward postures of the legs, trunk and neck, *Int. J. Ind. Ergon.* 9 (1992)

- 283–301. doi:10.1016/0169-8141(92)90062-5.
- [43] L. McAtamney, E. Nigel Corlett, RULA: a survey method for the investigation of work-related upper limb disorders, *Appl. Ergon.* 24 (1993) 91–99. doi:10.1016/0003-6870(93)90080-S.
- [44] T.R. Waters, V. Putz-Anderson, A. Garg, L.J. Fine, Revised NIOSH equation for the design and evaluation of manual lifting tasks, *Ergonomics*. 36 (1993) 749–776. doi:10.1080/00140139308967940.
- [45] G. Li, P. Buckle, Evaluating Change in Exposure to Risk for Musculoskeletal Disorders — A Practical Tool, *Proc. Hum. Factors Ergon. Soc. Annu. Meet.* 44 (2012) 5-407-5–408. doi:10.1177/154193120004403001.
- [46] S. Hignett, L. McAtamney, Rapid Entire Body Assessment (REBA), *Appl. Ergon.* 31 (2000) 201–205. doi:10.1016/S0003-6870(99)00039-3.
- [47] B. Buchholz, V. Paquet, L. Punnett, D. Lee, S. Moir, PATH: A work sampling-based approach to ergonomic job analysis for construction and other non-repetitive work, *Appl. Ergon.* 27 (1996) 177–187. doi:10.1016/0003-6870(95)00078-X.
- [48] D. Wang, F. Dai, X. Ning, Risk Assessment of Work-Related Musculoskeletal Disorders in Construction: State-of-the-Art Review, *J. Constr. Eng. Manag.* 141 (2015) 04015008. doi:10.1061/(ASCE)CO.1943-7862.0000979.
- [49] Industrial Lumbar Motion Monitor™ (iLMM3™), *Ergon. NexGen.* (n.d.).
- [50] R.G. Radwin, M. Li Lin, An analytical method for characterizing repetitive motion and postural stress using spectral analysis, *Ergonomics*. 36 (1993) 379–389. doi:10.1080/00140139308967895.
- [51] A. Freivalds, Y. Kong, H. You, S. Park, A Comprehensive risk Assessment Model for Work-Related Musculoskeletal Disorders of the Upper Extremities, *Proc. Hum. Factors Ergon. Soc. Annu. Meet.* 44 (2012) 5-728-5–731. doi:10.1177/154193120004403129.
- [52] R. Wells, R. Norman, P. Neumann, D. Andrews, J. Frank, H. Shannon, M. Kerr, Assessment of physical work load in

- epidemiologic studies: Common measurement metrics for exposure assessment, *Ergonomics*. 40 (1997) 51–61. doi:10.1080/001401397188369.
- [53] W.S. Marras, F.A. Fathallah, R.J. Miller, S.W. Davis, G.A. Mirka, Accuracy of a three-dimensional lumbar motion monitor for recording dynamic trunk motion characteristics, *Int. J. Ind. Ergon.* 9 (1992) 75–87. doi:10.1016/0169-8141(92)90078-E.
- [54] G. Hasson, P. Asterland, N. Holmer, S. Skerfving, Validity, reliability and applications of an inclinometer based on accelerometers, in: X2001—Exposure Assess. *Epidemiol. Pract.*, 2001: pp. 405–407.
- [55] E. Bernmark, C. Wiktorin, A triaxial accelerometer for measuring arm movements, *Appl. Ergon.* 33 (2002) 541–547. doi:10.1016/S0003-6870(02)00072-8.
- [56] M. Fiorentino, A.E. Uva, G. Monno, G.F. Trotta, V. Bevilacqua, V.M. Manghisi, Real time RULA assessment using Kinect v2 sensor, *Appl. Ergon.* 65 (2017) 481–491. doi:10.1016/j.apergo.2017.02.015.
- [57] P.W. Johnson, M. Hagberg, E. Wigaeus Hjelm, D. Rempel, Measuring and characterizing force exposures during computer mouse use, *Scand. J. Work. Environ. Heal.* 26 (2000) 398–405. doi:10.5271/sjweh.560.
- [58] K.S. Lee, M.C. Jung, Ergonomic evaluation of biomechanical hand function, *Saf. Health Work.* 6 (2015) 9–17. doi:10.1016/j.shaw.2014.09.002.
- [59] P. Terry, Joint Structure and Function – A comprehensive analysis, *Physiotherapy*. 78 (2010) 550. doi:10.1016/s0031-9406(10)61178-9.
- [60] H.-L. Yu, R.A. Chase, B.S. Mosby, *Atlas of hand anatomy and clinical implications*, 2004.
- [61] C. Choi, M. Shin, S. Kwon, W. Park, J. Kim, Understanding of hands and task characteristics for development of biomimetic robot hands, 2008 8th IEEE-RAS Int. Conf. Humanoid Robot. *Humanoids* 2008. (2008) 413–417. doi:10.1109/ICHR.2008.4755986.

- [62] Y. Wang, M. Neff, Data-driven glove calibration for hand motion capture, Proc. 12th ACM SIGGRAPH/Eurographics Symp. Comput. Animat. - SCA '13. (2013) 15. doi:10.1145/2485895.2485901.
- [63] K. Kitano, S. Member, A. Ito, N. Tsujiuchi, Estimation of Joint Center and Measurement of Finger Motion by Inertial Sensors, (2016) 5668–5671.
- [64] N.A. Baker, R. Cham, E. Hale, J. Cook, M.S. Redfern, Digit kinematics during typing with standard and ergonomic keyboard configurations, Int. J. Ind. Ergon. 37 (2007) 345–355. doi:10.1016/j.ergon.2006.12.004.
- [65] P. Plantard, E. Auvinet, A.S. Le Pierres, F. Multon, Pose estimation with a kinect for ergonomic studies: Evaluation of the accuracy using a virtual mannequin, Sensors (Switzerland). 15 (2015) 1785–1803. doi:10.3390/s150101785.
- [66] P. Plantard, H.P.H. Shum, A.S. Le Pierres, F. Multon, Validation of an ergonomic assessment method using Kinect data in real workplace conditions, Appl. Ergon. 65 (2017) 562–569. doi:10.1016/j.apergo.2016.10.015.
- [67] Cyber Glove, CyberGlove II Wireless Glove, Online Webpage. (2009) 1–6.
- [68] R. Zheng, J. Li, Kinematics and workspace analysis of an exoskeleton for thumb and index finger rehabilitation, in: 2010 IEEE Int. Conf. Robot. Biomimetics, ROBIO 2010, 2010: pp. 80–84. doi:10.1109/ROBIO.2010.5723307.
- [69] R. Yoshida, H.O. House, R.M. Patterson, M.A. Shah, S.F. Viegas, Motion and morphology of the thumb metacarpophalangeal joint, J. Hand Surg. Am. 28 (2003) 753–757. doi:10.1016/S0363-5023(03)00303-4.
- [70] R. Degeorges, C. Oberlin, Measurement of three-joint-finger motions: Reality or fancy? A three-dimensional anatomical approach, Surg. Radiol. Anat. 25 (2003) 105–112. doi:10.1007/s00276-003-0104-3.
- [71] M.C. Hume, H. Gellman, H. McKellop, R.H. Brumfield, Functional range of motion of the joints of the hand, J. Hand Surg. Am. 15 (1990) 240–243. doi:10.1016/0363-5023(90)90102-

W.

- [72] C.W. Chao EY, An KN, *Biomechanics of the Hand: A Basic Research Study*, World Scientific, 1989.
- [73] J.C. Becker, N. V. Thakor, *A Study of the Range of Motion of Human Fingers with Application to Anthropomorphic Designs*, *IEEE Trans. Biomed. Eng.* 35 (1988) 110–117. doi:10.1109/10.1348.
- [74] A.B. Swanson, *Flexible implant arthroplasty for arthritic finger joints: rationale, technique, and results of treatment.*, *J. Bone Joint Surg. Am.* 54 (1972) 435–55.
- [75] M. Sama, V. Pacella, E. Farella, L. Benini, B. Riccò, *3dID: A low-power, low-cost hand motion capture device*, *Proc. -Design, Autom. Test Eur. DATE.* 2 (2006). doi:10.1109/DATE.2004.1269064.
- [76] S.W. Kwok, K.H.H. Goh, Z.D. Tan, S.T.M. Tan, W.W. Tjiu, J.Y. Soh, Z.J.G. Ng, Y.Z. Chan, H.K. Hui, K.E.J. Goh, *Electrically conductive filament for 3D-printed circuits and sensors*, *Appl. Mater. Today.* 9 (2017) 167–175. doi:10.1016/j.apmt.2017.07.001.
- [77] S.H. Huang, P. Liu, A. Mokasdar, L. Hou, *Additive manufacturing and its societal impact: A literature review*, *Int. J. Adv. Manuf. Technol.* 67 (2013) 1191–1203. doi:10.1007/s00170-012-4558-5.
- [78] T.D. Ngo, A. Kashani, G. Imbalzano, K.T.Q. Nguyen, D. Hui, *Additive manufacturing (3D printing): A review of materials, methods, applications and challenges*, *Compos. Part B Eng.* 143 (2018) 172–196. doi:10.1016/j.compositesb.2018.02.012.
- [79] J.W. Stansbury, M.J. Idacavage, *3D printing with polymers: Challenges among expanding options and opportunities*, *Dent. Mater.* 32 (2016) 54–64. doi:10.1016/j.dental.2015.09.018.
- [80] B. Zareiyan, B. Khoshnevis, *Interlayer adhesion and strength of structures in Contour Crafting - Effects of aggregate size, extrusion rate, and layer thickness*, *Autom. Constr.* 81 (2017) 112–121. doi:10.1016/j.autcon.2017.06.013.
- [81] S. Bin Maidin, I. Campbell, E. Pei, *Development of a design feature database to support design for additive manufacturing*,

- Assem. Autom. 32 (2012) 235–244.
doi:10.1108/01445151211244375.
- [82] X. Wang, M. Jiang, Z. Zhou, J. Gou, D. Hui, 3D printing of polymer matrix composites: A review and prospective, *Compos. Part B Eng.* 110 (2017) 442–458. doi:10.1016/j.compositesb.2016.11.034.
- [83] A. Scheck, Caroline E.; Wolk, Jennifer N.; Frazier, William E.; Mahoney, Brian T.; Morris, Kyle; Kestler, Robert; Bagchi, Naval Additive Manufacturing: Improving Rapid Response to the Warfighter, *Nav. Eng. J.* 128 (2016) 5.
- [84] B. Berman, 3-D printing: The new industrial revolution, *Bus. Horiz.* 55 (2012) 155–162. doi:10.1016/j.bushor.2011.11.003.
- [85] ASTM INTERNATIONAL, Standard Terminology for Additive Manufacturing, *Rapid Manuf. Assoc.* (2013) 1–3. doi:10.1520/F2792-12A.2.
- [86] A.B. Varotsis, Schematic of a typical FDM printer, *3D Hubs.* (n.d.).
- [87] N. Travitzky, A. Bonet, B. Dermeik, T. Fey, I. Filbert-Demut, L. Schlier, T. Schlordt, P. Greil, Additive manufacturing of ceramic-based materials, in: *Adv. Eng. Mater.*, 2014: pp. 729–754. doi:10.1002/adem.201400097.
- [88] J. Raasch, M. Ivey, D. Aldrich, D.S. Nobes, C. Ayranci, Characterization of polyurethane shape memory polymer processed by material extrusion additive manufacturing, *Addit. Manuf.* 8 (2015) 132–141. doi:10.1016/j.addma.2015.09.004.
- [89] J.V. Ecker, M. Kracalik, S. Hild, A. Haider, 3D – Material Extrusion – Printing with Biopolymers: A Review, *Chem. Mater. Eng.* 5 (2017) 83–96. doi:10.13189/cme.2017.050402.
- [90] N.M. Sazonov E, *Wearable sensors: fundamentals, implementation and applications*, Elsevier, 2014.
- [91] C. Liu, N. Huang, F. Xu, J. Tong, Z. Chen, X. Gui, Y. Fu, C. Lao, 3D printing technologies for flexible tactile sensors toward wearable electronics and electronic skin, *Polymers (Basel)*. 10 (2018) 1–31. doi:10.3390/polym10060629.
- [92] A.D. Valentine, T.A. Busbee, J.W. Boley, J.R. Raney, A. Chortos,

- A. Kotikian, J.D. Berrigan, M.F. Durstock, J.A. Lewis, Hybrid 3D Printing of Soft Electronics, *Adv. Mater.* 29 (2017) 1–8. doi:10.1002/adma.201703817.
- [93] H. He, X. Chen, L. Ukkonen, J. Virkki, Textile-integrated three-dimensional printed and embroidered structures for wearable wireless platforms, *Text. Res. J.* (2018). doi:10.1177/0040517517750649.
- [94] H. Ota, S. Emaminejad, Y. Gao, A. Zhao, E. Wu, S. Challa, K. Chen, H.M. Fahad, A.K. Jha, D. Kiriya, W. Gao, H. Shiraki, K. Morioka, A.R. Ferguson, K.E. Healy, R.W. Davis, A. Javey, Application of 3D Printing for Smart Objects with Embedded Electronic Sensors and Systems, *Adv. Mater. Technol.* 1 (2016) 1–8. doi:10.1002/admt.201600013.
- [95] C.C. Kuo, L.C. Liu, W.F. Teng, H.Y. Chang, F.M. Chien, S.J. Liao, W.F. Kuo, C.M. Chen, Preparation of starch/acrylonitrile-butadiene-styrene copolymers (ABS) biomass alloys and their feasible evaluation for 3D printing applications, *Compos. Part B Eng.* 86 (2016) 36–39. doi:10.1016/j.compositesb.2015.10.005.
- [96] H.L. Tekinalp, V. Kunc, G.M. Velez-Garcia, C.E. Duty, L.J. Love, A.K. Naskar, C.A. Blue, S. Ozcan, Highly oriented carbon fiber-polymer composites via additive manufacturing, *Compos. Sci. Technol.* 105 (2014) 144–150. doi:10.1016/j.compscitech.2014.10.009.
- [97] J. Song, C. Chen, Y. Zhang, High thermal conductivity and stretchability of layer-by-layer assembled silicone rubber/graphene nanosheets multilayered films, *Compos. Part A Appl. Sci. Manuf.* 105 (2018) 1–8. doi:10.1016/j.compositesa.2017.11.001.
- [98] D.J. Horst, P.P.A. Junior, 3D-Printed Conductive Filaments Based on Carbon Nanostructures Embedded in a Polymer Matrix, *Int. J. Appl. Nanotechnol. Res.* 4 (2019) 26–40. doi:10.4018/ijanr.2019010103.
- [99] P.F. Flowers, C. Reyes, S. Ye, M.J. Kim, B.J. Wiley, 3D printing electronic components and circuits with conductive thermoplastic filament, *Addit. Manuf.* 18 (2017) 156–163. doi:10.1016/j.addma.2017.10.002.
- [100] K. Huang, J. Yang, S. Dong, Q. Feng, X. Zhang, Y. Ding, J. Hu,

- Anisotropy of graphene scaffolds assembled by three-dimensional printing, *Carbon* N. Y. 130 (2018) 1–10. doi:10.1016/j.carbon.2017.12.120.
- [101] E. Valero, A. Sivanathan, F. Bosché, M. Abdel-Wahab, Musculoskeletal disorders in construction: A review and a novel system for activity tracking with body area network, *Appl. Ergon.* 54 (2016) 120–130. doi:10.1016/j.apergo.2015.11.020.
- [102] A.I. Faisal, S. Majumder, T. Mondal, D. Cowan, S. Naseh, Monitoring Methods of Human Body Joints :, *Sensors* (Switzerland). (2019) 1–39.
- [103] S. Wilson, J.R. and Sharples, *Evaluation of Human Work*, 2015. doi:10.1016/0003-6870(91)90014-9.
- [104] Health and Safety Executive, *Assessment of Repetitive Tasks of the upper limbs (the ART tool)- Guidance for employers*, 2010.
- [105] *Rapid Entire Body Assessment (REBA) A Step by Step Guide*, Morgan Maxwell. (2018).
- [106] D.B. Chaffin, G.B. Andersson, B.J. Martin, *Occupational biomechanics*, 4th ed., Wiley, Hoboken, NJ., 2006.
- [107] S.L. Delp, F.C. Anderson, A.S. Arnold, P. Loan, A. Habib, C.T. John, E. Guendelman, D.G. Thelen, OpenSim: Open-source software to create and analyze dynamic simulations of movement, *IEEE Trans. Biomed. Eng.* 54 (2007) 1940–1950. doi:10.1109/TBME.2007.901024.
- [108] *Visual 3D: 3D analysis toolkit for 3D biomechanics modeling, analysis, and reporting*, (2013).
- [109] M. Damsgaard, J. Rasmussen, S.T. Christensen, E. Surma, M. de Zee, Analysis of musculoskeletal systems in the AnyBody Modeling System, *Simul. Model. Pract. Theory.* 14 (2006) 1100–1111. doi:10.1016/j.simpat.2006.09.001.
- [110] S.U. Han, M. Achar, S.H. Lee, F. Peña-Mora, Empirical assessment of a RGB-D sensor on motion capture and action recognition for construction worker monitoring, *Vis. Eng.* 1 (2013). doi:10.1186/2213-7459-1-6.
- [111] A. Sanchez-Lite, M. Garcia, R. Domingo, M. Angel Sebastian, *Novel Ergonomic Postural Assessment Method (NERPA) Using*

- Product-Process Computer Aided Engineering for Ergonomic Workplace Design, *PLoS One.* 8 (2013) 1–12. doi:10.1371/journal.pone.0072703.
- [112] L. Herda, R. Urtasun, P. Fua, Hierarchical Implicit Surface Joint Limits to Constrain Video-Based Motion Capture, *Lect. Notes Comput. Sci. (Including Subser. Lect. Notes Artif. Intell. Lect. Notes Bioinformatics).* 3022 (2004) 405–418.
- [113] P. Cerveri, A. Pedotti, G. Ferrigno, Robust recovery of human motion from video using Kalman filters and virtual humans, *Hum. Mov. Sci.* 22 (2003) 377–404. doi:10.1016/S0167-9457(03)00004-6.
- [114] COMPARE CAMERAS, (n.d.).
- [115] E. Ceseracciu, Z. Sawacha, C. Cobelli, Comparison of markerless and marker-based motion capture technologies through simultaneous data collection during gait: Proof of concept, *PLoS One.* 9 (2014) 1–7. doi:10.1371/journal.pone.0087640.
- [116] G.B. Guerra-filho, Optical motion capture: Theory and implementation, *J. Theor. Appl. Informatics.* 12 (2005) 61--89.
- [117] K. Essmaeel, L. Gallo, E. Damiani, G. De Pietro, A. Dipandà, Multiple Structured Light-Based Depth Sensors for Human Motion Analysis: A Review, in: *Lect. Notes Comput. Sci., Springer Berlin Heidelberg,* 2012. doi:https://doi.org/10.1007/978-3-642-35395-6_33.
- [118] A. Elhayek, E. De Aguiar, A. Jain, J. Tompson, L. Pishchulin, M. Andriluka, C. Bregler, B. Schiele, C. Theobalt, Efficient ConvNet-based marker-less motion capture in general scenes with a low number of cameras, *Proc. IEEE Comput. Soc. Conf. Comput. Vis. Pattern Recognit.* 07-12-June (2015) 3810–3818. doi:10.1109/CVPR.2015.7299005.
- [119] C.C. Lim, M. Affandi, S.N. Basah, M.Y. Din, Evaluating Lower Limb Joint Flexion by Computerized Visual Tracking System and Compared with Electrogoniometer and Universal Goniometer, 10 (n.d.) 2289–8131.
- [120] S. Majumder, T. Mondal, M.J. Deen, Wearable sensors for remote health monitoring, *Sensors (Switzerland).* 17 (2017).

doi:10.3390/s17010130.

- [121] M.P. Støve, T.S. Palsson, R.P. Hirata, Smartphone-based accelerometry is a valid tool for measuring dynamic changes in knee extension range of motion, *Knee*. 25 (2018) 66–72. doi:10.1016/j.knee.2017.11.001.
- [122] J. Connolly, J. Condell, B. O’Flynn, J.T. Sanchez, P. Gardiner, IMU Sensor-based Electronic Goniometric Glove (iSEG-Glove) for clinical finger movement analysis, *IEEE Sens. J.* 18 (2017) 1273–1281. doi:10.1109/JSEN.2017.2776262.
- [123] B. Siciliano, O. Khatib, Springer Handbook of Robotics, Springer Berlin Heidelberg, Berlin, Heidelberg, 2008. doi:10.1007/978-3-540-30301-5.
- [124] W.H. Corwin, D.L. Sandry-garza, M.H. Biferno, G.P. Boucek, Assessment of Crew Workload Measurement Methods, Techniques and procedures, 1989.
- [125] S. Akhter, P. Rabiul Islam, L.A. Bhuiyan, M. Hasan, A.F.M.S. Saif, An Analysis on Position Estimation, Drifting and Accumulated Error Accuracy during 3D Tracking in Electronic Handheld Devices, *J. Comput. Commun.* 06 (2018) 65–75. doi:10.4236/jcc.2018.64006.
- [126] Bosch Sensortec, BNO055 Intelligent 9-axis absolute orientation sensor, 2014.
- [127] K. Townsend, Adafruit BNO055 absolute orientation sensor, Adafruit Learn. Syst. (2019) 1–39.
- [128] J. Diebel, Representing attitude: Euler angles, unit quaternions, and rotation vectors, *Matrix*. 58 (2006) 1–35. doi:10.1093/jxb/erm298.
- [129] U.Y. Usta, Comparison of quaternion and euler angle methods for joint angle animation of human figure models, Naval Postgraduate School, 1999.
- [130] E. Salamin, Application of quaternions to computation with rotations, (1995) 1–10.
- [131] E. Cynthia C. Norkin PT, D.S. D. Joyce White PT, Measurement of Joint Motion A Guide to Goniometry, 4th ed., 2009. doi:10.2310/6640.2004.00031.

- [132] CyberGloveSystems, CyberGlove Systems, Data Sheet. (2015) 1–2.
- [133] The University of Michigan Center for Ergonomics, 3D Static Strength Prediction Program, *J. Occup. Environ. Med.* 38 (1996) 101. doi:10.1097/00043764-199601000-00028.
- [134] RepRap, RepRap GCode Cheat Sheet., 2007.
- [135] H.H. Hamzah, S.A. Shafiee, A. Abdalla, B.A. Patel, 3D printable conductive materials for the fabrication of electrochemical sensors: A mini review, *Electrochem. Commun.* 96 (2018) 27–31. doi:10.1016/j.elecom.2018.09.006.
- [136] K.G.J. Christiyana, U. Chandrasekhar, K. Venkateswarlu, A study on the influence of process parameters on the Mechanical Properties of 3D printed ABS composite, *IOP Conf. Ser. Mater. Sci. Eng.* 114 (2016). doi:10.1088/1757-899X/114/1/012109.
- [137] M.A. Cruz, S. Ye, M.J. Kim, C. Reyes, F. Yang, P.F. Flowers, B.J. Wiley, Multigram Synthesis of Cu-Ag Core–Shell Nanowires Enables the Production of a Highly Conductive Polymer Filament for 3D Printing Electronics, *Part. Part. Syst. Charact.* 35 (2018). doi:10.1002/ppsc.201700385.
- [138] M. Asadi-Eydivand, M. Solati-Hashjin, A. Farzad, N.A. Abu Osman, Effect of technical parameters on porous structure and strength of 3D printed calcium sulfate prototypes, *Robot. Comput. Integr. Manuf.* 37 (2016) 57–67. doi:10.1016/j.rcim.2015.06.005.
- [139] M. Korger, J. Bergschneider, M. Lutz, B. Mahltig, K. Finsterbusch, M. Rabe, Possible applications of 3D printing technology on textile substrates, *IOP Conf. Ser. Mater. Sci. Eng.* 141 (2016). doi:10.1088/1757-899X/141/1/012011.
- [140] N. Grimmelsmann, M. Kreuziger, M. Korger, H. Meissner, A. Ehrmann, Adhesion of 3D printed material on textile substrates, *Rapid Prototyp. J.* 24 (2018) 166–170. doi:10.1108/RPJ-05-2016-0086.
- [141] Y. Martens, A. Ehrmann, Composites of 3D-Printed Polymers and Textile Fabrics*, *IOP Conf. Ser. Mater. Sci. Eng.* 225 (2017). doi:10.1088/1757-899X/225/1/012292.

-
- [142] T. Spahiu, M. Al-Arabiyyat, Y. Martens, A. Ehrmann, E. Piperi, E. Shehi, Adhesion of 3D printing polymers on textile fabrics for garment production, *IOP Conf. Ser. Mater. Sci. Eng.* 459 (2018). doi:10.1088/1757-899X/459/1/012065.
- [143] E.P. T. Spahiu, N. Grimmelsmann, A. Ehrmann, E. Shehi, Effect of 3D printing on textile fabric, *Eng. Entrep.* (2017).
- [144] A.E. Christopher Dopke, Nils Grimmelsmann, 3D printing on knitted fabrics, *Int. Melliand.* (2017) 97–98.
- [145] J. Oyón-Calvo, A. Cazón-Martín, M.I. Rodríguez-Ferradas, L. Francés-Morcillo, L. Matey-Muñoz, P. Morer-Camo, Additive manufacturing on textiles with low-cost extrusion devices: Adhesion and deformation properties, *Dyna.* 94 (2019) 221–225. doi:10.6036/8893.

